AD-A099 591 BOHAN (WALTER A) CO PARK RIDGE IL F/G 4/2
NAVY TACTICAL APPLICATIONS GUIDE. VOLUME 3. NORTH ATLANTIC AND --ETC(U)
MAR 81 R W FETT, W A BOHAN N00228-79-C-3202

UNCLASSIFIED NEPRF-TR-80-07-VOL-3 NL

1 of 2

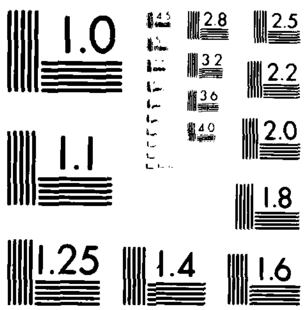

MICROCOPY RESOLUTION TEST CHART
NATIONAL BUREAU OF STANDARDS 1963-A

LEVEL II

UNCLASSIFIED

SECURITY CLASSIFICATION OF THIS PAGE (When Data Entered)

REPORT DOCUMENTATION PAGE		READ INSTRUCTIONS BEFORE COMPLETING FORM
1. REPORT NUMBER NAVENVPREDRSCHFAC Technical Report 80-07	2. GOVT ACCESSION NO. AD-A099591	3. RECIPIENT'S CATALOG NUMBER
4. TITLE (and Subtitle) Navy Tactical Applications Guide. Volume 3 North Atlantic and Mediterranean Weather Analysis and Forecast Applications		5. TYPE OF REPORT & PERIOD COVERED 6. PERFORMING ORG. REPORT NUMBER
7. AUTHOR(s) Robert W. Fett and Walter A. Bohan		8. CONTRACT OR GRANT NUMBER(s) The Walter A Bohan Company N00228-79-C-3202
9. PERFORMING ORGANIZATION NAME AND ADDRESS The Walter A. Bohan Company 2026 Oakton Street Park Ridge, Illinois 60068		10. PROGRAM ELEMENT, PROJECT, TASK AREA & WORK UNIT NUMBERS 62759N. WF 59-553. NEPRF WU: 6.2-9
11. CONTROLLING OFFICE NAME AND ADDRESS Naval Air Systems Command Department of the Navy Washington, D.C. 20361		12. REPORT DATE March 1981 13. NUMBER OF PAGES 125
14. MONITORING AGENCY NAME & ADDRESS(if different from Controlling Office) Naval Environmental Prediction Research Facility Monterey, California 93940		15. SECURITY CLASS. (of this report) Unclassified 15a. DECLASSIFICATION/DOWNGRADING SCHEDULE

16. DISTRIBUTION STATEMENT (of this Report)

Approved for Public Release
Distribution Unlimited

17. DISTRIBUTION STATEMENT (of the abstract entered in Block 20, if different from Report)

18. SUPPLEMENTARY NOTES

Original manuscript for case studies was submitted during calender year 1979.

19. KEY WORDS (Continue on reverse side if necessary and identify by block number)

Meteorological Satellite Systems
Analysis and Forecast Applications
North Atlantic and Mediterranean
Blocking
Cyclogenesis
Coastal Zone Phenomena
Ocean-Atmosphere Interaction

20. ABSTRACT (Continue on reverse side if necessary and identify by block number)

Case studies describing regional environmental analysis and forecast applications based on satellite data and conventional meteorological observations for the North Atlantic and Mediterranean areas are presented. Topics include blocking, cyclogenesis, coastal zone phenomena, and ocean-atmosphere interaction. The studies provide insights into identifiable patterns of weather development that occur frequently, so that once the basic pattern is recognized at an early stage this information can be used for improved weather analysis and forecasting.

DD FORM 1473, 1 JAN 73 EDITION OF 1 NOV 65 IS OBSOLETE
S/N 0102-014-6601

UNCLASSIFIED

SECURITY CLASSIFICATION OF THIS PAGE (When Data Entered)

81 6 01 173

20. Abstract (continued)

The volume also contains a user oriented section on current operational meteorological satellite systems that describes imagery acquisition and distribution, sensor systems, and spectral characteristics. In addition, sample imagery is included for each of the meteorological satellite systems.

NAVY TACTICAL APPLICATIONS GUIDE

VOLUME 3

NORTH ATLANTIC AND MEDITERRANEAN

WEATHER ANALYSIS AND FORECAST APPLICATIONS

METEOROLOGICAL SATELLITE SYSTEMS

Prepared under the direction of
Robert W. Fett
Tactical Applications Department
Naval Environmental Prediction Research Facility

Scientific Coordinator
Walter A. Bohan
The Walter A. Bohan Company

1981

THE WALTER A. BOHAN COMPANY

2026 OAKTON STREET, PARK RIDGE, ILLINOIS 60068
APPLIED RESEARCH IN SATELLITE METEOROLOGY AND OCEANOGRAPHY

Contributors to Volume 3

LCDR Geoffrey A. Stevenson, Royal Navy
Exchange Officer to Naval Environmental Prediction Research Facility
Monterey, California

LCDR Ronald J. Englebretson, U.S. Navy
Naval Environmental Prediction Research Facility
Monterey, California

Jay Rosenthal, Head, Geophysics Division
Pacific Missile Test Center
Point Mugu, California

John J. Bates, Meteorologist
The Walter A. Bohan Company
Park Ridge, Illinois

Foreword

The Navy Tactical Applications Guide, Volume 1, focused on the description of the unique characteristics of DMSP (Defense Meteorological Satellite Program) imagery and basic DMSP image analysis techniques. Volume 2 shifted the emphasis to the identification of environmental (meteorological and oceanographic) phenomena and effects in DMSP imagery and the interpretation of the imagery in operationally oriented terms.

In this volume we will examine satellite imagery from another perspective—how satellite imagery can be used, in conjunction with other environmental data, to forecast future environmental conditions. Because this publication is intended primarily for the U.S. Navy, the case studies we have chosen are for the oceanic, coastal, and nearcoastal regions. Also, since analyses and forecasts for Naval operations are prepared on a regional basis, the volumes are regionally oriented. In this volume the forecast application cases are limited to the North Atlantic and Mediterranean. Volumes 4 and 5 will continue this arrangement and will include case studies for the North Pacific and Indian Ocean, respectively.

This volume also broadens our use of satellite imagery beyond DMSP. We have included in the first section, a discussion of operational satellite systems, including U.S. and foreign satellites. This section will be particularly useful to the environmental forecaster on overseas assignment.

To expedite the receipt of the information in this volume by the operational user, the initial distribution contains only case studies in the important area of cyclogenesis. Other sections are under development and will be distributed separately for inclusion in this volume.

It is anticipated that this volume will assist Navy environmental forecasters to use satellite imagery more effectively in the preparation of better and more accurate forecasts in support of Naval operations.

W. G. SCHRAMM
Captain, U.S. Navy
Commanding Officer, NEPRF

Acknowledgements

The assistance of AG1 Rudy Schaar, AG2 Michael Dodge, AG2 Darryl Wagoner, AG3 Robert Bonaly, AG3 John Benvick, and AG3 Brian Kenthack in developing the documentation for many of the case studies in this volume is gratefully acknowledged. PH1 Albert Matthews processed many of the original photographs used in this publication. The correlative meteorological and oceanographic data used in the case studies were provided by the Fleet Numerical Oceanography Center, Monterey, CA, and the U.S. Naval Oceanographic Command Detachment, Ashville, NC. Appreciation is also extended to the personnel of the DMSP sites at Rota, Spain and San Diego, CA; and aboard the aircraft carriers USS *Constellation*, USS *Kitty Hawk*, USS *John F. Kennedy*, USS *Independence*, and USS *Midway*.

Additional satellite imagery was supplied by the National Earth Satellite Service (NESS) and the Environmental Data and Information Service (EDIS) of the National Oceanic and Atmospheric Administration (NOAA), the European Space Agency (ESA), and the Japan Weather Association (JWA).

The assistance of the staff of The Walter A. Bohan Company is acknowledged; in particular, Lido A. Andreoni for design of the format of the publication and layouts of the case studies. Gregory E. Terhune for his assistance in the preparation of case study graphics and participation in the editing and formatting of the text. The high quality of the reproduction of the satellite imagery used in the case studies and the excellent printing of the publication are due to the combined efforts of Peter M. Samorez and Michael E. Brock.

Contents

Introduction

This volume of the Navy Tactical Applications Guide is the first in a series of regionally oriented volumes devoted to the use of satellite imagery for short and medium range forecasting. For example, given a satellite depiction of today's weather systems over Europe, how can these data be most effectively included in the decision-making process of forecasting tomorrow's weather? The accomplishment of this task is not simple: it involves utilizing the full range of skills of the operational meteorologist, who has been trained in the analysis and interpretation of satellite imagery.

Satellite data must be properly gridded for location and comparison of imagery elements with related synoptic chart weather features. Inorder to highlight synoptic features it may be necessary to enhance the satellite data. Visible and the corresponding infrared imagery should also be compared to obtain information on the vertical extent of cloud formations and on the thermal structure of the underlying terrain and of the sea. The meteorological implications of these data can then be integrated with conventional analyses and prognoses, taking into consideration the multi-leveled structure of the atmosphere and inter-relationships between levels in terms of vertical motions and resulting dynamical changes.

Finally, the forecasts must be developed within a regional context, considering the particular topography and climatology of the area involved. This also includes a knowledge of the regional oceanography, so that important air-sea interaction effects are not neglected as input to the forecast.

Because of operational forecasters' detailed knowledge of the influences of local environmental conditions on weather pattern evolution, it is recognized that they have developed, and will continue to develop, many local forecasting techniques. As the following case studies will demonstrate, it is important that new forecasting techniques include satellite data. Therefore, suggestions for supplemental case studies to this, and to future guides in this series, should include pertinent satellite depictions. Address comments and suggestions to the Tactical Applications Department, Naval Environmental Prediction Research Facility.

Section 1

Operational Environmental Satellites

1A Polar-orbiting Satellites

1B Geostationary Satellites

1A Polar-orbiting Satellites

Sun-synchronous Polar-orbiting Satellites

Both the TIROS-N/NOAA and DMSP satellites are launched with an inclination such that the orbit is sun-synchronous. This means that the orbital plane of the satellite precesses 360° in 365 days. Precession of the orbital plane at this rate keeps it always in the same orientation with respect to the sun, day to day and revolution to revolution. Thus, an individual satellite may be termed to be in a morning, noon, or afternoon orbit (pass) depending on this orientation.

The combination of precession of the orbital plane and the rotation of the Earth produces an apparent westward motion of the satellite subtracks on the Earth (Fig. 1A-1a). At a near-circular orbital altitude of 835 km, these satellites have an orbital period of 101.4 minutes. Subtracting the orbital precession, the longitude of the ascending node increases about 25° per revolution. Since the orbital period is 101.4 minutes, there are 14 revolutions in less than 24 hours. This means that the first revolution occurs about five degrees further east each day.

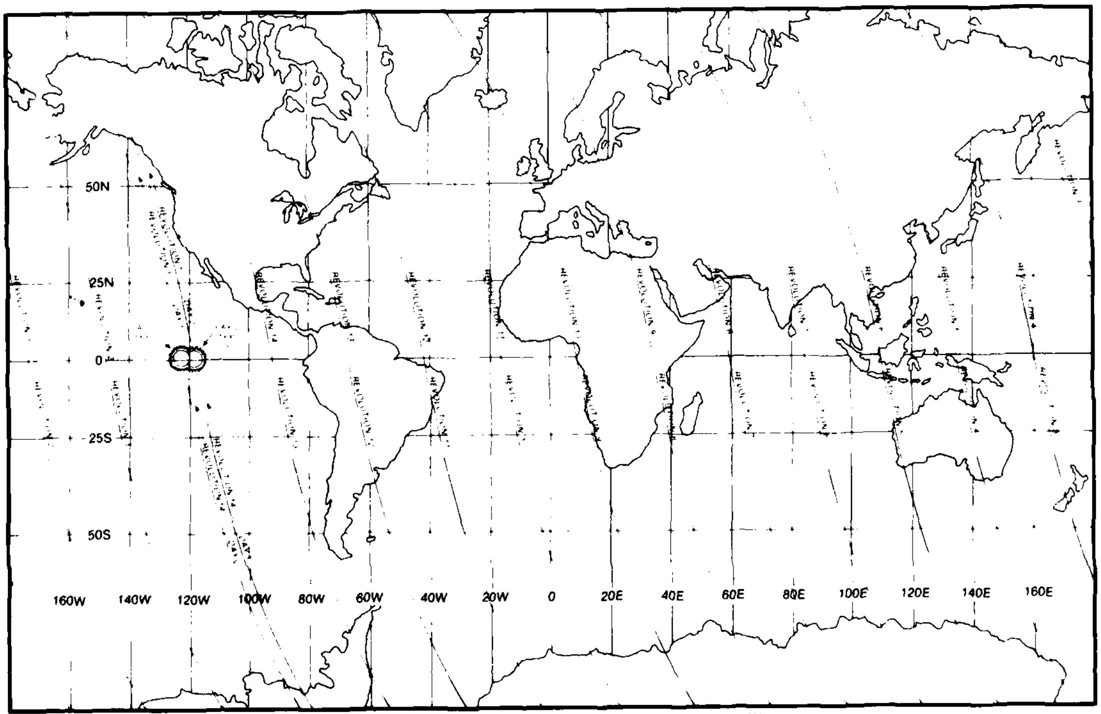

1A-1a. Ascending orbit satellite subtracks for a noon sun-synchronous polar-orbiting satellite.

National Oceanic and Atmospheric Administration
Polar-orbiting Satellite Program

(TIROS-N/NOAA)

The NOAA polar-orbiting satellite program, TIROS-N/NOAA[1], provides (1) high resolution, day and night multispectral imagery of the Earth, its atmosphere, and clouds, (2) improved observations of vertical temperature and moisture profiles, and (3) a high capacity data collection and platform location system. Only the image products obtained from the satellite are described in this section.

The operational system includes two satellites; NOAA-6 in a morning pass (0730 LST descending node) and TIROS-N in an afternoon pass (1500 LST ascending node). Both spacecraft are in near-polar, sun-synchronous orbits. TIROS-N orbits at an average altitude of 854 km, while NOAA-6 and all future spacecraft in the series will orbit at an average altitude of 833 km. The orbital period is approximately 102 minutes which produces 14.2 revolutions per day.

1. TIROS-N is the name of the first spacecraft in this program. Subsequent spacecraft will be named NOAA-6 through NOAA-12.

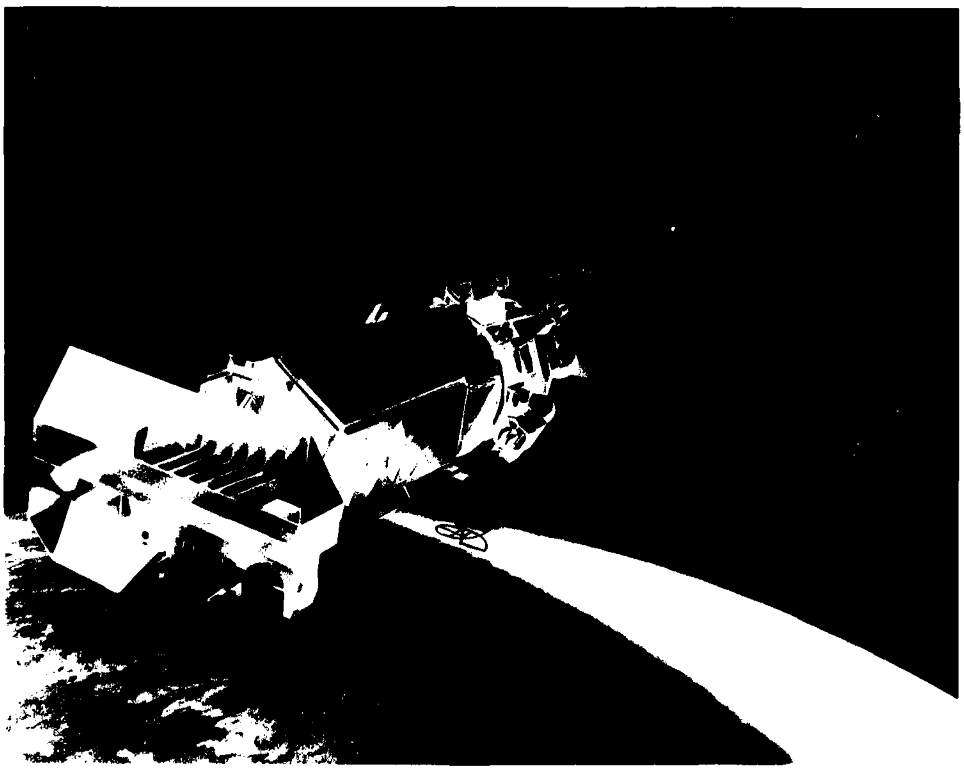

1A-3a. The TIROS-N/NOAA satellite is a five-sided box-like structure which is approximately 12 ft long and 6 ft wide. Four of the five sides are equal in size and contain a total of twelve thermal cooling panels. The fifth side is wider than the other four and contains the communication antenna and the Earth-viewing sensors. At one end of the spacecraft is a large panel containing arrays of solar power cells. This panel is motor-driven to rotate once per orbit so that it continuously faces the sun during the daylight portions of the orbit.

Image Acquisition

Imagery from the Advanced Very High Resolution Radiometer (AVHRR) is available from each spacecraft in two operational modes to direct readout users. The first is direct readout of any two spectral channels to ground receiving stations of the Automatic Picture Transmission (APT) class at 2 n mi resolution. The second mode is direct readout of all four spectral channels to ground receiving stations of the High Resolution Picture Transmission (HRPT) class at 0.5 n mi resolution. The swath width of the AVHRR is approximately 1700 n mi.

The APT systems receive an analog signal from the spacecraft on the standard APT frequencies. One visible channel (0.55-0.90 μm on TIROS-N and 0.58-0.68 μm on NOAA-6) is used to provide imagery during daytime, and one infrared channel (10.5-11.5 μm) is used to provide imagery day and night.

The APT data are output at a rate of 120 lines per minute and the along scan samples are averaged so that the resolution is nearly constant. This greatly reduces panoramic distortion of the image at the edges. To produce this nearly constant resolution in the along scan direction, each scan line is divided into five zones from the subpoint to the end of the scan line, with each zone using a different averaging algorithm. To obtain the 120 lines per minute rate, only every third line from the 360 lines per minute AVHRR HRPT output is transmitted. This reduces the resolution of the APT imagery to approximately 2 n mi (Fig. 1A-4a). Simulations have shown that this algorithm retains all significant features near the satellite subpoint and near the ends of scan.

The HRPT system transmits all four AVHRR spectral channels at 0.5 n mi resolution. These data do not undergo any preprocessing on-board the spacecraft. Also, HRPT data are transmitted in digital form requiring software at user sites so that the data can be properly formatted for operational display.

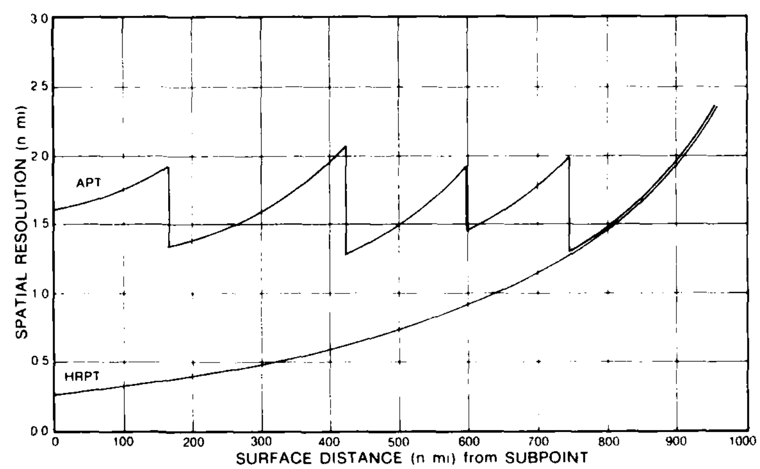

1A-4a. Surface resolution of the TIROS-N NOAA APT and HRPT imagery.

Sensor System Description

The AVHRR sensors are mounted in a sensor package at one end of the spacecraft so that with nominal attitude control the sensors are always oriented toward the Earth. The basic operation of the AVHRR is

similar to its predecessor, the VHRR, which flew on the ITOS/NOAA series satellites. That is, it is a line scan device; global coverage is achieved from continuous horizon-to-horizon crosstrack scanning by a mirror combined with the forward motion of the spacecraft. The scanning mirror rotates at a constant rate of 360 revolutions per minute. Once during each revolution, a synchronization pulse is generated as the mirror reaches a precise pre-Earth position. Upon receipt of the synchronization pulse, a data sampling process begins which takes the appropriate number of samples at specified times during the scan line. The data from the AVHRR is then processed to provide separate outputs for APT and HRPT formats in real-time.

Radiation from the Earth scene is gathered by an optical system which consists of a Cassegrain telescope combined with secondary optics. The secondary optics separates the radiant energy into discrete spectral bands which are focussed onto their respective focal planes. The instantaneous field of view (IFOV) for all channels is specified to be 1.3±0.1 milliradians which gives a spatial resolution of 0.5 n mi at the satellite subpoint. The IFOV was chosen so that the satellite motion along its orbital path would cause successive scan lines to be contiguous at the satellite subpoint. The instrument has been designed so that the IFOV of the four channels can be made coincident within ±0.1 milliradians (±8%).

The visible and near infrared channels of the AVHRR use silicon detectors to measure incident radiation. The infrared channels use metal-segment detectors cooled to 105° K. A bimetal (InSb) has been chosen for the 3.55 3.93 μm channel, while the 10.5-11.5 μm channel uses a trimetal (HgCdTe) detector. In all channels, the zero point for detected energy is restored to a zero level once each scan while viewing space. The output of the radiometer during the remainder of the scan is equal to the difference in detected energy between space and the radiated energy from the detection scene. The system has been designed so that instrument output is linear with input energy.

Variations in the electronic signal used to gather and transmit the infrared data produce random or coherent noise patterns on the signal radiated from the Earth. When the noise patterns are of comparable magnitude to the temperature gradient under scrutiny, it becomes difficult to distinguish one from the other. A measure of the total noise produced by an infrared sensing system is the Net Equivalent Temperature Difference (NETD). The NETD of the TIROS-N/NOAA infrared channels is better than 0.12° K (for a 300° K scene). The temperature sensitivity of these channels is approximately 0.5° K at the same temperature. Since the NETD is less than the temperature sensitivity, accurate identification of thermal gradients is made feasible.

During every scan line, the AVHRR views cold space (zero radiance) and its housing (approximately 290° K). The housing portion of the instrument has been designed to be a blackbody target to be used in orbit for instrument calibration. Four thermometers whose output values are included in the data stream are embedded in the housing and monitor the temperature of the target. By determining the instrument output while viewing cold space and the known warm target, it is possible to ascertain the instrument response curve. This permits on board calibration of the infrared channels.

Channel Characteristics

The AVHRR channel characteristics are summarized in Table 1A. After the fourth spacecraft in the series, the AVHRR will be expanded to include a fifth channel (11.5-12.5 μm), and the system will be renamed AVHRR/2.

TABLE 1A
TIROS-N/NOAA
AVHRR Spectral Channel Characteristics

Channel 1 wavelength will be 0.58-0.68 μm for all instruments after the TIROS-N flight model. Channel 4 wavelength will be 10.3-11.3 μm for all AVHRR/2 instruments. Channel 5 has been added to the A RR/2 instrument to further enhance sea surface temperature measurements in the tropics.

Channel	Resolution at Subpoint	Wavelength (μm)
1	0.5 n mi	0.55-0.90
2	0.5 n mi	0.725-1.10
3	0.5 n mi	3.55-3.93
4	0.5 n mi	10.5-11.5
5	0.5 n mi	11.5-12.5

The normalized sensor response curve of TIROS-N channel 1 (0.55-0.90 μm) is shown in Fig. 1A-6a. As can be seen, this channel has a broad peak response in the interval from 0.7–0.9 μm, in the near infrared, and there is little or no response in the blue portion of the visible spectrum (<0.5 μm). This channel is used for daytime mapping of clouds and Earth surface features. On NOAA-6 and all future spacecraft in the series, the response of this channel will be narrowed to 0.58-0.68 μm so that the sensor responds only in the visible light portion of the spectrum and does not overlap with the response of channel 2.

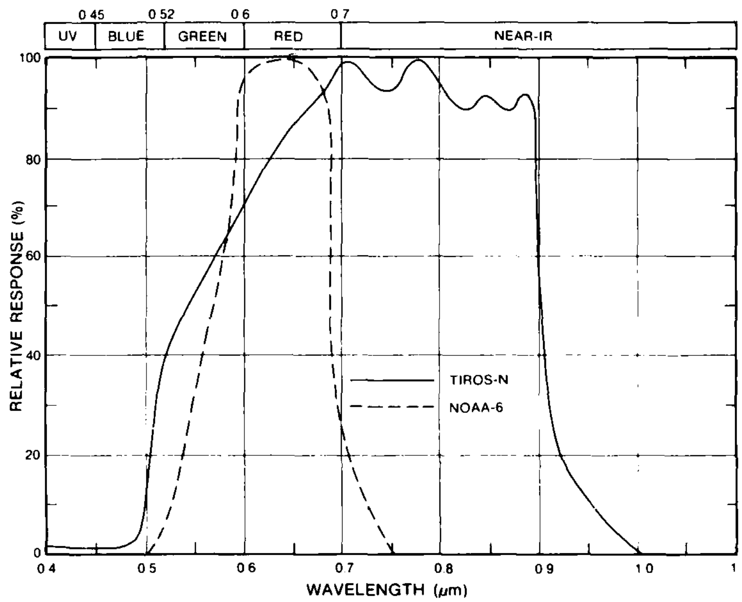

1A-6a. TIROS-N NOAA channel 1 normalized sensor response curves.

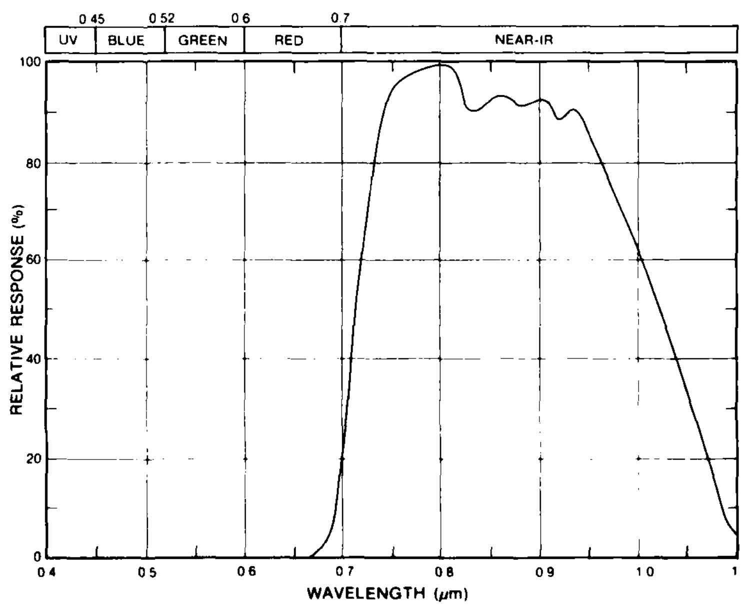

1A-6b. TIROS-N NOAA channel 2 normalized sensor response curve.

The normalized response curve of channel 2 (Fig. 1A-6b) is limited to the near infrared with a peak response near 0.8 μm. Since liquid water absorbs near infrared radiation more strongly than visible radiation, this channel is used prima-ily for daytime delineation of surface water and land/water boundaries. In addition, by comparing data from channels 1 and 2 it is possible to locate areas of ice-snow melt.

The normalized sensor response curves of the two infrared channels are shown in Figs. 1A-7a and 1A-7b. These channels are used for determining the temperature of the radiating surface (land, sea, or atmosphere). Channel 3 (3.55–3.93 μm) is normally used at night, since the response of this channel is contaminated by reflected solar radiation

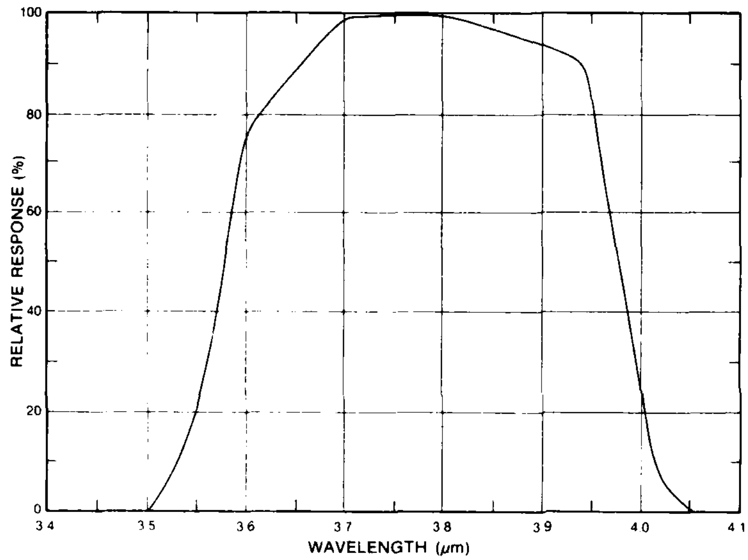

1A-7a. TIROS-N NOAA channel 3 normalized sensor response curve.

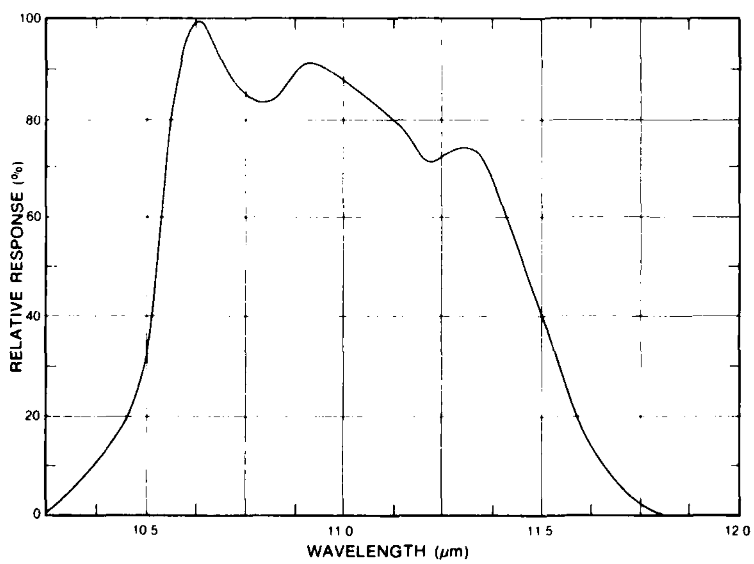

1A-7b. TIROS-N NOAA channel 4 normalized sensor response curve.

during the day. In this spectral range, there is almost no absorption by water vapor. As a result, surface radiation can penetrate heavy water vapor concentrations and some thin clouds with little loss of energy. This channel is especially useful in the tropics for delineating sea surface temperatures because of these characteristics.

Channel 4 (10.5-11.5 μm) is used continuously day and night since it responds to the peak radiations emitted by the Earth and its atmosphere and is not affected by reflected solar radiation. Although attenuation by water vapor is minimized in this region, variations in water vapor concentrations, both horizontally and vertically, still cause significant attenuation when viewing Earth surface temperatures. A fifth channel, sensitive in the 11.5-12.5 μm region, will be added later to the AVHRR making it possible to account for some effects of water vapor attenuation in the determination of surface temperatures.

References

Hussey, W.J., 1979: The TIROS-N NOAA Operational Satellite System. National Environmental Satellite Service, NOAA, Washington, D.C., 35 pp.

Kidwell, K.B., 1979: NOAA Polar Orbiter Data (TIROS-N) Users Guide Preliminary Version. National Climatic Center, Satellite Data Services Division, Washington, D.C., 172 pp.

Schwalb, A., 1978: The TIROS-N NOAA A-G Satellite Series. NOAA Tech. Memo. NESS 95, National Environmental Satellite Service, NOAA, Washington, D.C., 75 pp.

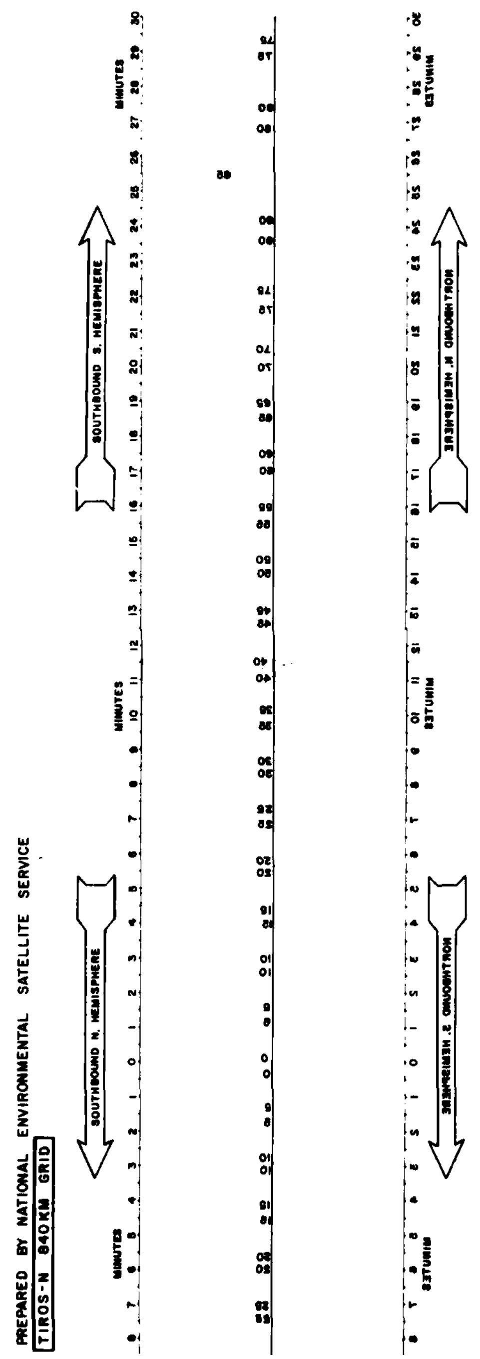

Operational User Aid

This TIROS-N APT grid shows the orbital subtrack and areal coverage for any satellite pass. To use the grid:

1. Make an acetate copy of the grid to the same scale as the satellite image so that the border of the image and grid coincide.

2. Determine whether the satellite pass is northbound (ascending) or southbound (descending) and rotate or flip the grid appropriately.

3. Use standard APT techniques for grid registration to the picture.

Due to recorder characteristics, this grid may not fit your display device. Individual sites should check the accuracy of this grid and, if necessary, hand-construct a grid that fits your display. For additional information on gridding, individual sites may contact NEPRF.

These images (Figs. 1A-10a and 1A-11a) were acquired operationally on-board R/V Knorr on a research cruise out of Woods Hole, Mass., to the Grand Banks area of Newfoundland.

In the visible picture, sunglint is apparent along the right edge of the image, while a large area of cellular cloudiness occurs to the northwest behind a frontal cloud band. The infrared picture shows a Gulf Stream meander south of Nova Scotia.

1A-10a. NOAA-6 APT. Visible Picture (Channel 1), 2 n mi Resolution. 1137 GMT 15 October 1979.

1A-11a NOAA-6 APT Enhanced Infrared Picture (Channel 4), 2 n mi Resolution, 1152 GMT 19 October 1979.

In Fig. 1A-12a sunglint appears along the western portion of the image in this afternoon, descending pass. The long, narrow, north-south oriented line east of the sunglint may be related to a surface slick formation. Such slicks have been frequently noted in association with seaweed and organic material which stretches for great distances over the Sargasso Sea and Gulf Stream region. In the corresponding infrared picture (Fig. 1A-13a) note that some apparent sea surface temperature features are actually clouds in the visible picture, while the sunglint apparent in the visible picture is not detected by the infrared channel. These pictures reveal the importance of having both visible and infrared imagery simultaneously for accurate interpretation of phenomena and effects.

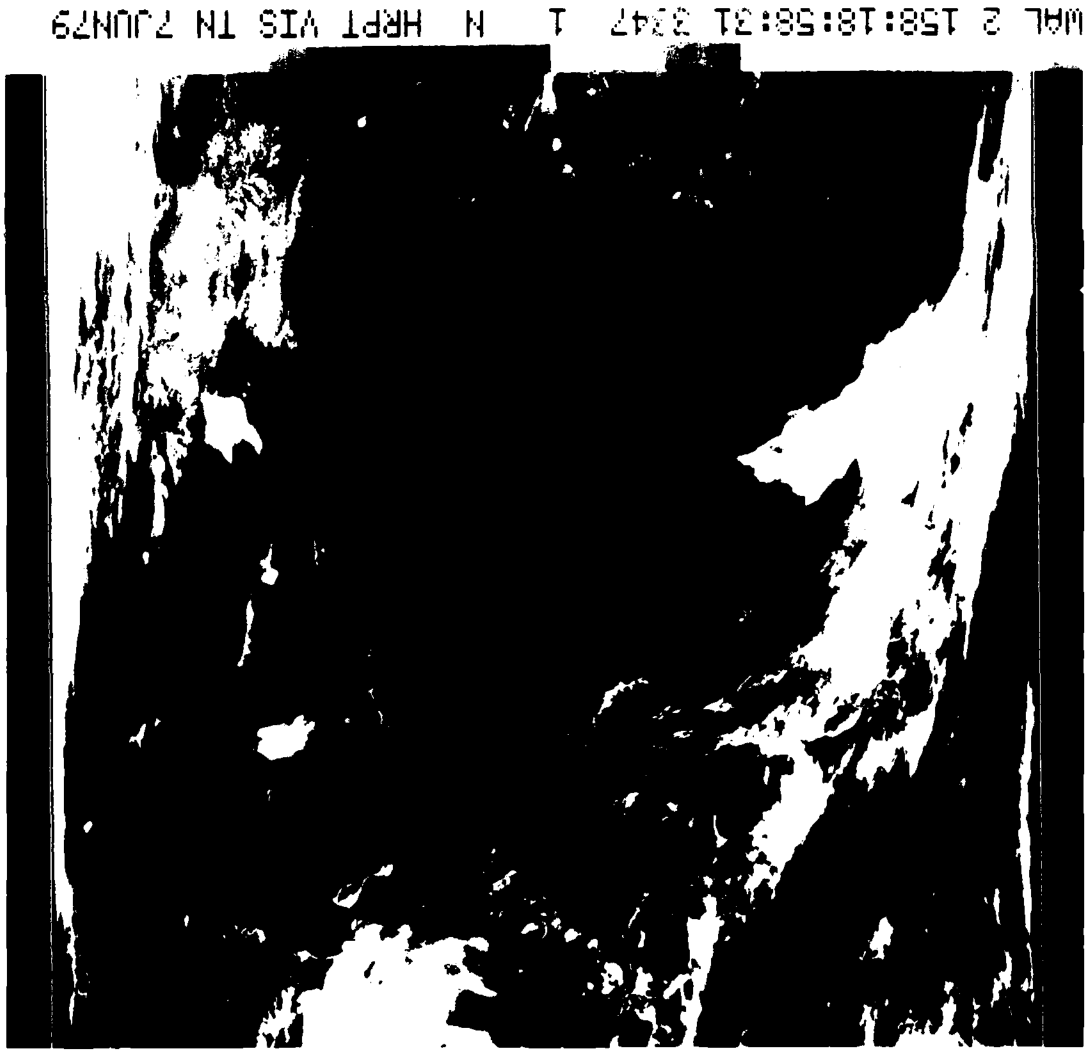

1A-12a. TIROS-N HRPT. Visible Picture (Channel 1), 0.5 n mi Resolution, Descending Node, 1915 GMT 15 June 1979. (Photo Courtesy of NOAA EDIS.)

1A-13a. TIROS-N HRPT. Infrared Picture (Channel 4), 0.5 n mi Resolution, Descending Node, 1915 GMT 15 June 1979. (Photo Courtesy of NOAA EDIS.)

Defense Meteorological Satellite Program
(DMSP)

The Block 5D satellite is the second generation polar-orbiting satellite developed to support operations of the Department of Defense (DOD). The spacecraft is in a near-polar, sun-synchronous orbit at an altitude of approximately 835 km. The orbital period is 101.4 minutes which produces 14.2 orbits per day. The operational system includes at least two satellites; one in a morning orbit (0730 LST descending node), and one in a noon orbit (1200 LST ascending node). This section describes some aspects of the Block 5D spacecraft pertinent to the image data received by direct read-out tactical sites throughout the world.

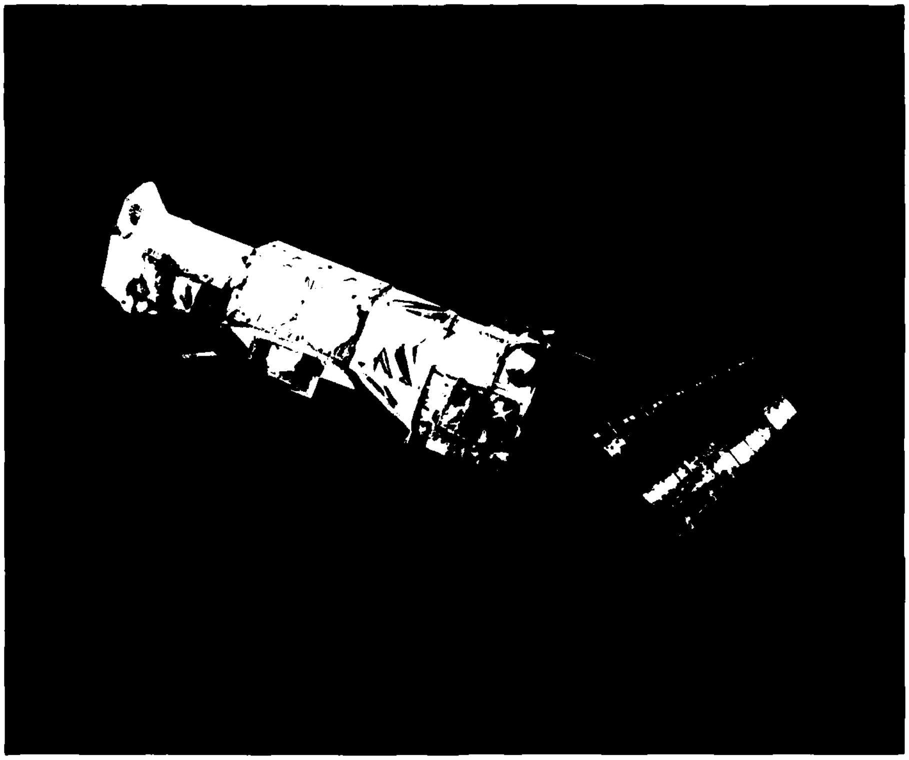

1A-15a. The Block 5D satellite is an integrated spacecraft in that the launch vehicle upper stage remains attached to and provides support for the satellite in orbit. The satellite itself is a five-sided box-like structure (the prototype for TIROS-N) in which four of the five sides are equal in size and contain thermal control louvers, while the fifth side is wider and contains the Earth-viewing sensors. A large solar power panel is attached to one end of the spacecraft; it rotates once each orbit so that it is always oriented toward the sun during the daylight portions of the orbit.

Image Acquisition

The Operational Linescan System (OLS) is the primary image acquisition system on the DMSP Block 5D spacecraft. The system is designed to gather visible and infrared spectrum data from Earth scenes, and to transmit such data in real-time or to store multi-orbit data for later transmission to a central receiving facility. The OLS data processing subsystem performs command, control, data manipulation, storage, and management functions. Commands are received from the ground through the spacecraft communications system, stored, and processed according to time codes. The OLS executes commands, accomplishes smoothing of fine resolution data, derives gain commands from orbital parameters for normalization of visible data and dynamic signal control, and outputs the data to the spacecraft communications system. All data are processed, stored and transmitted in encrypted (direct readout) or clear (stored) digital form.

Three S-band transmitters are provided on the Block 5D spacecraft for data transmission. Two of these may be operated simultaneously for stored data playback. The third is used for real-time data transmission to direct readout tactical sites. A combination of one channel fine (F) resolution data (0.3 n mi resolution) and the complimentary smoothed (S) resolution data (1.5 n mi resolution) are provided in the real-time data transmission mode.

The stored data may consist of either fine resolution or smoothed resolution data. Tape recorder capacity and transmission constraints limit the quantity of fine resolution data which can be stored to a total of 40 minutes per central ground station readout. Data smoothing permits global coverage in both the infrared and visible spectrum to be stored on tape recorders. A total of up to 400 minutes of smoothed resolution data may be transmitted to the central ground station at the Air Force Global Weather Center (AFGWC), Offutt, Nebraska.

Sensor System Description

Two spectral channels are used in the OLS. One channel responds to reflected solar or lunar radiation in the 0.4-1.1 μm range and is termed the visible light or L band. Two different detectors are used for collection of L band data; one is a silicon diode for collection of fine resolution data (LF) during daytime, the other is a photomultiplier tube (PMT) for collection of low resolution data (LS) under quarter moonlight or brighter nighttime conditions. The other channel of the OLS responds to emitted Earth, atmosphere, and cloud radiation in the 8.0-13.0 μm range and is called the thermal infrared or T band.

To achieve global coverage, the DMSP spacecraft has a scanning optical telescope system driven in sinusoidal motion by counter-reacting coiled springs and a pulsed motor. This motion moves the IFOV of the detectors across the satellite subtrack with maximum scanning velocity at nadir. The scanning velocity slows as the telescope reaches the end of scan and reverses during the overscan period. Contiguous along track scanning is accomplished by the motion of the satellite in its orbit. The sinusoidal scan motion causes the surface velocity of the detector IFOV (i.e., the scene temporal resolution) to be nearly constant. Since the geometric resolution of a sensing system is related to the product of the scene spatial resolution and the scene temporal resolution, the sinusoidal motion (along with detector switching, discussed later) permits nearly-constant geometric resolution.

The OLS optical system is divided into two portions, the oscillating telescope assembly and the relay optics. The oscillating telescope

assembly consists of a Cassegrain telescope and three additional mirrors which redirect the incident radiant energy to the relay optics. One of these mirrors also provides image motion compensation. Compensation is required because the telescope reverses scan direction on alternate scans. Fig. 1A-17a shows the path of the IFOV of the telescope on the ground with and without image motion compensation.

The relay optics are the stationary portion of the OLS which deliver focussed Earth scene energy to each of three detectors (silicon diode, PMT, and trimetal). They consist of beam splitters which divide the radiant energy into discrete spectral bands and lenses which focus the energy onto the focal plane of each of the detectors.

At the fine mode visible detector, composed of three silicon diode segments, detector geometry and segment switching compensate for the enlargement and rotation of the IFOV projection on the Earth scene as

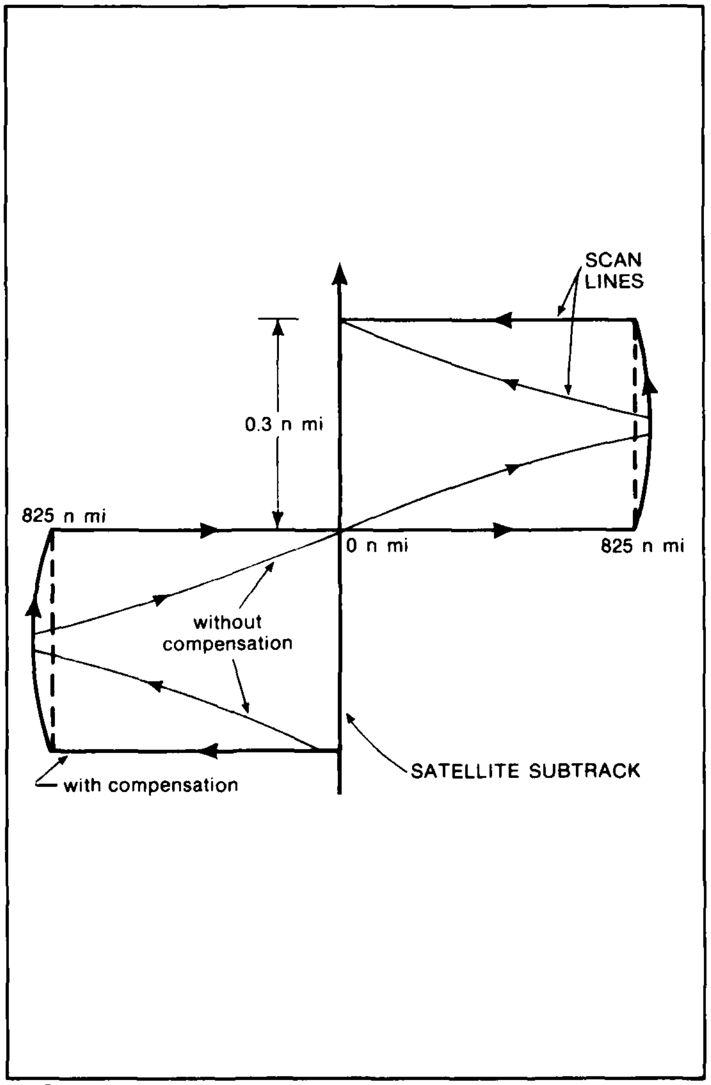

1A-17a. OLS scan line projection on the ground with and without image motion compensation.

scan angle increases. Fig. 1A-18a illustrates the concept of IFOV rotation and switching. Four scan positions are depicted via the projection of the detector IFOV on the ground. The circled dot indicates the centroid of the nadir IFOV in each view and the shaded area indicates the IFOV segment which is on. The dashed lines indicate the two IFOV portions which may be used selectively with increase of scan angle. This selectable portion of the detector is the full IFOV in one direction and one third the full IFOV in the other.

At nadir (0 n mi), the IFOV has the nearly diamond shape of the detector. From nadir to 400 n mi, all three segments of the detector are used. As the surface distance increases from 0 to 400 n mi the IFOV projection on the ground both rotates and enlarges. The diamond-shaped orientation at nadir becomes a more rectangular shape at 400 n mi with the along scan dimension minimized by the rotation. After 400 n mi the IFOV is sw:.:hed to the section at the right side of the nadir IFOV. When scanning the left side of nadir, the IFOV rotation causes the left section to be the proper one to use. At 490 n mi the IFOV projection becomes purely rectangular with the enlargement in the along scan dimension just about compensated for by the reduction due to switching. Near the end of scan (800 n mi), more rotation and significant enlargement of the IFOV have occurred and its projection on the ground becomes nearly square. It can be seen that through the use of rotation

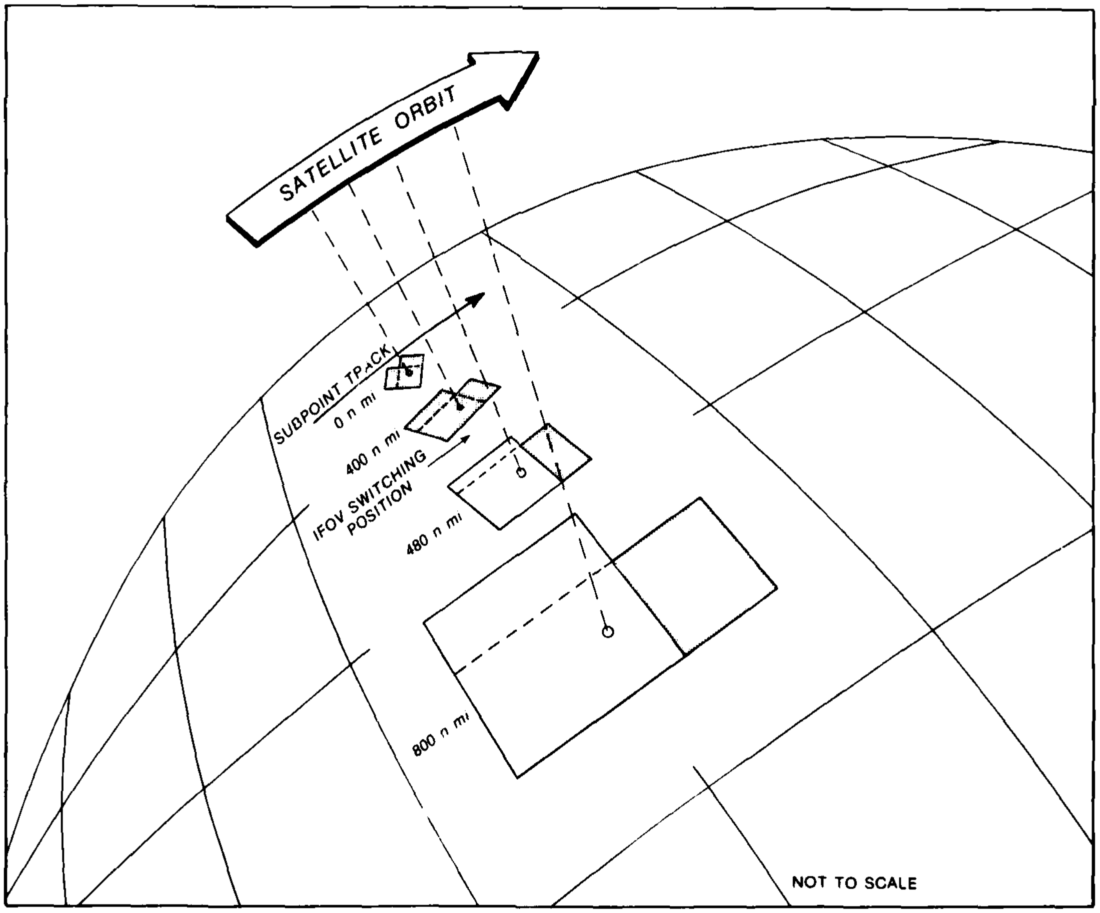

1A-18a. Segmented silicon diode detector field of view projection on the ground.

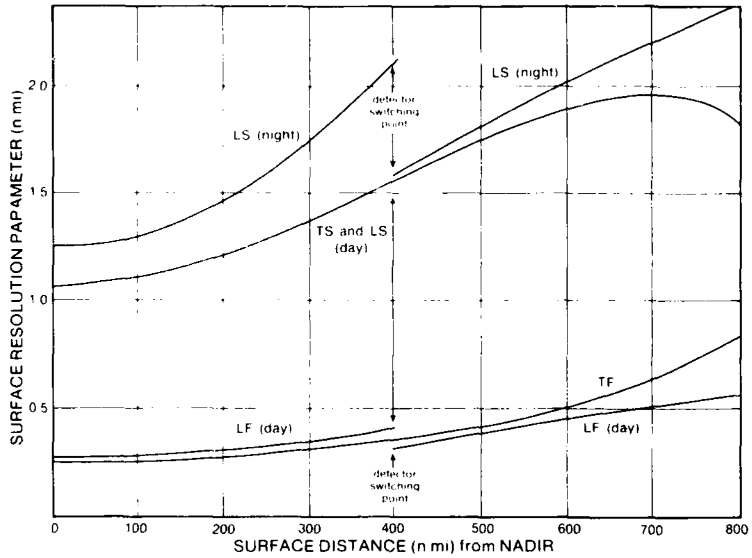

1A-19a. DMSP Block 5D OLS surface resolution.

and switching of the detector IFOV, the scene spatial resolution uniformity along scan has been significantly increased. The ground resolution along scan for all channels of the OLS is summarized in Fig. 1A-19a.

To obtain smooth mode visible data (LS) during daytime, the sensor resolution is reduced to 1.5 n mi by averaging 5 samples at every fifth sample in the along scan direction, then averaging five such 0.3 by 1.5 n mi samples in the along track direction.

A photomultiplier tube (PMT) is used to collect low resolution visible data (1.5 n mi resolution) under quarter moonlight or brighter nighttime conditions. It is important to note that the nighttime Block 5D LS data are not obtained from the segmented silicon detector, but from the PMT which has different spectral characteristics. Nearly constant image resolution in the along scan direction for the PMT is produced electronically. At 420 n mi from the subpoint, the IFOV projection on the ground is reduced and the PMT receives only one third the amount of energy the full IFOV would receive. Because of this, a noticeable degradation of the imagery occurs from 420 n mi to the end of scan in LS nighttime imagery. In addition to nighttime use, there is an option to use the PMT detector in terminator areas where scene illumination is too low for the silicon detector.

The OLS infrared detector is a trimetal (HgCdTe) that is passively cooled to an operating temperature of 105° K. The detector itself consists of two segments which are positioned in the same sense as the two selectable portions of the silicon detector. At nadir, the sampling switches from one segment to the other. This provides approximately constant field of view projection on the ground. Detector switching may sometimes cause a thermal change at nadir in the imagery due to calibration differences between the two detectors. Data smoothing for TS (1.5 n mi resolution) data, is accomplished in the same manner as for daytime LS data.

The infrared sensor output is normalized in terms of the equivalent

blackbody temperature of the radiating object. Output voltage is a linear function of scene temperature. The detector temperature sensitivity is 1.56° K in the temperature range 210–310° K. The NETD of the infrared system is 1° K in this same range.

Channel Characteristics

The normalized sensor response curves of the PMT and silicon diode are shown in Fig. 1A-20a. Two different PMT detector response curves are included. The curves for the F-1, F-2, and F-3 spacecraft have a peak response near 0.6 μm. The response has been modified for the F-4, F-5,

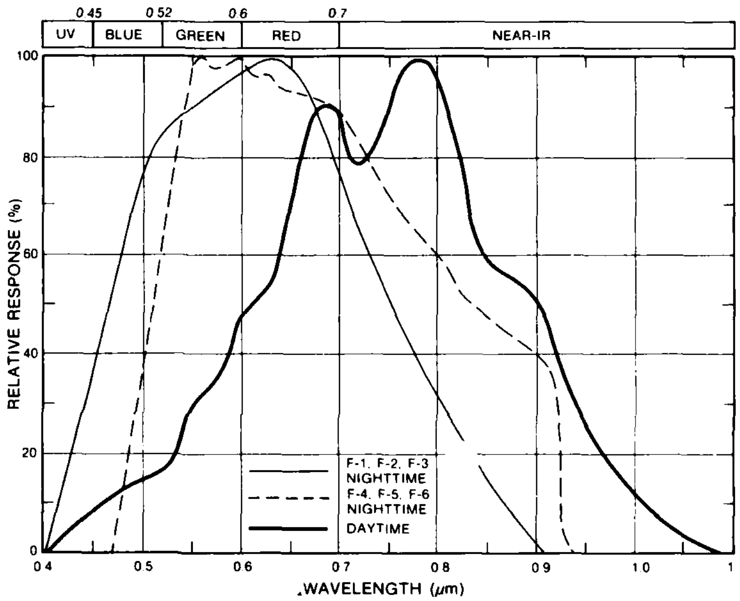

1A-20a. DMSP Block 5D visible channel normalized sensor response curves.

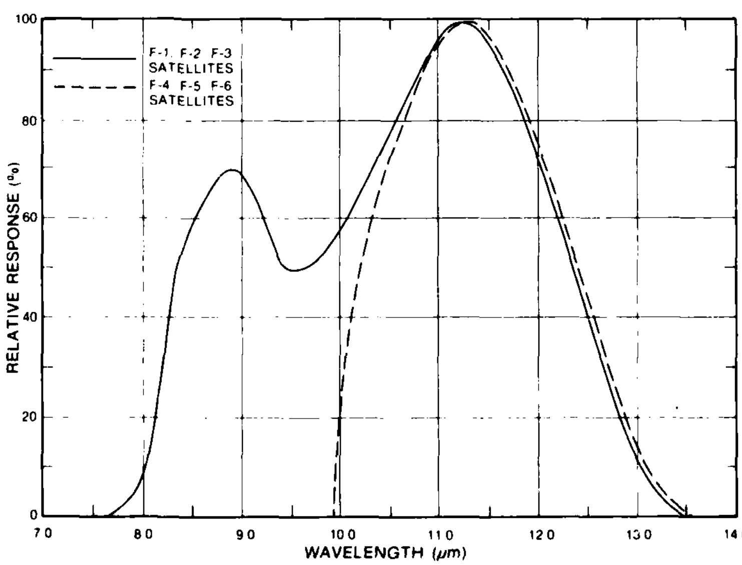

1A-20b. DMSP Block 5D infrared channel normalized sensor response curves.

F-6 and later spacecraft to provide a broader spectral interval extending into the near infrared. The silicon diode detector response extends into and peaks in the near infrared wavelengths. This provides excellent land/water contrast and enhances haze detection capabilities.

The OSL infrared channel (Fig. 1A-20b) senses the 8.0–13.0 μm range. This range contains the peak radiations emitted by the Earth and its atmosphere and is an atmospheric window region largely transparent to outgoing radiation except for appreciable water vapor absorption in moist atmospheres and for an ozone absorption peak at about 0.96 μm (see NTAG, Vol. 2, Sec. 3A, Case 6). This broad spectral range was initially selected to permit fine spatial resolution while still maintaining an acceptable signal-to-noise ratio at the detector.

On the F-4 and subsequent spacecraft, refinements in the infrared detector will permit the spectral range of the sensor to be narrowed to 10.8–12.5 μm while still maintaining an acceptable signal-to-noise ratio. This new, narrower spectral range, unlike the previous range, is not appreciably affected by ozone absorption and is less affected by water vapor absorption. For operations at direct readout sites this means that new correction factors are required to accurately determine surface temperatures and cloud top temperatures and heights. Through experimentation, a combination of surface temperatures and atmospheric sounding profiles was selected from which to derive a base correction for these determinations. These surface temperatures and atmospheric sounding profiles are listed in Table 2A.

TABLE 2A

SURFACE TEMPERATURE (°K)	PROFILE (AFGWC)
310-300	TROPICAL
290-270	U.S. STANDARD
270-250	SUBARCTIC WINTER
250-210	ARCTIC WINTER

The AFGWC has developed several theoretical temperature bias correction curves for the new infrared spectral range. Although these curves were developed for surface temperatures, they can be used to approximate the corrections required for cloud top temperatures by using one of the standard profiles.

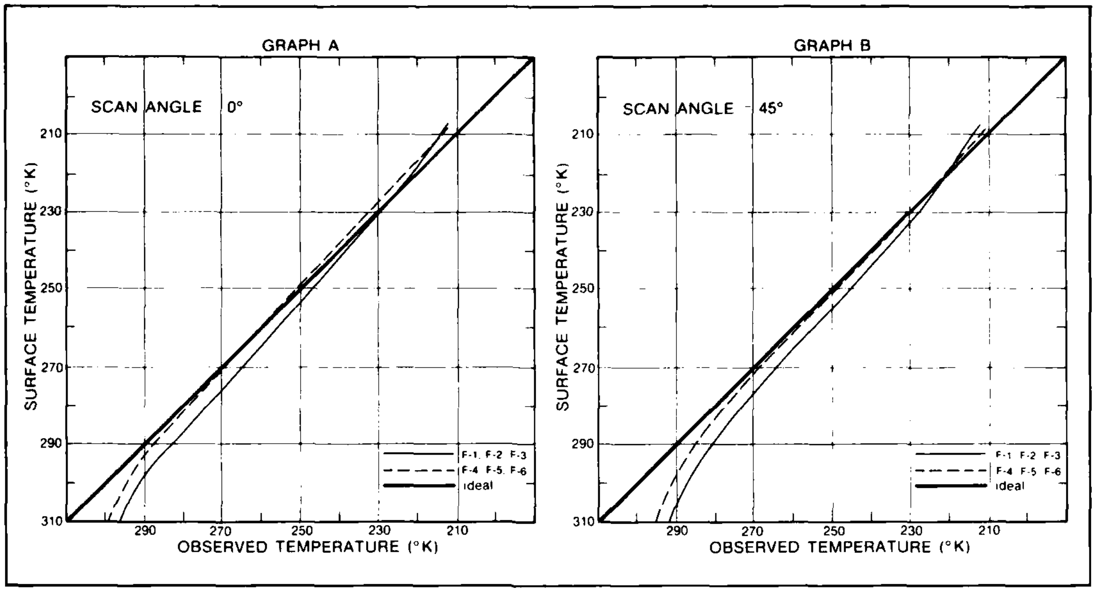

1A-22a. Calculated temperature bias correction curve with surface emissivity equal to 1.0 and scan angles from 0° to 45° (0 to 490 n mi from the satellite subtrack) and scan angle 45° (490 n mi from satellite subtrack) or greater.

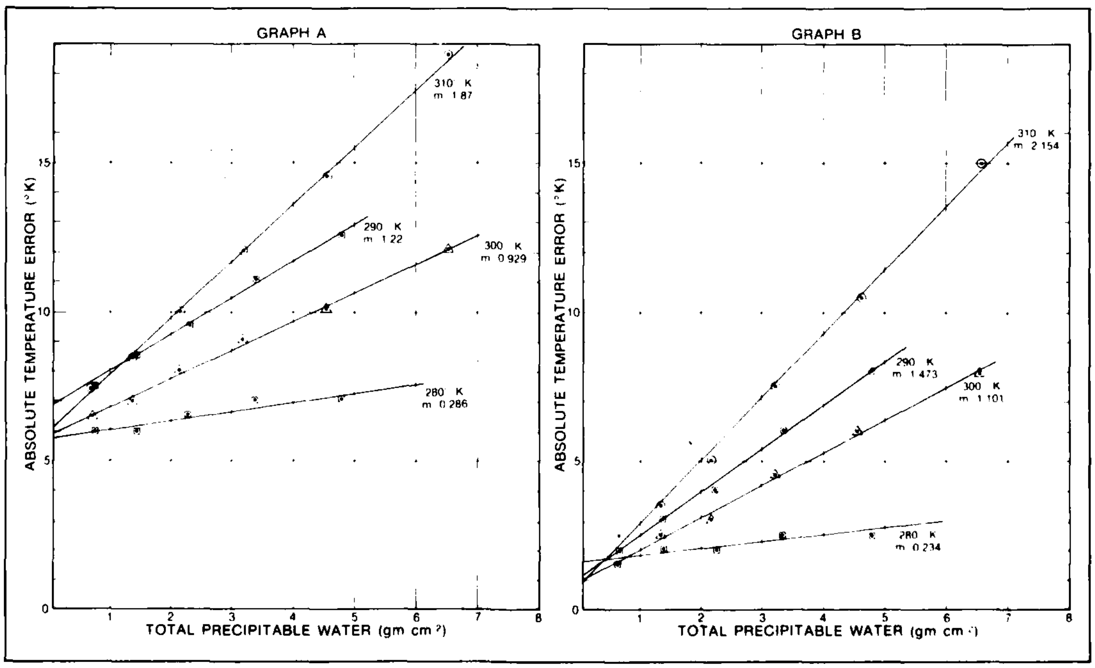

1A-22b. (A) F-1, F-2, and F-3; and (B) F-4, F-5, and F-6 absolute temperature error (ΔT) for the indicated surface temperatures as a function of atmospheric water vapor content.

Temperature bias correction values should be interpolated using Fig. 1A-22a. For scan angles between 0° and 45° (0 to 490 n mi from the satellite subtrack) use Graph A. Use Graph B as an approximation for scan angles greater than 45° (greater than 490 n mi from the satellite subtrack). It can be seen that the absolute temperature error for the F-4, F-5, and F-6 sensor is less than the error for the F-1, F-2, and F-3 sensor.

Corrections for atmospheric water vapor content (total precipitable water) should be made using Fig. 1A-22b. For the F-1, F-2, and F-3 spacecraft use Graph A; for the F-4 and subsequent spacecraft use Graph B. These curves show that the correction for water vapor attenuation is important for surface temperatures greater than 280° K.

An improved version of the Block 5D spacecraft, called the Block 5D-2, is used on the F-6 and later flight vehicles. The Block 5D-2 spacecraft (1) carries the same OLS system as the Block 5D, (2) is larger in size and is able to carry a larger, non-OLS sensor payload, (3) has a greater redundancy of systems, (4) has a computer memory twice the size of that on the Block 5D, and (5) has a 36 month in orbit lifetime as opposed to the 18 month in orbit lifetime of Block 5D.

In addition to the Block 5D-2, plans for a Block 6 spacecraft (first launch 1984) are currently in the development stage. This series spacecraft is being designed to satisfy both the military and civilian environmental data needs and to provide a growth capability so that several additional sensors can be incorporated.

For further information on DMSP contact:

Navy Space Systems Representative
SAMSO/YDN
P.O. Box 92960
Worldway Postal Center
Los Angeles, California 90009

Additional information on the Block 5C and Block 5D Systems can be found in Volume 1 of this series.

References

Dickinson, L.G., S.L. Boselly III, and W.S. Bergmann, 1974: Defense Meteorological Satellite Program (DMSP) User's Guide. AWS-TR-74-250. Air Weather Service, United States Air Force, Scott AFB, 109 pp.

Nichols, D.A., 1975: Block 5D Compilation. Headquarters, Space and Missile Systems Organization, Air Force System Command, United States Air Force, 522 pp.

Sample Imagery, DMSP

These simultaneous DMSP images show the cloud cover and thermal features over western Europe and northwestern Africa. In the visible picture (Fig. 1A-24a), there is a small vortex over the western Mediterranean and an extensive area of cloudiness over France and Great Britain. The corresponding infrared picture (Fig. 1A-25a) reveals that this cloudiness is low-level stratus or fog and also shows that there is considerable convective activity over the western Mediterranean ahead of the vortex.

SYSTEM ID SVROTA: FTV 1535; AM; ASCEND REV 6961; RT; DATE 78-015; TR 10:54:13; DATA TYPE LF 6 BIT; SCALE X1; MIDPNT 0800 NM
DATA MOD: L-LOW ; TN 10:51:13; LN 350.89; ROLL +.000; ALT 459.7; SYS POS: LAT +36/LONG 006; +IMAGE; NE
15JAN78 35N=0.5EAST TAPE# 015-5

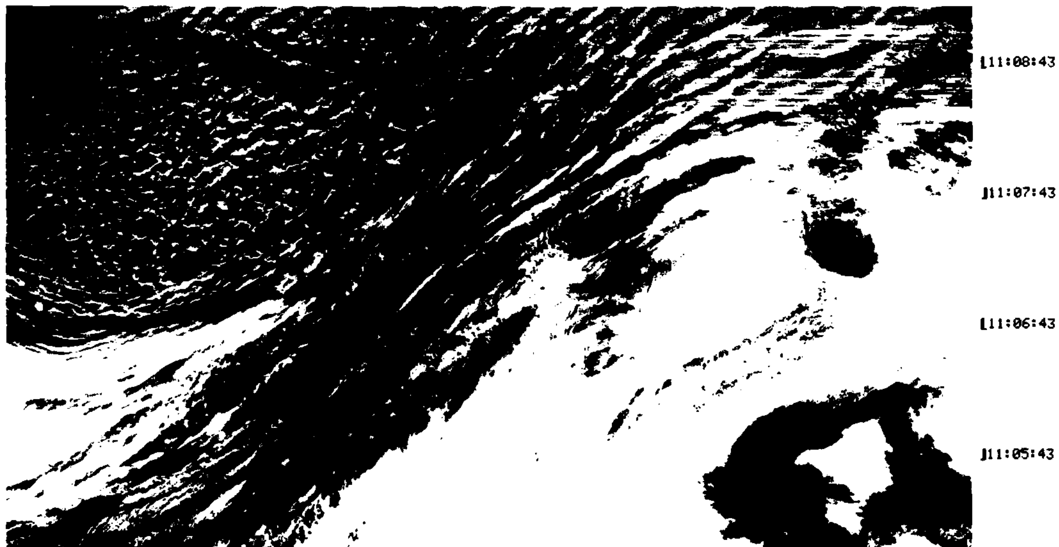

1A-24a. F-1. DMSP LF Low Enhancement. 1051 GMT 15 January 1978.

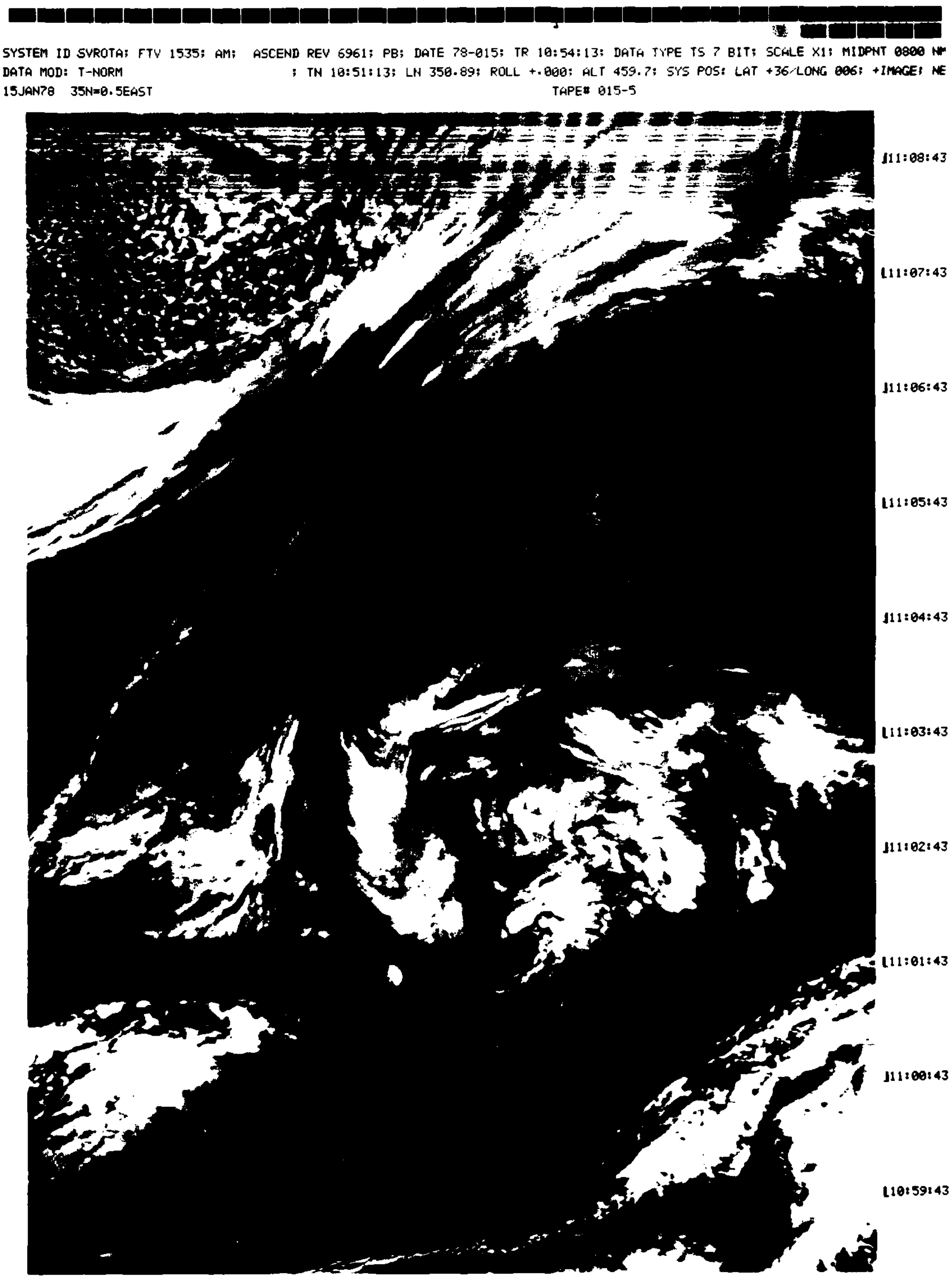

1A-25a. F-1. DMSP TS 1-Normal, 1051 GMT 15 January 1978.

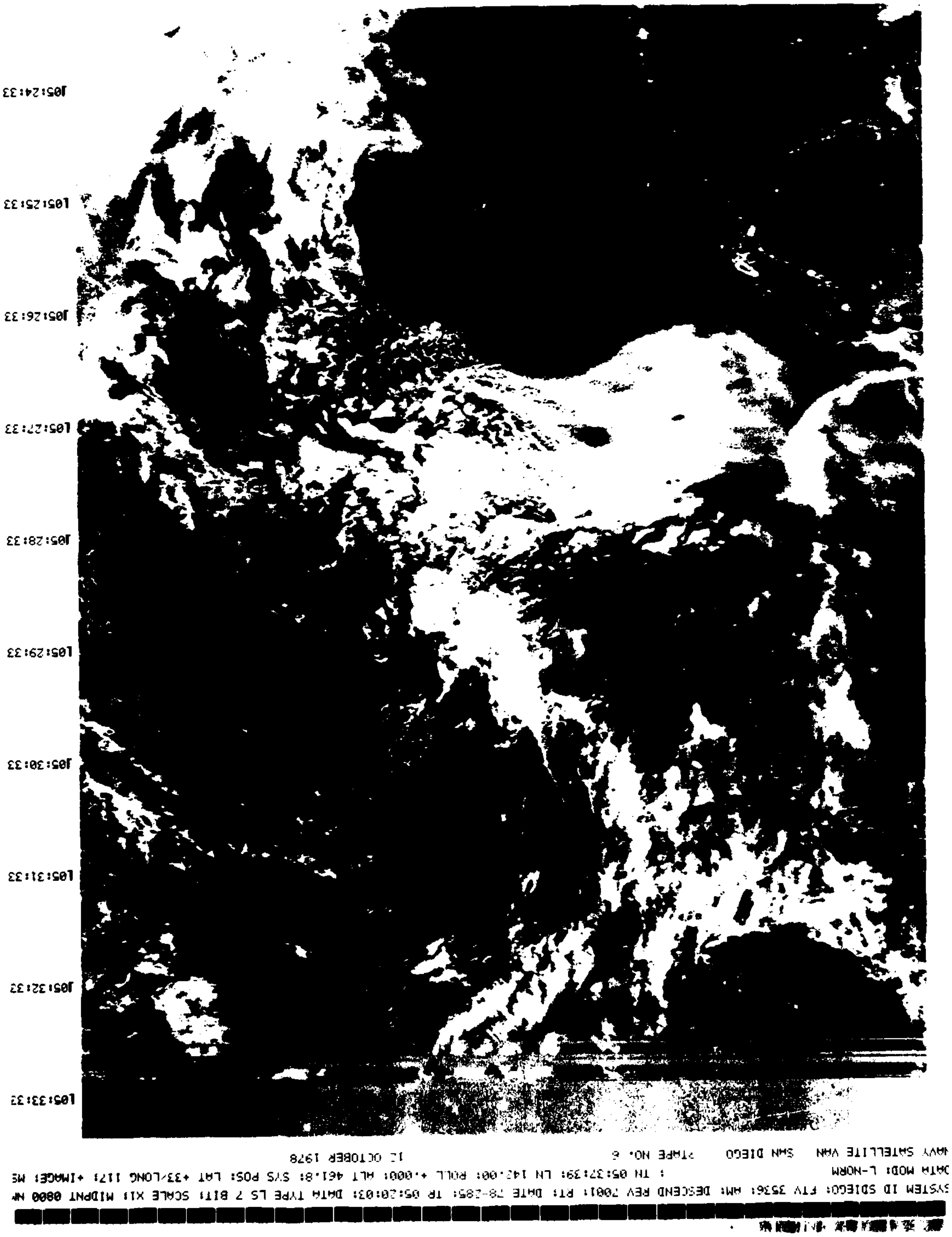

1A-26a. F-2. DMSP LS Nighttime, Descending Node 0537 GMT 12 October 1978.

Figs. 1A-26a and 1A-27a are simultaneous visible and infrared images showing the U.S. West Coast. The nighttime visible picture reveals the lights of the major metropolitan areas as well as cloud patterns over the eastern North Pacific. Note the granular texture of the image at the right and left edges. This is caused by the reduction of the nighttime visible sensor's aperture which is necessary to keep the along scan resolution nearly constant.

The infrared picture has been enhanced to display sea surface temperature gradients along the coast. This type of enhanced imagery is useful for oceanographic and air-sea interaction studies.

1A-27a. F-2. Enlarged View. DMSP TF (Special Table A). Descending Node. 0537 GMT 12 October 1978.

1B Geostationary Satellites

Geostationary Satellite System

Five meteorological satellites in geostationary orbit (altitude 35,800 km) are to be maintained continuously on station above the equator, at intervals of about 70° longitude around the globe. Fig. 1B-1a shows the satellite subpoint position and areal coverage of each satellite. As can be seen, this system will give continuous coverage of the Earth except for the polar regions.

The geostationary satellite system provides (1) data in the visible, water vapor (METEOSAT only), and infrared modes, (2) real-time transmission of these data (reformatted) to users, (3) relay of conventional meteorological data from remote data collection platforms to users, and (4) transmission of conventional meteorological charts via the satellite to users.

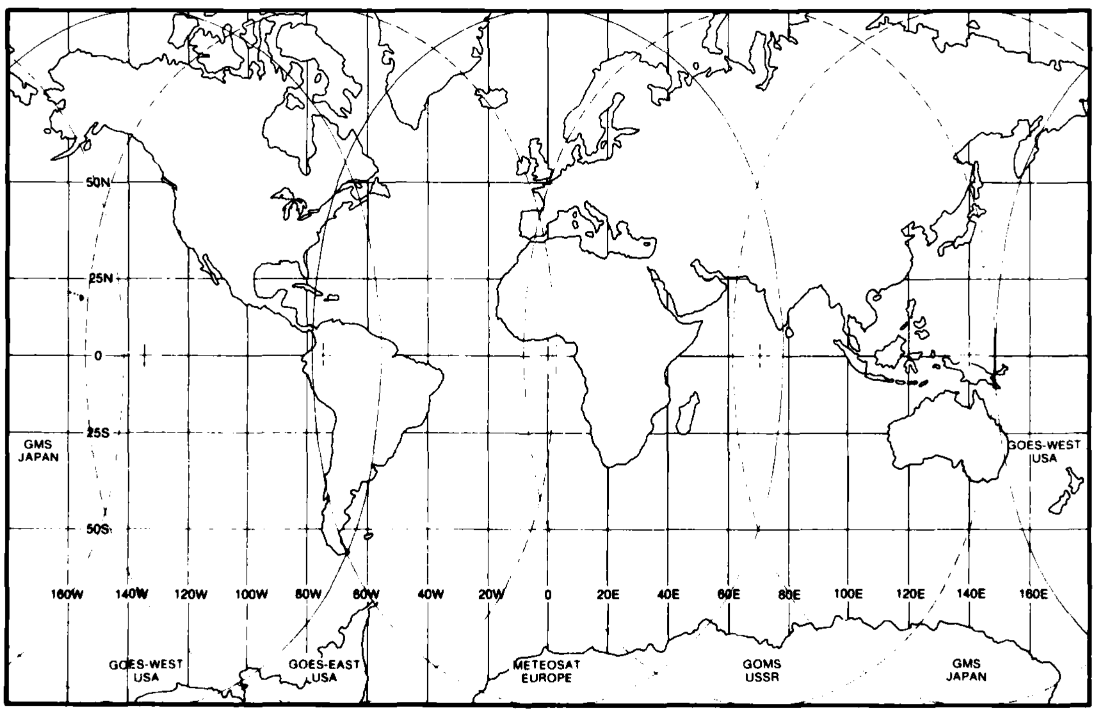

1B-1a. Satellite subpoint position and areal coverage of the geostationary satellites. GOMS is not yet in orbit.

Earth Scanning Technique

The GOES, GMS, and METEOSAT spacecraft utilize a scanning radiometer telescope for obtaining visible, infrared, and water vapor data. The same principle for Earth scanning is used on each spacecraft; that is, horizontal lines of data are generated by a telescope imaging device looking out of the side of the spacecraft as it spins on an axis oriented parallel to the spin axis of the Earth. Successive contiguous lines are obtained by stepping the telescope in discrete increments (north-south) on successive rotations of the spacecraft. One rotation of the spacecraft generates one line of infrared data (plus one line of water vapor absorption band data in the case of METEOSAT) and either 2, 4, or 8 lines of visible data. A scan of the full Earth disc is accomplished in either 18 minutes (GOES) or 25 minutes (GMS and METEOSAT). Since it takes several minutes for the telescope to retrace to the starting position, a new full disc image can only be generated every thirty minutes. In addition to the normal scan mode, the telescope can be placed into a limited scan mode. In this mode, the north-south motion of the telescope is limited to a fewer number of line scans. This reduces the area of coverage, but increases the frequency of imaging.

The major characteristics of the geostationary imaging radiometers are listed in Table 1B. Note that METEOSAT is the only spacecraft that has a water vapor channel and the scan mode for METEOSAT is east-west and south-north, which is opposite to the scan mode used on the GOES and GMS.

TABLE 1B
GEOSTATIONARY SATELLITE RADIOMETER SUMMARY

		GOES	GMS	METEOSAT
Spin Rate (RPM)		100		
Line scan direction		W-E		E-W
Telescope step direction		N-S		S-N
Number of scan lines for full disc IR		1821	2500	
Number of VIS detectors		8	4	2
Resolution at SSP	VIS IR WV	0.5 n mi 5 n mi —	0.7 n mi 2.8 n mi —	1.4 n mi 2.8 n mi 2.8 n mi
Full disc scan time, minutes		18.21	25	
Sensor type	VIS IR	Photomultipliers Hg Cd Te		Si Photo Diode Hg Cd Te & WV
Spectral Response (μm)	VIS IR WV	0.55-0.75 10.5-12.5 —		0.4-1.1 10.5-12.5 5.7-7.1

Determination of Ground Spatial Resolution

The ground spatial resolution of a geostationary satellite image degrades with distance away from the satellite subpoint (SSP) due to the curvature of the Earth's surface when viewed from geostationary altitude (Glover, 1974). Fig. 1B-3a gives small circle arcs of normalized resolution degradation as a function of the resolution at the satellite subpoint (R_{SSP}). The figure shows that from the SSP to about 42° of arc away from the SSP the resolution degrades to 1.5 R_{SSP}. Beyond 42° of arc from the SSP the resolution degrades rather rapidly.

To determine the ground spatial resolution of the imagery from a particular satellite at a given location, plot the location relative to the latitude/longitude of the satellite subpoint and then multiply the subpoint resolution by the appropriate factor. For example, Monterey (x in Fig. 1B-3a) is at 37° N, 122° W relative to GOES-West subpoint at 0° N, 135° W. This gives a factor of approximately 1.4 R_{SSP}. Since GOES-West resolution at the SSP is 0.5 n mi for visible imagery and 5 n mi for infrared imagery, the resolution at Monterey is 0.7 n mi for visible imagery and 7 n mi for infrared imagery.

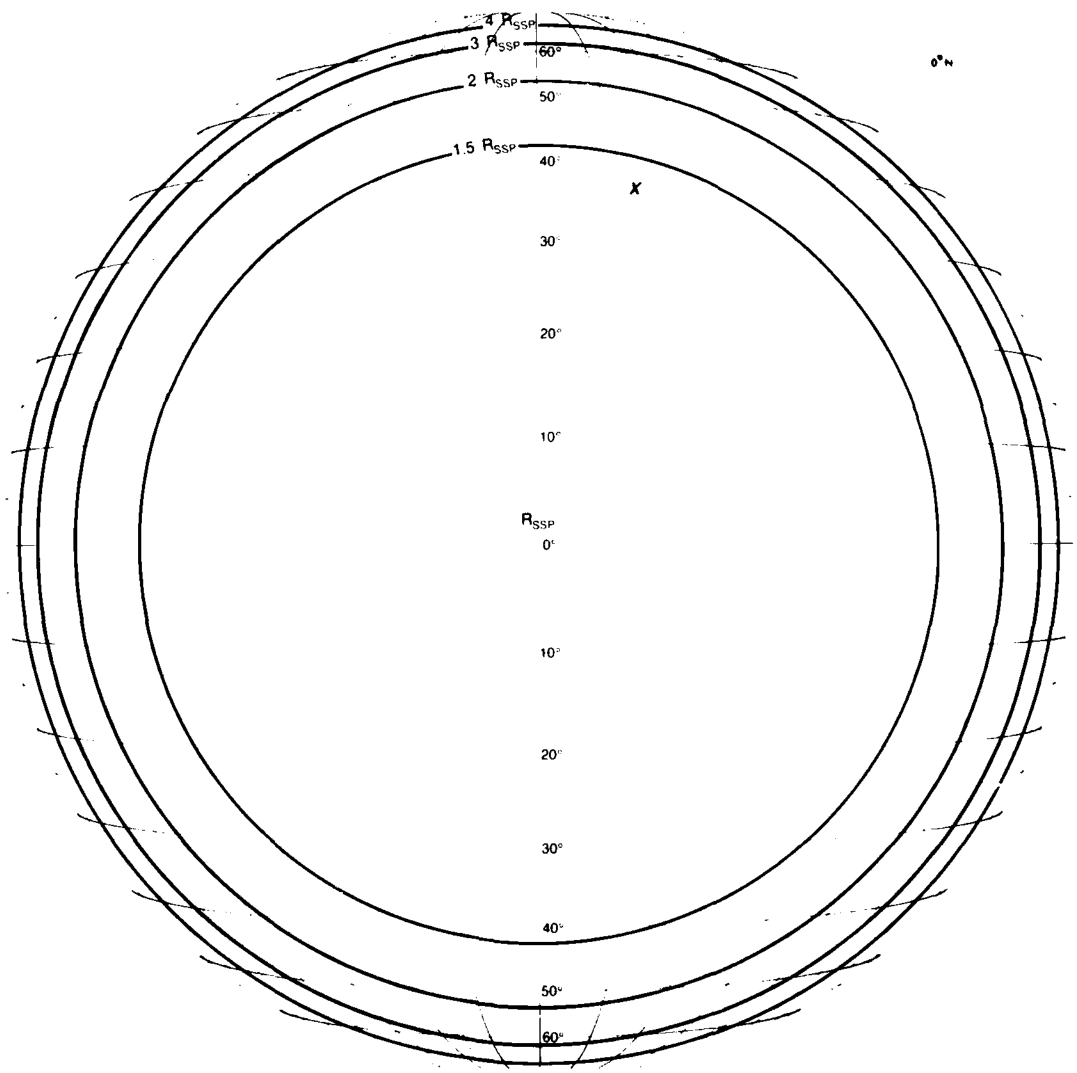

1B-3a. Determination of ground spatial resolution.

Reference

Glover, J.C., 1974: Degradation of resolution in GOES imagery with distance away from the subsatellite point. Unpublished Manuscript, NOAA/NESS, 4 pp.

Cloud Top Location Corrections

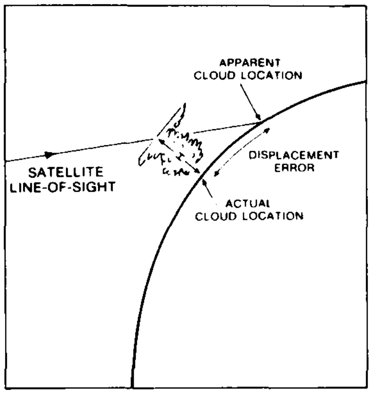

1B-4a. Schematic illustrating an actual verses apparent cloud location.

Because the Earth's surface curves rapidly away from the geostationary satellite line-of-sight (Fig. 1B-4a), a cloud top at height H appears to be displaced from its actual position (NWS, 1977 and Weiss, 1978). For a cloud located precisely over the satellite subpoint, the apparent and actual cloud positions coincide, but the distance between the apparent and actual cloud positions (displacement error) increases in a direction away from the subpoint as the cloud's distance from the subpoint increases. The amount of the correction is also a function of cloud top height.

Fig. 1B-4b shows the calculated lines of equal displacement error for a 40,000 ft cloud top. An adjustment for cloud tops at other heights can be made as the error is essentially a linear function of height and would be 50% greater for a 60,000 ft top and 50% less for a 20,000 ft top. To correct for the displacement error and obtain the actual cloud top location, move the cloud top the amount of the error in a radial direction towards the satellite subpoint.

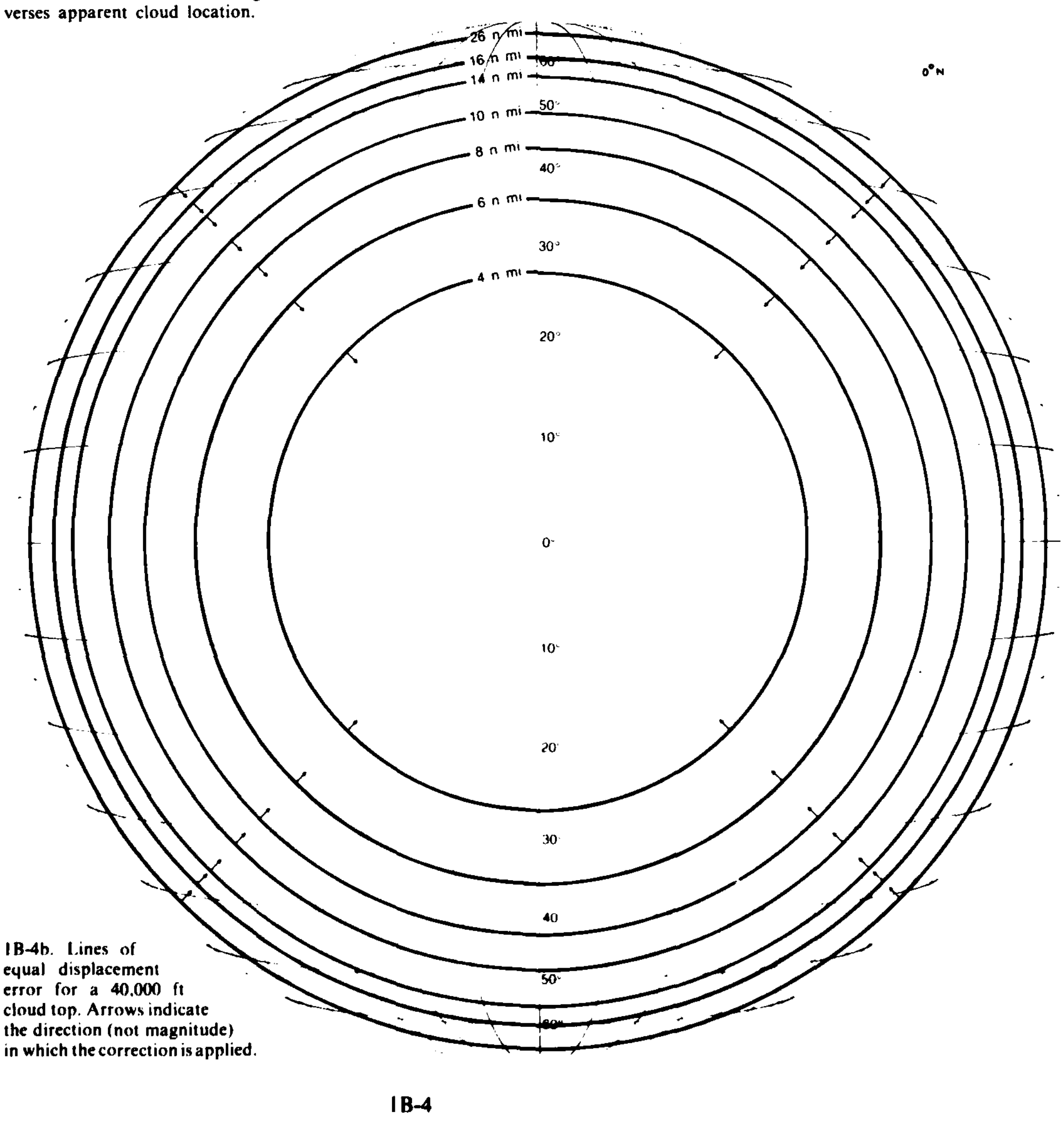

1B-4b. Lines of equal displacement error for a 40,000 ft cloud top. Arrows indicate the direction (not magnitude) in which the correction is applied.

Image Distribution

The Panel on Meteorological Satellites (WMO, 1975) has worked with the multi-national sponsoring agencies developing geostationary satellite systems so that the modes of satellite data transmission to users are functionally similar. Thus, all spacecraft types (United States-GOES, Japan-GMS, Europe-METEOSAT, Soviet Union-not yet in orbit) make weather facsimile (WEFAX) transmissions on a common frequency.

In addition to WEFAX transmissions, each spacecraft type has another image distribution system. In the United States, a system called GOES-TAP uses surface, high-quality telephone lines to provide visible and infrared imagery for a wide variety of users. The European system has two fully independent spacecraft data transmission channels so that raw image data, high resolution facsimile data, and WEFAX data can be transmitted simultaneously. In contrast, these three data transmission functions must be time-shared in the Japanese system.

For naval operations, U.S. Department of Defense communication centers around the world provide radio facsimile transmissions of geostationary satellite imagery. The radio facsimile products are similar to the WEFAX products and ships can receive radio facsimile transmissions up to several hundred miles out to sea.

Data Display

In the field, geostationary satellite imagery transmitted on WEFAX or radio facsimile is usually displayed as hardcopy (film print or transparency). Current hardcopy display equipment converts analog data transmissions into discrete gray shades to provide a visual product. These image display devices are readily available, permitting wide distribution of the image products to operational users.

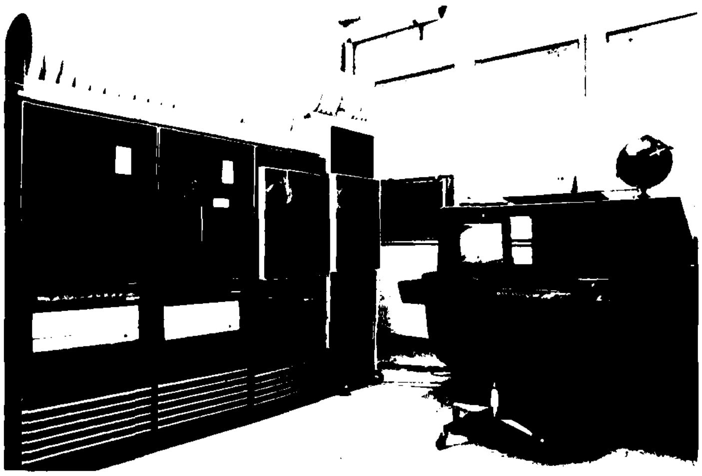

1B-5a. Digital data display systems, such as the Naval Environmental Prediction Research Facility's Satellite Processing and Display System (SPADS), are currently under development. These systems will enable the user to obtain real-time winds from cloud motions, derived fields of motion, and false color enhancement of the imagery for highlighting selected phenomena. The user will also be able to superimpose conventional meteorological data and analysis on the satellite imagery and make time-lapse loops of a series of geostationary satellite pictures. These systems permit great flexibility in monitoring atmospheric and oceanographic phenomena in a quantitative manner.

References

NWS Central Regional Technical Attachment No. 77-G4, April 1977. Displacement error of satellite and tops. 4 pp.

Weiss, C.E., 1978: Cloud-location corrections near the horizon of an SMS image. Satellite Application Information Note 78 8, NWS NESS, U.S. Dept. of Commerce, Washington, D.C., 8 pp.

World Meteorological Organization, 1975: World Weather Watch Global Observing System Satellite Sub-System Information on Meteorological Satellite Programmes Operated by Members and Organizations. UNIPUB, New York, New York, 74 pp.

Universal Latitude/Longitude Grid

This universal grid can be used with any geostationary satellite imagery. Make an acetate copy to the desired size and label the latitudes and longitudes (dark lines appear every 10°) from the satellite subpoint.

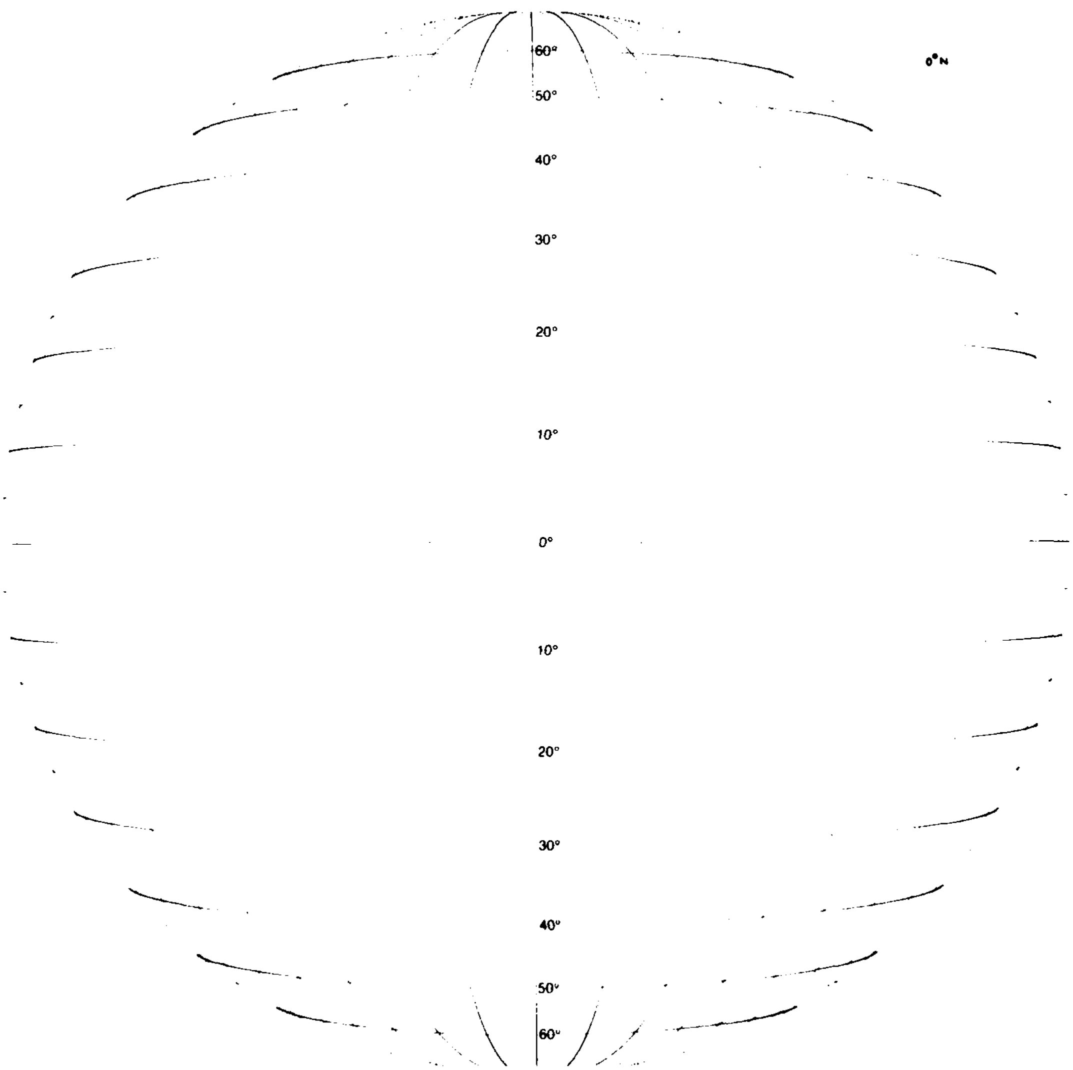

Geostationary Operational Environmental Satellite
(GOES)

The United States currently operates two geostationary satellites, GOES-East with a satellite subpoint position at 75° W, 0° N and GOES-West with a satellite subpoint at 135° W, 0° N. GOES-East gives an areal coverage from Antarctica to Greenland and from Africa into the eastern Pacific, while GOES-West areal coverage extends from Antarctica to Alaska and from the western Americas to the western Pacific.

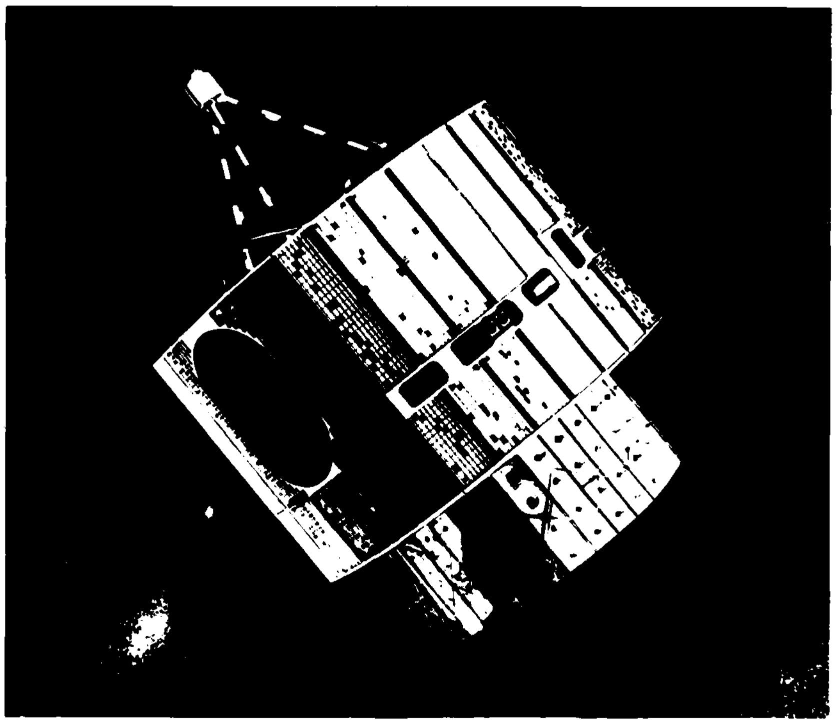

IB-7a. The main body of the GOES spacecraft is cylindrical, about 75 inches in diameter, with an aperture in the side through which the radiometer telescope views the Earth. The outside of the spacecraft is covered with solar cells which supply power. Attached to the main body is a smaller cylinder supporting multiple elements of combined S-band and UHF antenna.

Image Acquisition and Distribution

The National Environmental Satellite Service (NESS) of NOAA has implemented a central data distribution system to receive, process and distribute GOES visible and infrared spin scan radiometer (VISSR) data to users in near real-time. The VISSR data flow diagram (Fig. 1B-8a) shows the system for communicating the image data to various users at several locations.

The GOES image distribution system begins with the acquisition of raw VISSR image data from the spacecraft by the Command and Data Acquisition (CDA) station at Wallops Island, Virginia. These data are received during the time that the radiometer views the Earth (approximately 20° of one full rotation). In the CDA, the raw VISSR data are processed in a synchronizer/data buffer (line stretcher) which reduces the bandwidth required for retransmitting the data. These stretched data are then retransmitted through the spacecraft and on to users during the remaining 340° of spacecraft rotation. Although the stretched data are transmitted at a slower rate than the raw data, quite sophisticated reception equipment is still required to receive it.

In addition, the lower data rate infrared imagery is formatted in the CDA for direct analog transmission via high quality telephone lines to Satellite Field Services Stations (SFSS), and for digital transmission via a special landline to the NESS Central Data Distribution Facility (CDDF) at Camp Springs, Maryland.

The NESS central facility, located at Suitland, Maryland, receives the stretched VISSR data from the satellite for in-house use and also relays the data via dedicated microwave link to the CDDF. The NESS-Suitland facility also receives infrared imagery via special landline for use by the NOAA/NESS large scale data processing facility.

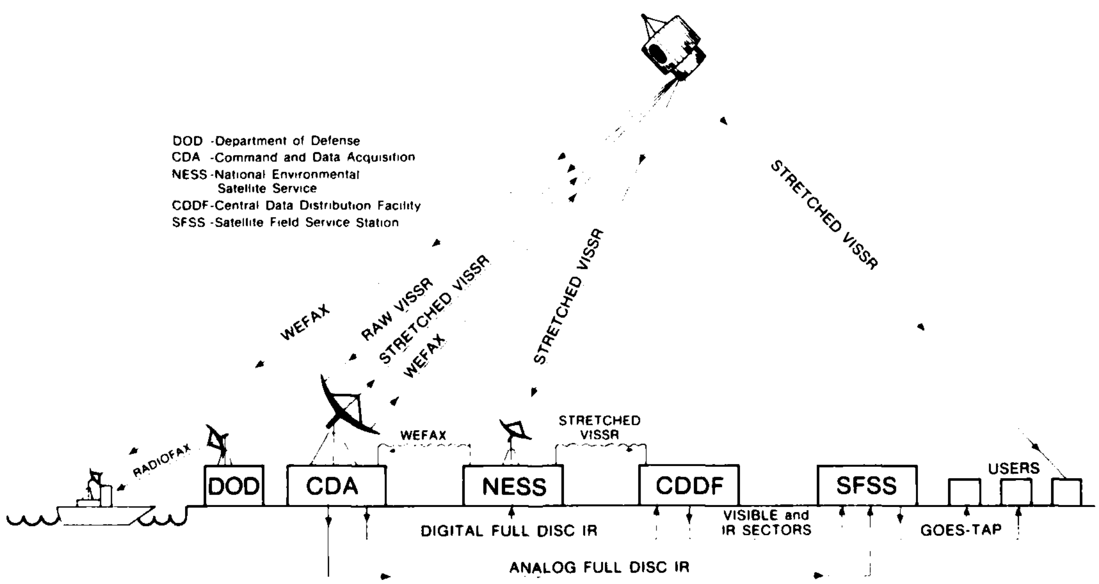

1B-8a. GOES Central Data Distribution System.

At the CDDF, a series of sectorizer units select and convert geographical areas of the full disc visible image into analog form, and subsequently make an analog transmission of the sectorized data to SFSS's. This data distribution system is called GOES-TAP. The sectors consist of specified geographical areas and have resolutions of 0.5, 1, or 2 n mi. The sectorizer operates in a serial fashion (i.e., it does not have the capability of receiving and transmitting data simultaneously) which causes the transmission of the sectors from the CDDF to be on a near real-time rather than real-time basis. The average data user in the United States requires data only in the Northern Hemisphere. Because of this, the sectorizer utilizes only 9 minutes of the 18 minute full disc imaging interval to receive the data. Approximately 17 more minutes are required for handling and transmission of the sectors, making it possible to complete the processing and transmission of the sectors well within the 30 minute interval between successive full disc VISSR readouts. Numerous sectors cover the contiguous 48 states, Alaska, and the western North Pacific to about 170° E. All standard sectors have automatically implanted geographical grids.

Infrared data are also sectorized at the CDDF to provide equivalent infrared sectors with the same geographical coverage as the 1 n mi resolution visible sectors. This facilitates the comparison of visible and infrared imagery. The CDDF also has the capability of temperature (infrared) enhancement to highlight selected features in the imagery (e.g., sea surface temperatures, severe storm cloud top temperatures, etc.).

The SFSS's receive sectorized data from the CDDF and the full disc infrared data from the CDA over high quality telephone lines. Since only one sector at a time can be transmitted over a single line, several lines to each SFSS are needed for simultaneous transmission of several sectors. A user in line with a SFSS may receive any one of the standard sectors available to the SFSS every 30 minutes. The user may vary his choice of sectors so long as he remains within the data set available to the SFSS to which he is connected.

Ships or remote land stations within a 60° small circle arc of the satellite subpoint may receive imagery on the WEFAX channel. The WEFAX data are centrally produced by the NOAA computers in Suitland, Maryland, and then transmitted through the spacecraft and on to users from the CDA. Since WEFAX broadcasts are on the same frequency as the stretched VISSR data, WEFAX broadcasts are scheduled only in the 12 minute interval between successive VISSR readouts.

The WEFAX product line consists of both visible and infrared full disc imagery transmitted in sections or chips. Each chip requires slightly more than four minutes for transmission. Complete full disc coverage in both the visible and infrared channels (at 4 n mi resolution at satellite subpoint) requires the transmission of four chips. Each chip covers an area from the equator to 60° N (or S) latitude, and 60° E (or W) from the central longitude. Requests for information on ground equipment requirements, data reception, and WEFAX products and schedules may be addressed to:

Coordinator, Direct Readout Services, S131
National Environmental Satellite Service
National Oceanic and Atmospheric Administration
Washington, D.C. 20233

Sensor System Description

At the spacecraft (Fig. 1B-10a), radiation from the Earth image scene enters an aperture and is reflected 45° by an object-space scan mirror. This mirror is an elliptically-shaped plane mirror that is tilted about its axis to obtain the north-south scan steps. Radiation reflected from the scan mirror enters a Cassegrain telescope (primary and secondary mirrors) which focusses the radiant energy onto the detector array.

At the detector array, visible spectrum energy is collected by eight fiber optics and passed on to eight separate photomultiplier tubes (PMT's) which respond in the 0.55–0.75 μm range. Each PMT has an instantaneous field of view (IFOV) of 0.021 by 0.025 milliradians which gives a spatial resolution at the satellite subpoint of approximately 0.5 n mi. On-board the spacecraft, the voltage output from each PMT is converted to one of 64 digital count values proportional to the amount of reflected solar radiation received. A conversion in the digital count is made so that there is more contrast between dark objects in the imagery (terrain features) than in light objects in the imagery (highly reflective clouds).

Thermal infrared imagery is also relayed and filtered from the detector array to two identical (one active, one backup) infrared detectors. The detectors are mounted on a plate that is passively cooled by a radiation device to a controlled temperature of 95° K so as not to interfere with detected Earth scene radiation. Optical filters pass only radiation in the 10.5–12.5 μm region. Each infrared detector has an IFOV of 0.192 by

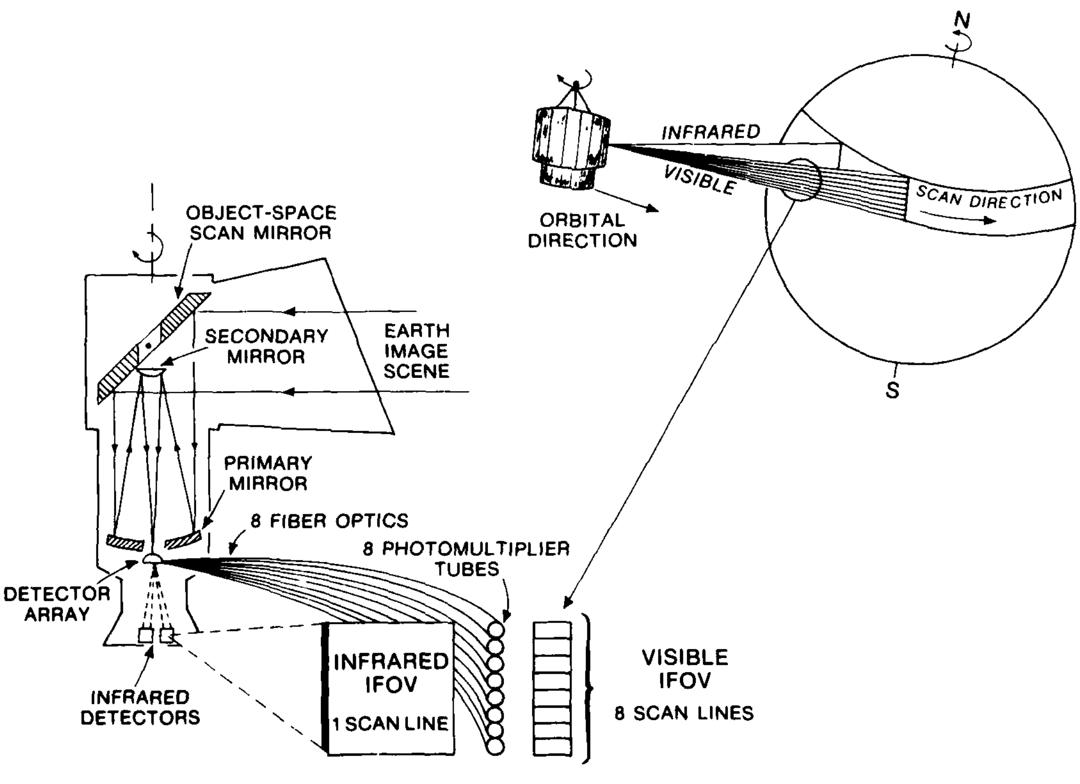

1B-10a. Schematic of the GOES VISSR optics.

0.192 milliradians which gives a spatial resolution of 5 n mi at the satellite subpoint. In order to better define sharp temperature gradients, the infrared detector is oversampled in the along scan direction resulting in a 50% overlap in the IFOV of adjacent samples. Although these data are displayed as 5 by 2.5 n mi rectangles, the instantaneous resolution remains 5 by 5 n mi.

The infrared detector output is normalized in terms of the equivalent blackbody temperature of the radiating object so that the detector output is a simple, nearly-linear function of scene temperature. The infrared temperature sensitivity is a 0.5° K change in the range from 330–242° K, and a 1.0° K change from 242–163° K. The NETD of the GOES is a 0.3° K change across the entire temperature range sensed.

Spectral Characteristics

The GOES spacecraft carries a VISSR which measures reflected solar radiation in the 0.55–0.75 μm wavelength region during daylight and emitted Earth, atmosphere, and cloud radiation in the 10.5–12.5 μm wavelength region day and night. The normalized sensor response curve of the GOES visible channel is shown in Fig. 1B-11a. Comparison of this sensor's response curve with the color spectrum of visible light reveals that the sensor has no response in the blue light region (<5 μm). This eliminates the effects of blue light backscattering of the atmosphere. The peak response of the sensor is in the green and red portions of the visible spectrum with the response decreasing, but extending slightly into the near infrared. Imagery obtained from this sensor is used for daytime mapping of the Earth's surface and cloud cover.

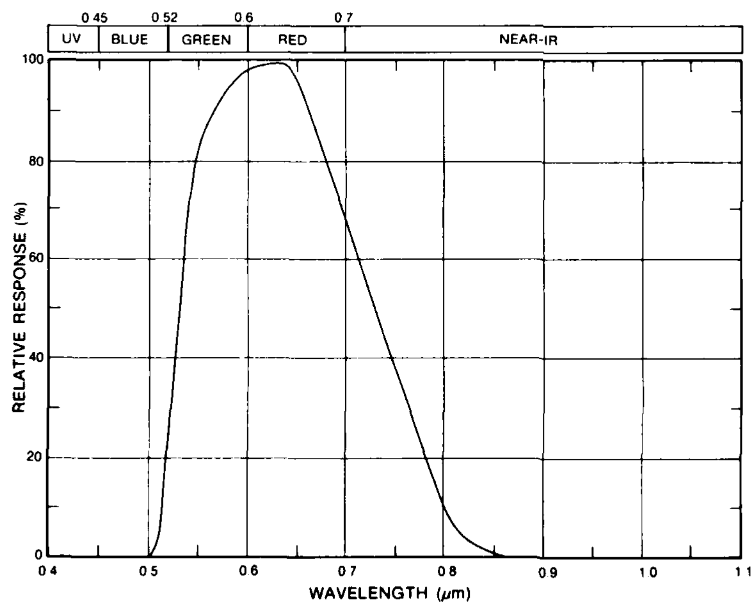

1B-11a. GOES visible channel normalized sensor response curve.

Imagery obtained from the VISSR infrared sensor is used for determining the temperature of the radiating surface and for continuous

cloud cover mapping day and night. The normalized response curve of the GOES infrared sensor is shown in Fig. 1B-12a. The 10.5-12.5 μm range is used because it contains the peak radiations emitted by the Earth and its atmosphere and also because it is within an atmospheric window more transparent than other adjacent wavelengths to outgoing radiation. When examining infrared imagery qualitatively and quantitatively, it is important to note that thermal infrared radiation in this range is attenuated by water vapor, aerosols, carbon dioxide and ozone. Depending on atmospheric conditions then, the Earth's surface temperature can appear to be 1-10° K lower at the satellite sensor. The temperature corrections are estimated to range from 1.0-10.0° K for water vapor, 0.1-1.0° K for aerosols, and 0.1° K for carbon dioxide and ozone. Although there is no absolute calibration of the infrared sensors on GOES, data corrected for atmospheric attenuation have verified well with ground truth and appear consistent.

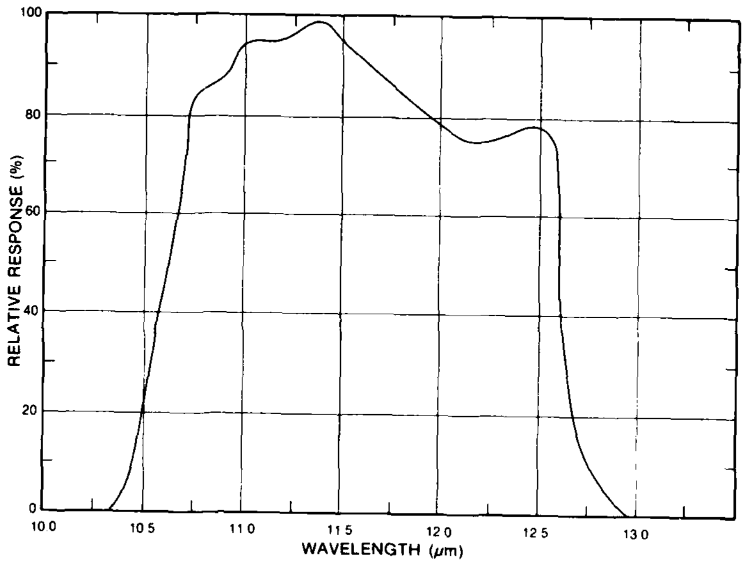

1B-12a. GOES infrared channel normalized sensor response curve.

For additional information on the GOES spacecraft, contact:

National Climatic Center
Satellite Data Services Division D56
World Weather Bldg., Room 606
Washington, D.C. 20233

References

Bristor, C.L., 1975: Central processing and analysis of geostationary satellite data. NOAA Tech. Memo. NESS 64, U.S. Dept. of Commer., Washington, D.C., 155 pp.

Corbell, R.P., C.J. Callahan, and W.J. Kotsch, 1976: The GOES/SMS Users Guide. Management and Technical Services Company, Rep. No. NAS 5-20694, 118 pp.

Figs. 1B-14a and 1B-15a are examples of simultaneous visible and infrared pictures from the GOES-East spacecraft during the northern hemisphere winter. The visible picture shows sunglint off the northwest coast of South America, considerable cloudiness over much of the Atlantic and Pacific Oceans, and a large clear area behind a cold frontal cloud band off the U.S. East Coast. The infrared picture reveals the strong thermal boundaries of the Gulf Stream, upwelling of cold water in the Gulf of Tehuantepec, and the relative heights (temperatures) of the clouds. The brightest clouds are the highest and coldest, while the medium gray clouds are lower and warmer. The land masses are the darkest and warmest.

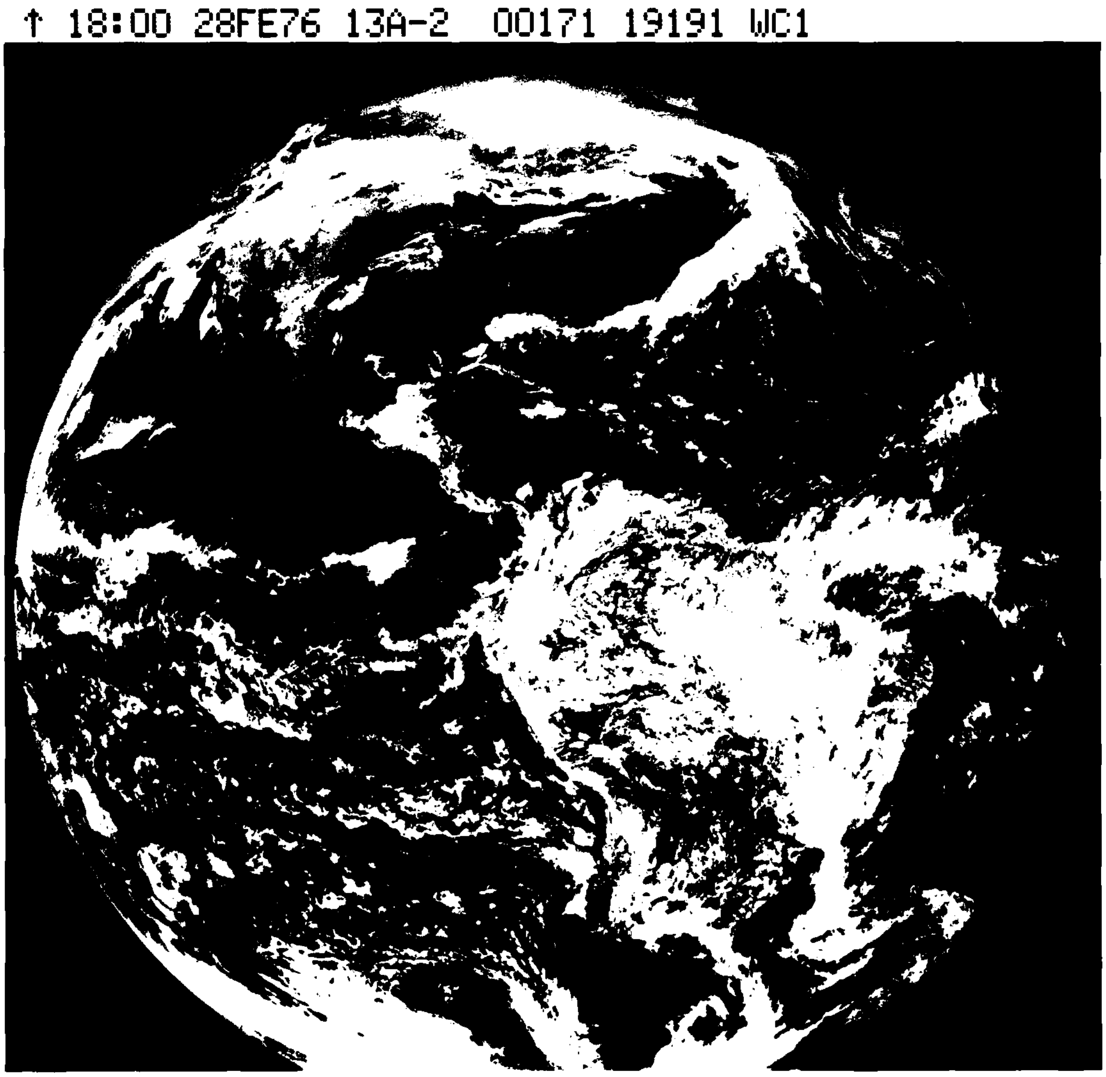

1B-14a. GOES-E. Visible Picture, 2 n mi Resolution, 1800 GMT 28 February 1976.

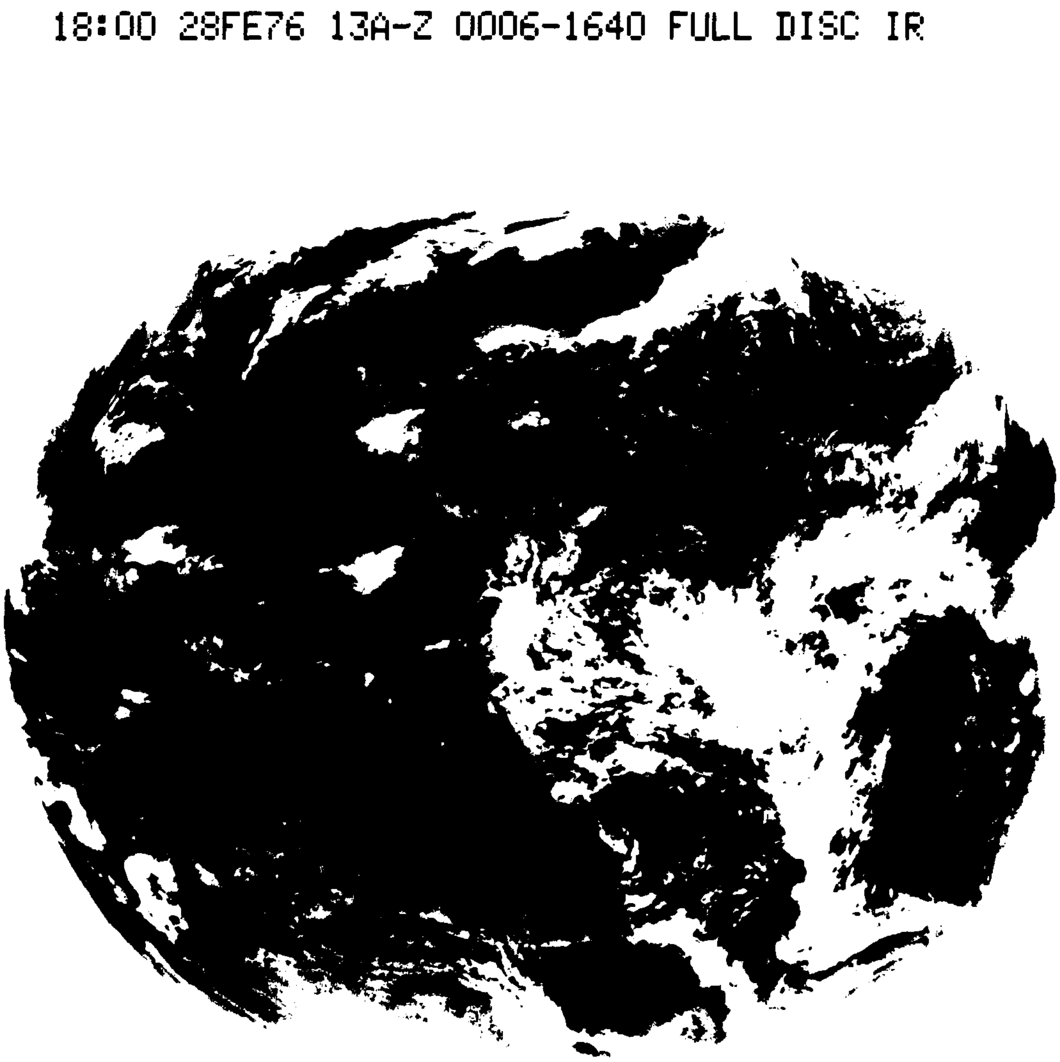

1B-15a. GOES-E. Infrared Picture, 5 n mi Resolution. 1800 GMT 28 February 1976.

Figs. 1B-16a and 1B-17a are simultaneous views of the Earth from GOES-West. The western portion of North America appears in the upper right corner, while the wide expanse of the Pacific Ocean is visible beneath the cloud free skies in the remainder of the picture. Cirrus cloudiness associated with the subtropical jet stream stands out well in the infrared picture, but is difficult to distinguish in the visible. The large area of cellular cloudiness west of Baja California occurs in the northerly flow around the high pressure area over the western North Pacific.

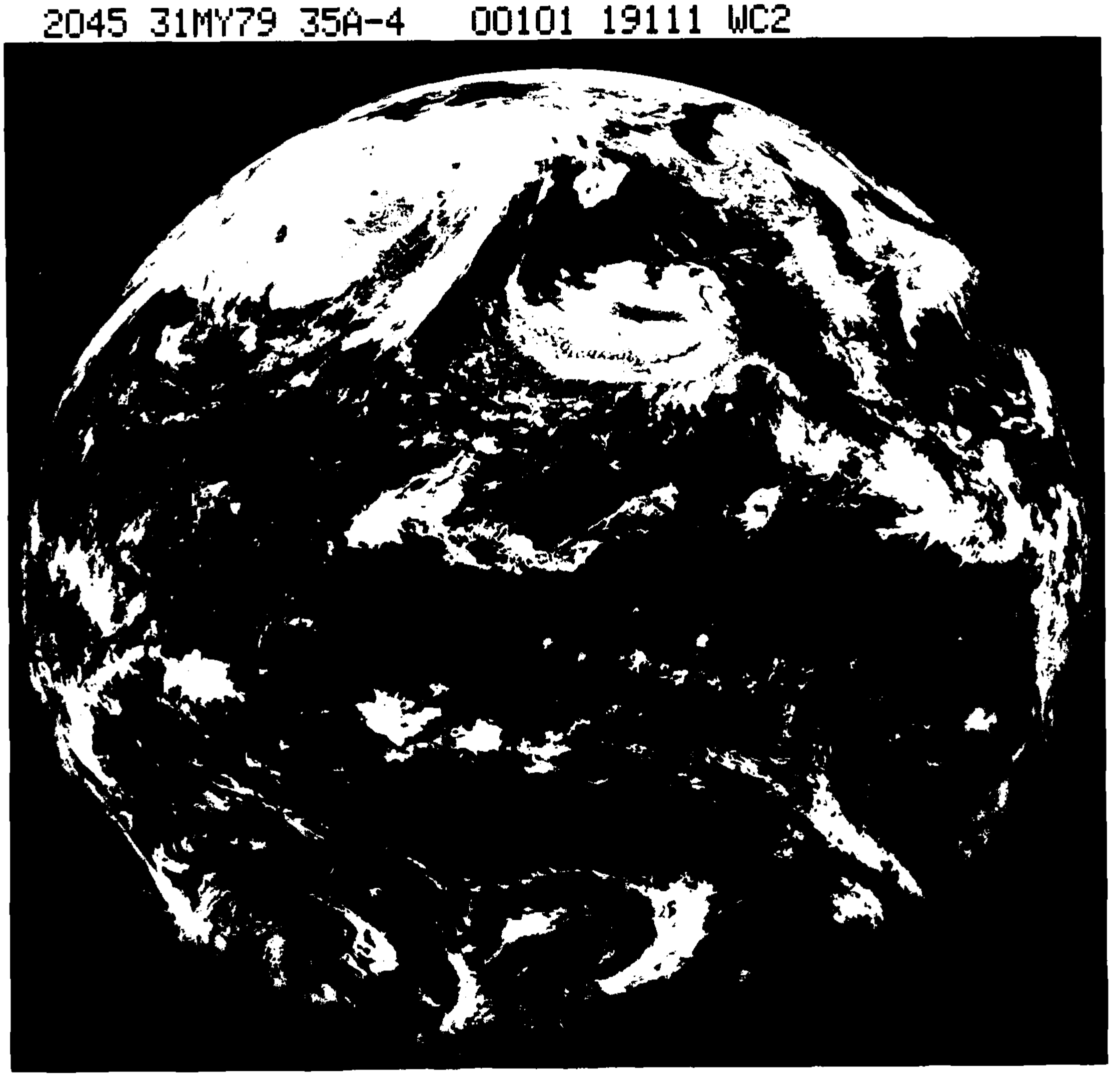

1B-16a. GOES-W. Visible Picture, 2 n mi Resolution, 2045 GMT 31 May 1979.

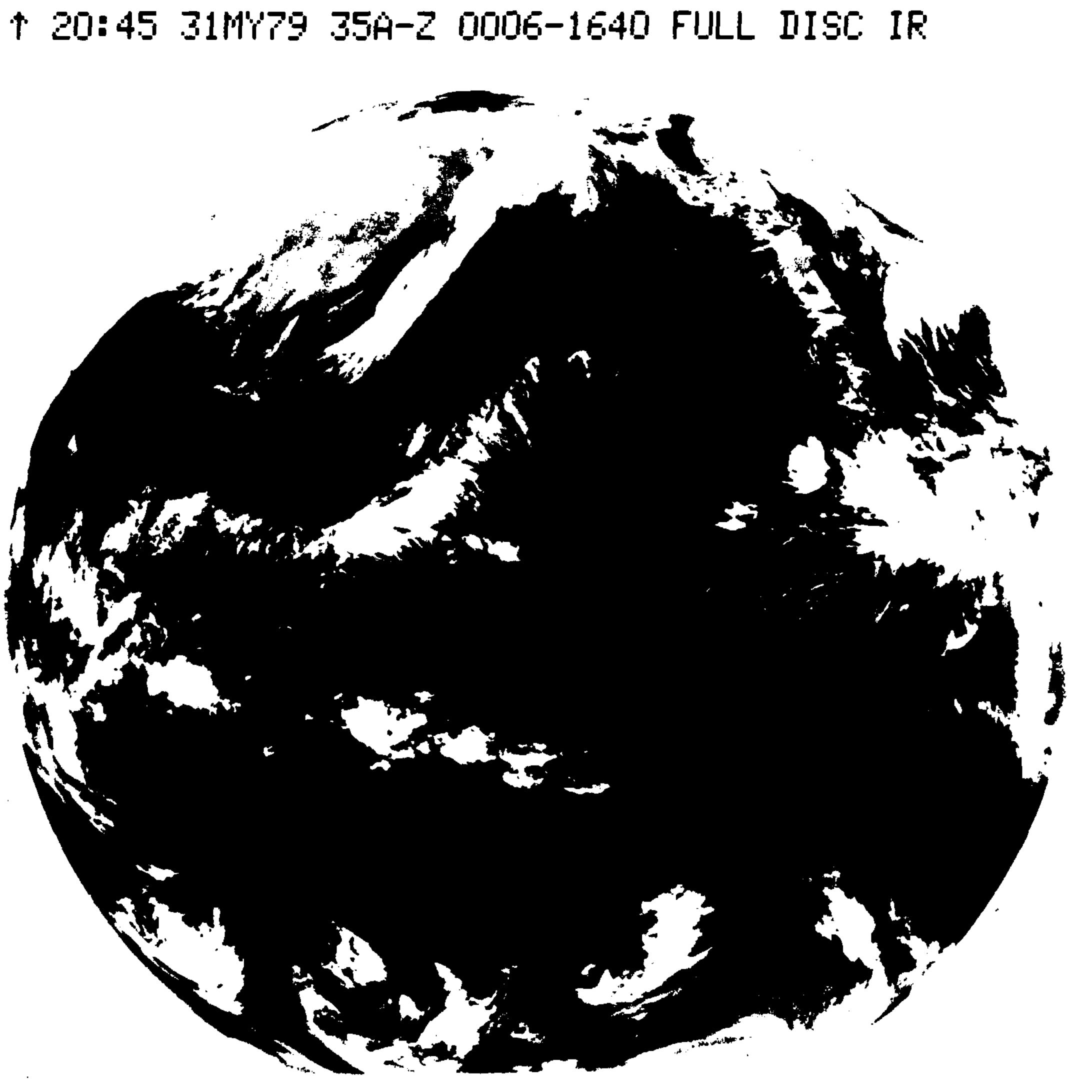

1B-17a" GOES-W. Infrared Picture, 5 n mi Resolution. 2045 GMT 31 May 1979.

GOES IMAGERY CODED IDENTIFICATION HEADER

GOES HEADER	1230	27JN79	12A-2	01044	18162	DB5	
Coding Elements	a	b	c d e f g	h	i	j k	(sector identification see below)

Coding Elements

a Greenwich time in hours and minutes indicating time of actual picture start.

b Calender day, month, and year.

c Line stretcher/data buffer identification:

Identifier	Satellite
1	GOES-East
2 or 3	GOES-West

d Satellite Identification:

Identifier	Satellite
1	SMS-1
2	SMS-2
3	SMS-3
4	GOES-2
5	GOES-3

e Image type:

Identifier	Image type
A,B,C,D	Visible sectors
E	Equivalent IR sector
A-Z	Full-disc IR

f Image resolution:

Identifier	Resolution
1	0.9 km x 0.9 km (0.5 n mi x 0.5 n mi)
2	1.8 km x 1.8 km (1 n mi x 1 n mi)
4	3.7 km x 3.7 km (2 n mi x 2 n mi)
E*	9 km x 9 km (4.85 n mi x 4.85 n mi)

*Equivalent IR sector, same geographical area as corresponding visible sector.

g Enhancement curve identifier for IR data only. A single letter, Z, identifies the enhancement curve used on full-disc IR data. On all other IR data, the enhancement curve displayed is identified by two letters (AA-ZZ). Absence of letters indicates no enhancement of data.

h Starting scan line number for the image (Y-axis). Range: 0000-1821.

i Vernier correction factor for starting scan line number.

j The X-axis element number of the midpoint of each horizontal line contained in the sector. Range: 0000-3822.

k Vernier correction factor for sector center location.

Sector Identification

	Standard Sector	Floating Sector	Rapid Scan Sector
GOES HEADER	DB5	DA37N82W-1	PQ35N95W-1
Coding Elements	a b c	a b d e f	g h i j k

Coding Elements

a Major NESS hub (SFSS or regional area requirement) for which the sector is generated.

Identifier	Station
A	Anchorage
D	Washington, D.C.
H	Honolulu
K	Kansas City
M	Miami
S	San Francisco
U	Universal

Identifier	Region
W	Washington complex production only (not transmitted over GOES network).
WB	4 km (2 n mi) geographical sector with 2 km (1 n mi) resolution.
WC	9 km (4.85 n mi) full-disc with 4 km (2 n mi) resolution.

b Sector resolution. (See **f** above.)

c Identifier number for the specific standard sector (1-9).

d Latitude of image center point.

e Longitude of image center point.

f Identifier number for the selected floater (1 or 2).

g Identifier for type of scan:

Identifier	Scan
P	Partial disc
L	Limited scan

h Identifier for cycle time of the rapid scan data.

Identifier	Scan Cycle
(1-9)	Number indicates approximate minutes of scan cycle.
Q	15 min. (standard scan cycle).

i Latitude of image center point.

j Longitude of image center point.

k Identifier number for the selected floater (1 or 2).

This information was taken from the following publication:
Corbell, R.P., et al., 1976: The GOES/SMS User's Guide. National Environmental Satellite Service, NOAA, Washington, D.C.

1230 :

1B-18a. GOES-I

Figs. 1B-18a and 1B-19a are examples of visible and enhanced infrared imagery transmitted on the GOES-TAP distribution system over the Eastern U.S. The infrared image has been enhanced according to the MB curve. This curve is designed to highlight thunderstorm cloud top temperatures and thus helps isolate the areas of most intense convective activity.

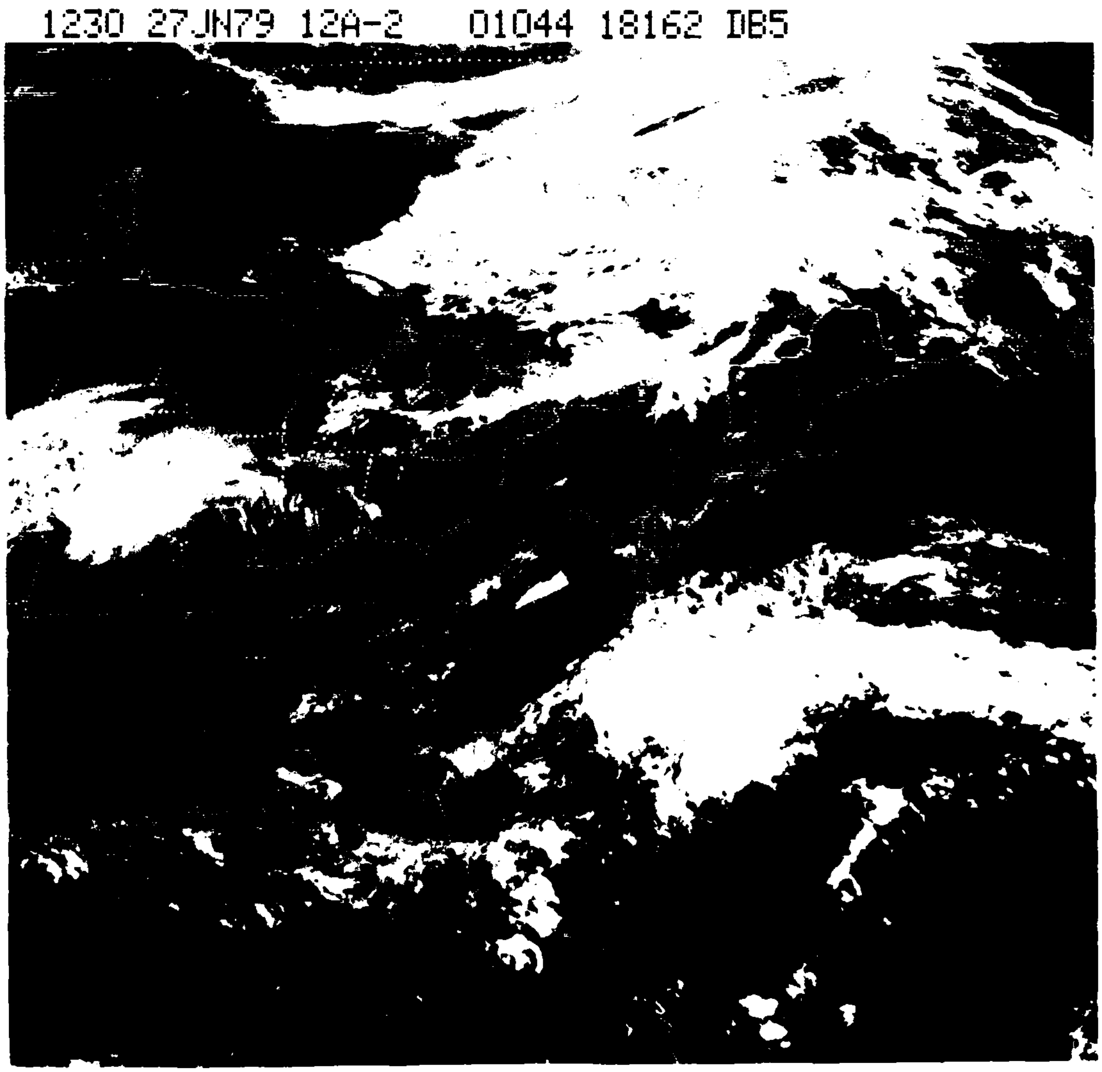

1B-18a. GOES-E. Visible Picture. 1 n mi Resolution. 1230 GMT 27 June 1979.

Infrared Temperature Gray Scale

+50 +40 +30 +20 +10 0°C 10 20 30 40 50 60 70 80 90 100

Temperature values are marked at ten degree intervals, from +50° C to −100° C, along the bottom of the gray scale. The gray shades are a photographic display of the enhancement curve used for the picture. Uniform changes in the gray shades from black to white in the lower end of the scale, in this example, correspond to linear temperature changes. Abrupt changes in the gray shades at the upper end of the scale, in this example, designate temperature steps in the enhancement curve to obtain "contouring" of the temperature features in the picture, as shown in the figure below.

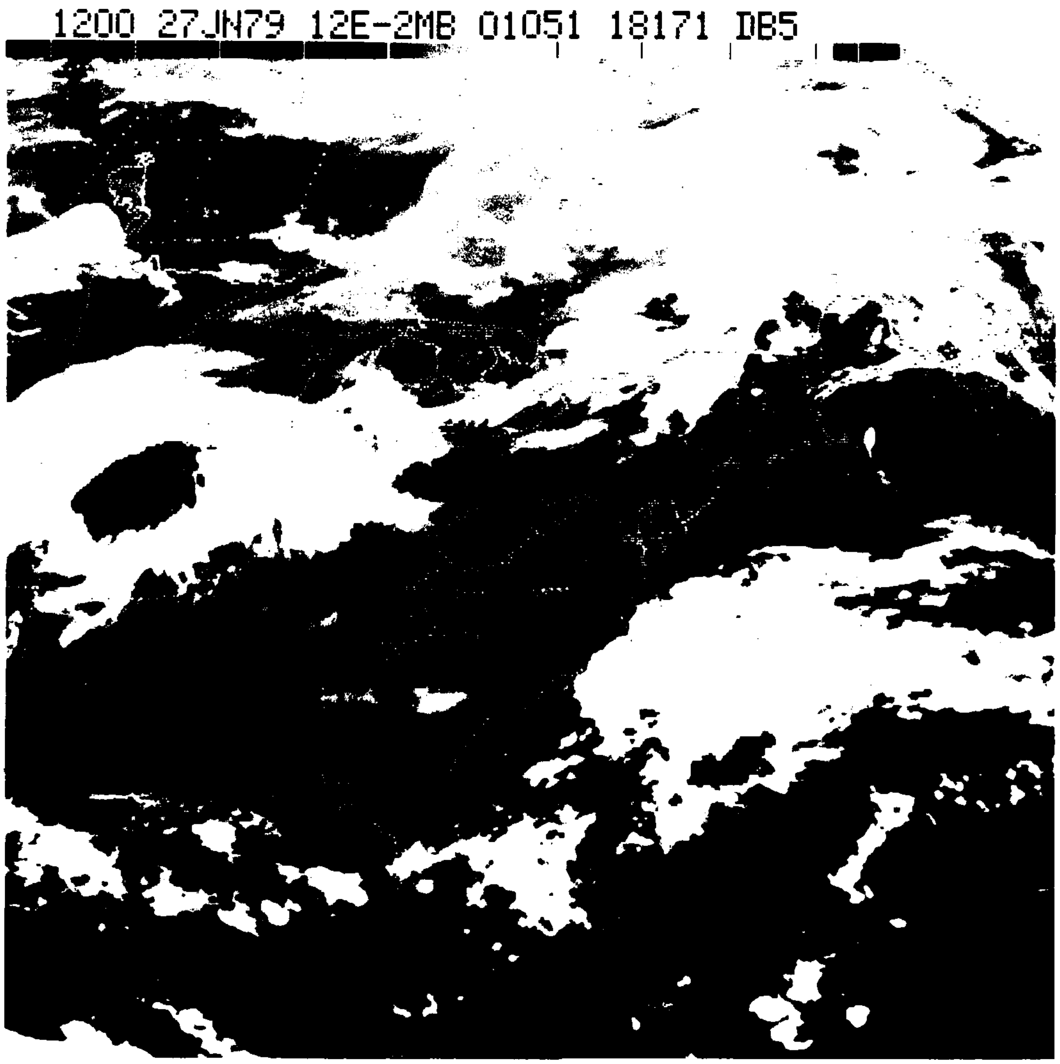

1B-19a. GOES-E. Infrared Picture (Enhancement Curve MB), 5 n mi Resolution 1200 GMT 27 June 1979.

Geostationary Meteorological Satellite
(GMS)

Japan currently operates one geostationary satellite, GMS, which has a satellite subpoint at 140° E, 0° N. This position gives GMS an areal coverage from Antarctica to Siberia, and from Hawaii to India.

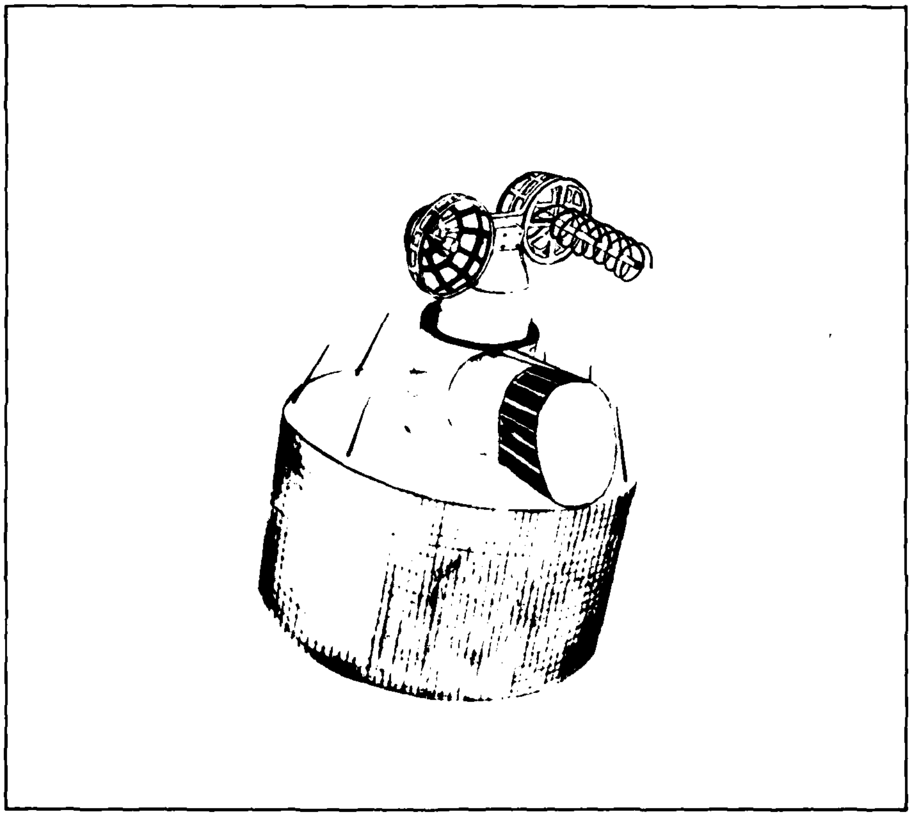

1B-21a. On the GMS spacecraft, the S-band and UHF antennas and the radiometer aperture protrude from the main cylindrical body. As with the GOES spacecraft, the outside of GMS is covered with solar power cells.

Image Acquisition and Distribution

The frequency of picture taking by the GMS satellite and the method of picture distribution to the user are different from those of the GOES satellite due to differences in satellite design, design of the ground processing system, and other factors. Since distribution of satellite image data by landline facsimile is very difficult in the western Pacific and eastern Asia, image data are distributed through the GMS spacecraft on a time-delayed basis (i.e., facsimile pictures are not transmitted until after the complete full disc image is acquired).

The GMS image distribution system (Fig. 1B-22a) begins with the acquisition of raw VISSR data from the spacecraft by the Command and Data Acquisition Station (CDAS) located at Hatoyama (about 34 mi northwest of Tokyo). In the CDAS, the raw VISSR data are fed into a synchronizer/data buffer which stretches the data rate to the length of one spin period of the spacecraft. Picture parameter data and a gray scale are added to the stretched data, and the data are sent to the Data Processing Center (DPC) at Kiyose (about 15 mi northwest of Tokyo) by microwave.

As the stretched VISSR data arrive at the DPC, they are taken into an on-line computer through a high speed communications system and the data are stored on a magnetic disc together with the picture parameter data. The data are then processed to produce a full disc, high resolution analog facsimile (HR-FAX) picture. The HR-FAX visible picture has a resolution of 1.4 n mi at the satellite subpoint, while the infrared picture has a 2.7 n mi resolution. The picture also includes grid lines, gray scale wedge, and annotations (specifying observation time, sensor type, etc.). For transmission, the HR-FAX picture data are sent back to the CDAS via microwave link and then transmitted through the GMS spacecraft on to Medium-scale Data Utilization Stations (MDUS). Transmission of one HR-FAX picture takes approximately 14 minutes and transmissions are scheduled for eight 28 minute time slots per day. Since raw VISSR data transmission and facsimile transmissions operate on the same frequency, they are time-shared in the routine operation of GMS. In addition to the full disc picture, a Mercator projection picture (schematically shown in Fig. 1B-23a) is also produced and transmitted on HR-FAX four times a day.

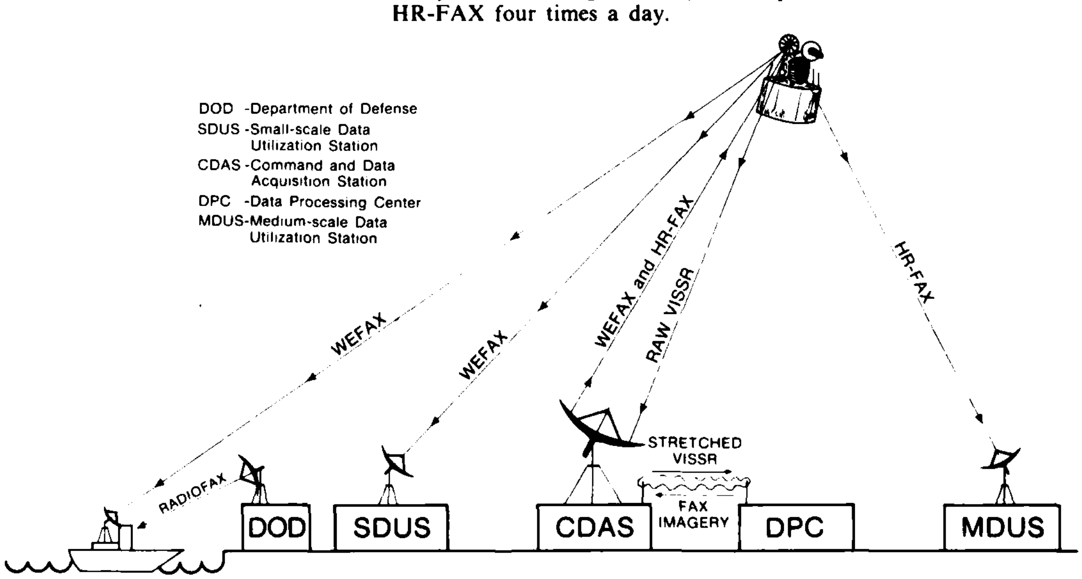

1B-22a. GMS Central Data Distribution System.

Next, the on-line computer prepares the low resolution facsimile (WEFAX) pictures for transmission to Small-scale Data Utilization Stations (SDUS). This time the full disc picture of the Earth is sectorized into seven portions (as shown in Fig. 1B-23b) and each portion is stored on a separate magnetic disc. Each disc contains all necessary information to construct one WEFAX image and takes approximately four minutes to transmit. All 7 sectors are transmitted in a 28 minute time slot eight times a day. The resolution of the WEFAX images at the satellite subpoint is 2.5 n mi for the visible imagery and 4 n mi for the infrared imagery.

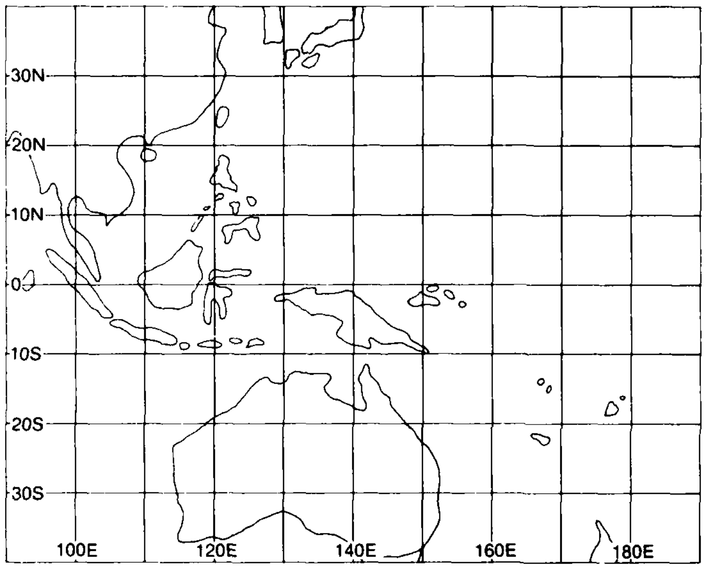

1B-23a. GMS Mercator Projection Picture.

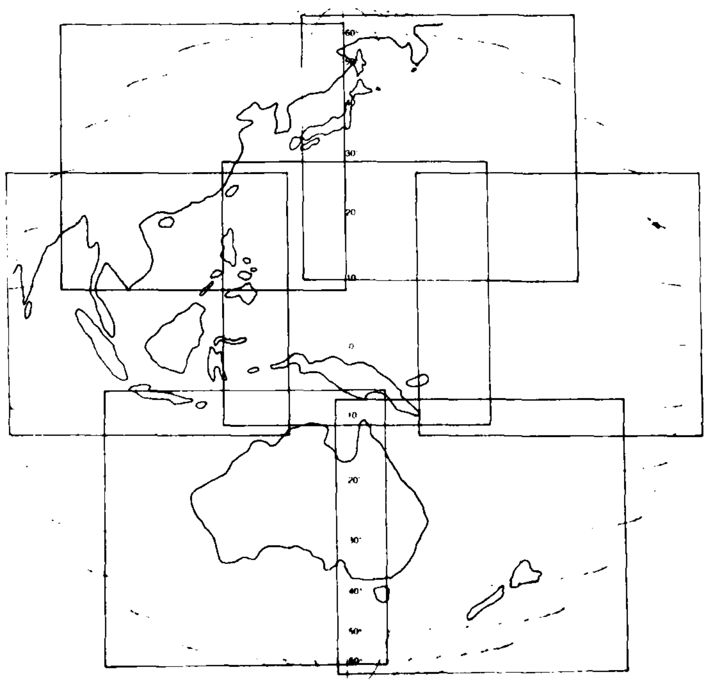

1B-23b. GMS WEFAX Sectors.

Because the Japanese government has not granted blanket approval for reception of direct broadcast HR-FAX and WEFAX signals from GMS, approval is granted on a case-by-case basis by the Planning Director, Japan Meteorological Agency.

Sensor System Description

At the GMS spacecraft, radiation from the Earth scene enters a telescope aperture and is reflected 45° by an object-space scan mirror. Radiation reflected from the scan mirror enters a Cassegrain telescope (primary and secondary mirrors) which focusses the radiant energy onto the detector array.

Energy in the visible spectrum is detected by using eight fiber optics located at the focal plane. The other ends of the fibers are incident upon eight PMT's (four active, four backup) responding in the 0.55–0.75 μm range. Each PMT has an IFOV of 0.031 by 0.035 milliradians which gives a spatial resolution of approximately 0.7 n mi at the satellite subpoint. As with GOES, the output voltage from each PMT is converted to one of 64 digital counts for transmission to the ground.

Infrared spectrum energy (10.5–12.5 μm) is also relayed and filtered from the detector array to two detectors (one active, one backup) cooled to a controlled temperature of 93.5° K. Each infrared sensor has an IFOV of 0.14 by 0.14 milliradians which gives a spatial resolution of 2.7 n mi at the satellite subpoint.

The infrared sensor output is normalized in terms of the equivalent blackbody temperature of the radiating object so that the sensor output is a simple, nearly-linear function of scene temperature. The infrared temperature sensitivity is a 0.5° K change when viewing a 300° K object, degrading to a 1.5° K change when viewing a 200° K object. The NETD is approximately 0.3° K across the entire temperature range.

Spectral Characteristics

The responses of the GMS visible and infrared sensors are identical to those of GOES. See the section on GOES Spectral Characteristics for a discussion of the response curves which also pertain to the GMS.

References
Hirai, M., 1978: Current status of Japanese meteorological satellites GMS and GMS-2. WMO/UN Regional Training Seminar on the Interpretation, Analysis, and Use of Meteorological Satellite Data, Tokyo, Japan, SAT/L2A 1 14.
Kodaira, N., 1978: Outline of the GMS system. WMO/UN Regional Training Seminar on the Interpretation, Analysis, and Use of Meteorological Satellite Data, Tokyo, Japan, SAT L1C 1 13.

Sample Imagery, GMS

These simultaneous visible and infrared pictures show cloud patterns and thermal features over the Western Pacific, Eastern Asia, and Australia. Geographical boundaries and a latitude/longitude grid have been added to both pictures. Additionally, registration marks (+) are put on the pictures to facilitate alignment of a series of images.

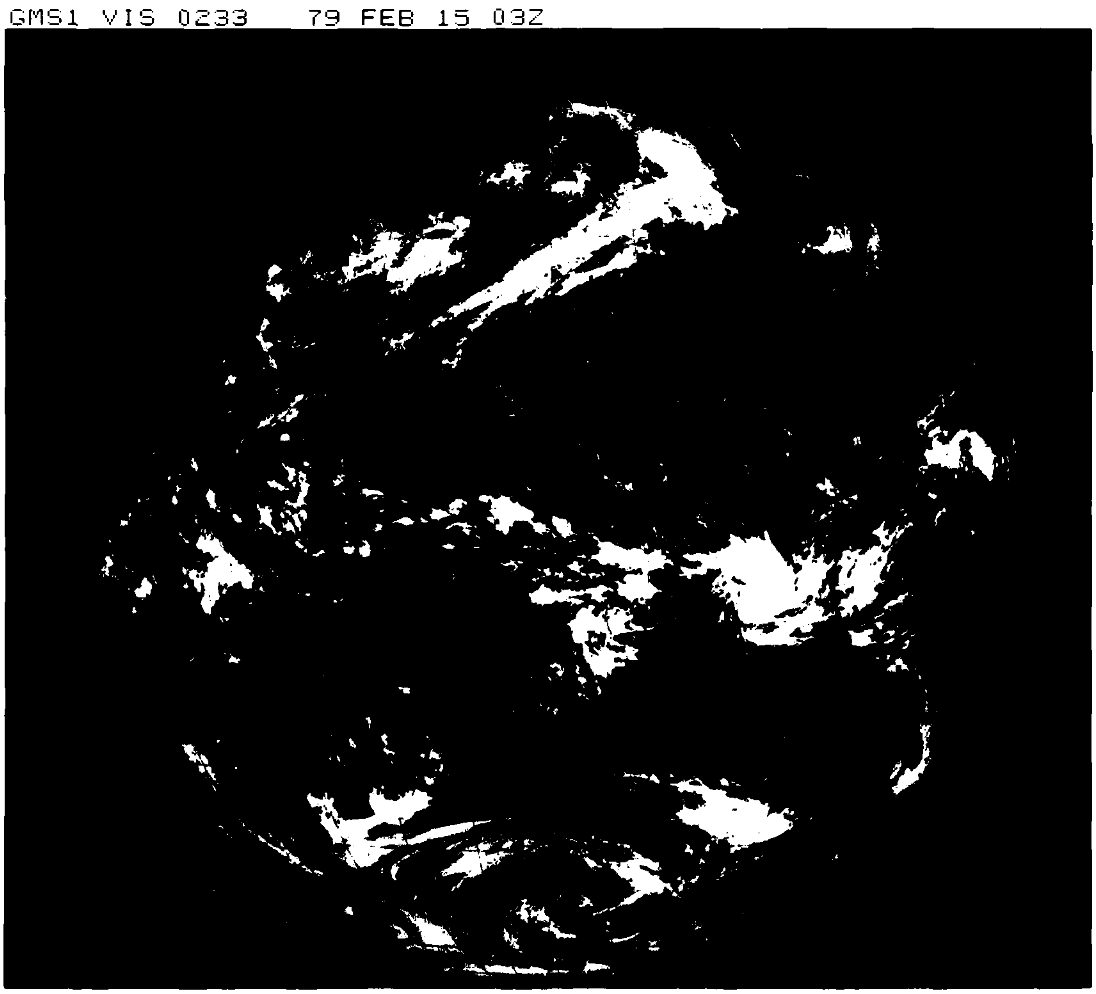

1B-26a. GMS. Visible Picture, 0.7 n mi Resolution. 0300 GMT 15 February 1979. (Photo Courtesy of Japan Weather Association.)

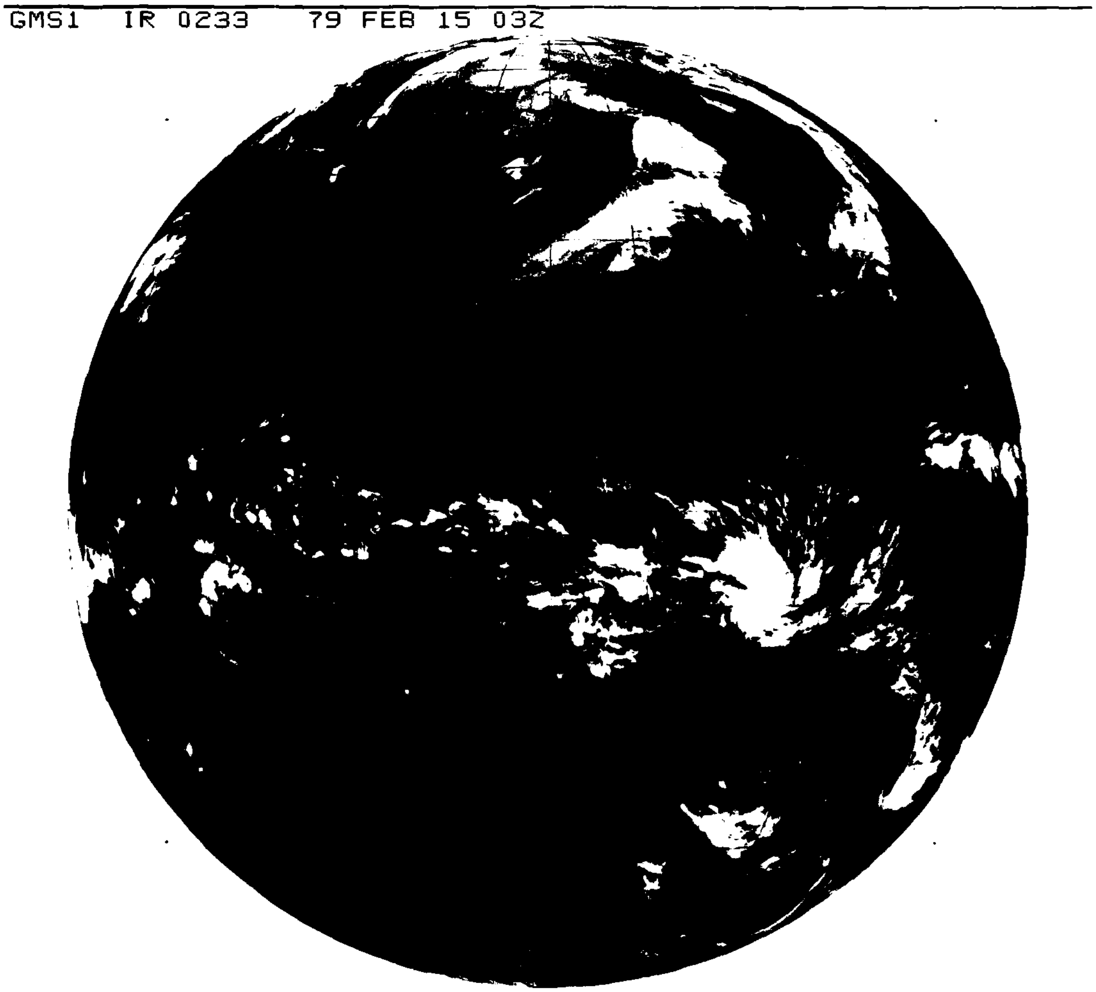

1B-27a. GMS. Infrared Picture, 2.7 n mi Resolution. 0300 GMT 15 February 1979. (Photo Courtesy of Japan Weather Association.)

European Geostationary Meteorological Satellite

(METEOSAT)

The European Space Agency (member-states Belgium, Denmark, France, Italy, Sweden, Switzerland, the United Kingdom, and W. Germany) currently operates one geostationary satellite, METEOSAT[1], which has a subpoint at 0° E, 0° N. This position gives METEOSAT an areal coverage from Antarctica to Greenland and from Saudi Arabia to Brazil.

1. METEOSAT failed in November, 1979. Current plans are for the launch of a similarly equipped METEOSAT-2 in 1980.

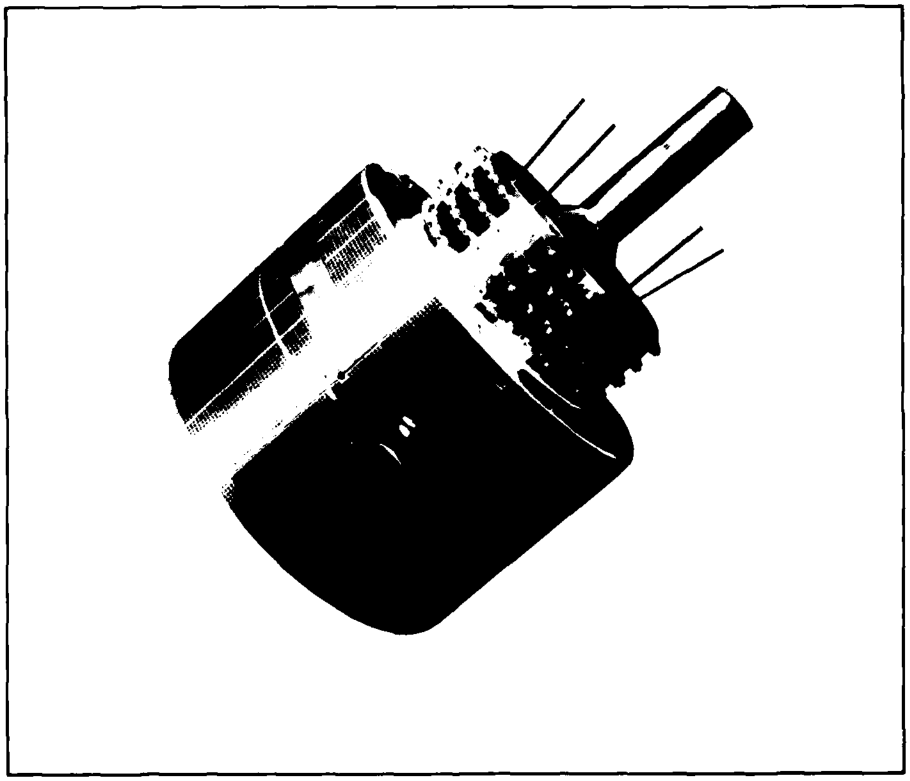

1B-29a. METEOSAT is composed of a main cylindrical body, 82 inches in diameter, on top of which a drum-shaped section and two cylinders are stacked concentrically. The main cylinder contains the radiometer aperture and arrays of solar power cells, while the drum-shaped section contains elements of the combined S-band and UHF antennas. The thin concentric cylinders on top are additional antennas for S-band and low UHF.

Image Acquisition and Distribution

The METEOSAT image distribution system (Fig. 1B-30a) begins with the acquisition of stretched VISSR image data from the spacecraft by the Data Acquisition, Telemetry, and Tracking Station (DATTS) which is situated in open country some 30 mi southeast of Darmstadt, W. Germany. Stretching of the raw radiometer data is done by an on-board computer unit, although should the unit fail, raw radiometer data can be broadcast directly to the ground. At DATTS, the stretched data are preprocessed and timing data are entered. The data are then relayed by landline to the European Space Operations Center (ESOC) located in Darmstadt.

At ESOC, the stretched image data are processed to remove calibration errors, variations in satellite spin speed, etc., and to mutually register the three channels of data. Because the detectors for the three channels of data are at physically different locations on the focal plane of the telescope, the data values for the same locations in the data chain do not correspond to the same Earth location. The process used to mutually register the three channels of data is called image conditioning. After image conditioning, special computers format the data for digital transmission (HR-FAX) to Primary Data User Stations (PDUS) and analog transmission (WEFAX) to Secondary Data User Stations (SDUS). For broadcast, the facsimile data are relayed back to DATTS and transmitted through the spacecraft on to users.

Both types of facsimile imagery have latitude/longitude grids and coastlines added before transmission. In the case of WEFAX images this information is superimposed on the actual picture, but with HR-FAX images it is added to the transmission as coded data to be used at the discretion of the individual user.

Images from all three spectral channels are included in the distribution schedule, which is designed to cover the entire METEOSAT field of view once every three hours and the European region every half hour. In addition, imagery from the GOES-East satellite is relayed through a station at Lannion, France, and rebroadcast through METEOSAT to users at selected times.

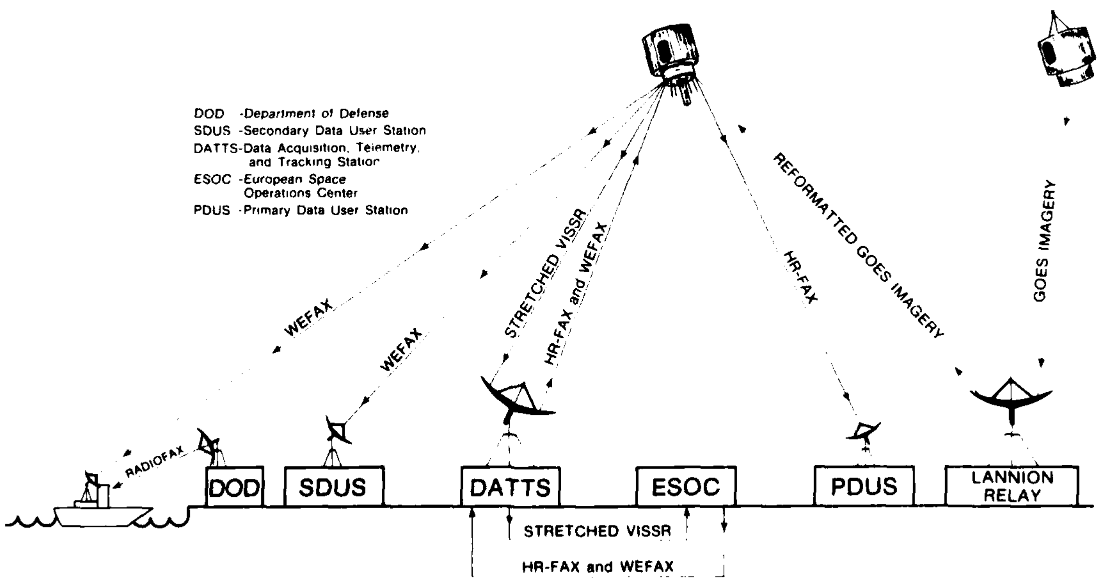

1B-30a. METEOSAT Central Data Distribution System.

Formats used for HR-FAX digital transmissions include format A (Fig. IB-31a) which covers the full Earth disc and is transmitted once every three hours, and format B which is a sector covering the European region and is transmitted every half h. A and B formats include data from all three spectral channels multiplexed on a line by line basis. This allows the user to select the channels as needed or to combine the channels in real-time by employing line buffers in the receiving equipment.

Figs. IB-31a and IB-31b show the areal coverage of formats used for the transmission of WEFAX sectors. The C formats are used for transmission of high resolution visible data. A total of 24 sectors covers most of the full Earth disc. Of the C formats, the European formats C2 and C3 are transmitted at half hourly intervals and the remaining sectors are transmitted at intervals of between one and three hours during daylight.

The D and E formats are used to transmit the infrared and water vapor absorption band imagery. The European infrared sector D2 is transmitted every half hour with full disc coverage in all infrared D sectors at least once every three hours. The nine E sectors used for water vapor absorption band data are transmitted at least twice each day.

Sensor System Description

At the METEOSAT spacecraft, radiation from the Earth scene enters a telescope aperture, is focussed by the primary telescope, and is reflected along the spin axis of the spacecraft to two different focal planes. One focal plane contains two visible sensors while the second focal plane contains three infrared sensors.

In the focal plane of the visible sensors, two silicon diode detectors collect reflected Earth, atmosphere, and cloud radiation in the 0.4–1.1 μm range. Each visible detector has an IFOV of 0.065 by 0.065 milliradians which gives a spatial resolution of 1.6 n mi at the satellite subpoint.

IB-31a. HR-FAX digital transmission formats (A and B) and WEFAX visible imagery formats (C).

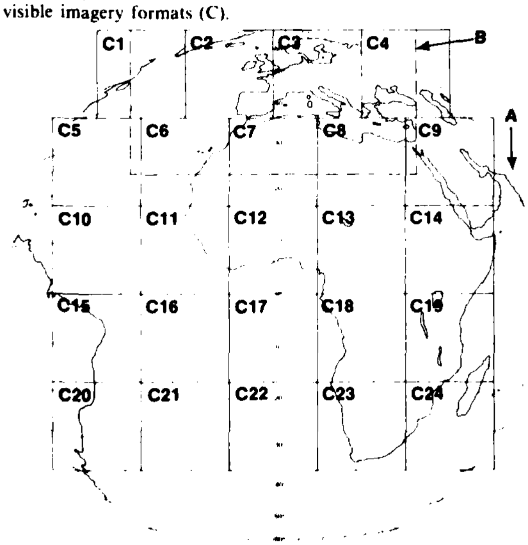

IB-31b. WEFAX infrared formats (D) and water vapor formats (E).

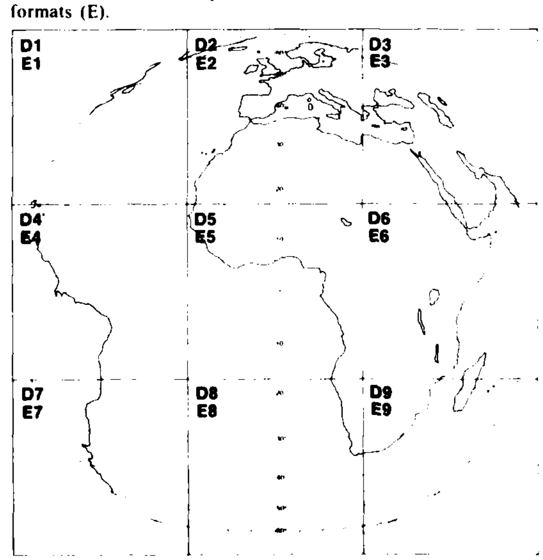

When the water vapor channel is in operation, only one visible detector can be sampled. This reduces the spatial resolution of the visible data to 3.2 n mi in the north-south direction. The resolution in the east-west direction remains 1.6 n mi.

Radiation is also reflected to the infrared sensors which are mounted on a passive cooling plate and cooled to an ambient temperature of 95° K. The infrared detectors include a redundant pair (one active, one backup) for sensing thermal infrared radiation (10.5-12.6 μm) and a single detector for sensing in the atmospheric water vapor absorption band region (5.7-7.1 μm). Each detector has an IFOV 0.14 by 0.14 milliradians and gives a spatial resolution of 3.2 n mi at the satellite subpoint.

The thermal infrared sensor output is normalized in terms of the equivalent blackbody temperature of the radiating object so that the sensor output is a simple, nearly-linear function of scene temperature. The infrared temperature sensitivity is a 0.5° K change when viewing a 300° K scene degrading to a 1.5° K change when viewing a 200° K scene. The NETD is less than a 0.2° K change across the entire temperature range sensed.

Although the water vapor channel is sensitive to temperature, the data obtained from this channel are representative of a fairly deep layer of the atmosphere and thus cannot be assigned to a specific altitude.

The water vapor detector uses the sampling electronics of one of the two visible channels and, consequently, it is sampled 5000 times per line although the ground resolution is only 3.2 n mi. This means that the water vapor detector is oversampled so there is a 50% overlap in the IFOV between adjacent samples in the east-west direction. To display this imagery, the data from the overlapping samples in each direction are averaged with the center sample.

Spectral Characteristics

The METEOSAT spacecraft carries a spin scan radiometer that senses radiation in the visible, water vapor absorption band, and thermal infrared spectrum. The visible sensor's normalized response curve is shown in Fig. 1B-33a. There is little response in the blue end of the visible spectrum in order to minimize the effects of blue light back-scattering of the atmosphere. Since a silicon diode is used as the detector, the peak response is in the near infrared region. The response also extends further into the near infrared than the visible sensors of the other geostationary satellites. This extension into the near infrared makes the sensor more responsive to haze detection and also provides better land/water contrast.

Thermal infrared radiation is collected in the 10.5-12.6 μm atmospheric window region (Fig. 1B-33b). Either one of the two redundant infrared detectors is used for imaging. The IR1 detector curve has a bell-shaped response throughout this spectral interval, while the IR2 curve has a somewhat broader response though this interval. The data obtained form both detectors are essentially the same.

A new feature in geostationary space meteorology is the inclusion of a 5.7-7.1 μm infrared channel that corresponds to the atmospheric water vapor absorption band. This sensor's response curve (Fig. 1B-33c) peaks near 7.0 μm, has a small minimum near 6.5 μm, and has a secondary peak near 6.2 μm. The weighting function curve of the water vapor channel (Fig. 1B-33d) shows that this channel measures the radiant emission of an integrated moisture column from approximately 250 mb

to 500 mb with a peak contribution at 350 mb. In the imagery from this channel, moisture rich or cloudy areas in the upper troposphere are white or light gray shades in the imagery, and the drier areas are dark gray to black tones. This channel, when observing dry atmospheric situations, is not affected by the surface to any appreciable extent and supplies no information on low-level moisture distribution.

For additional information on the METEOSAT system write to:

METEOSAT DATA MANAGEMENT DEPARTMENT
ESOC
Robert-Bosch-Str. 5
D-6100 DARMSTADT
Federal Republic of Germany

References

Houghton, D.D., and V.E. Suomi, 1978: Information content of satellite images. *Bull. Amer. Meteor. Soc.*, **59**, 1614 1617.

Morel, P., M. Desbois, and G. Szejuach, 1978: A new insight into the troposphere with the water vapor channel of METEOSAT. *Bull. Amer. Meteor. Soc.*, **59**, 711 714.

Morgan, J., 1978: Introduction to the METEOSAT system. ESTEC Reproduction Services, Darmstadt, 54 pp.

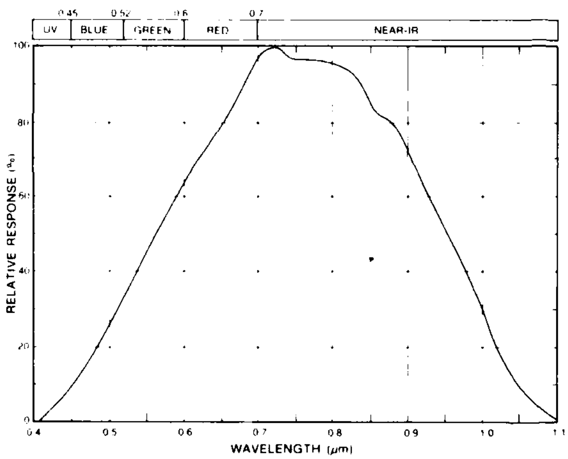

IB-33a. METEOSAT visible channel normalized sensor response curve.

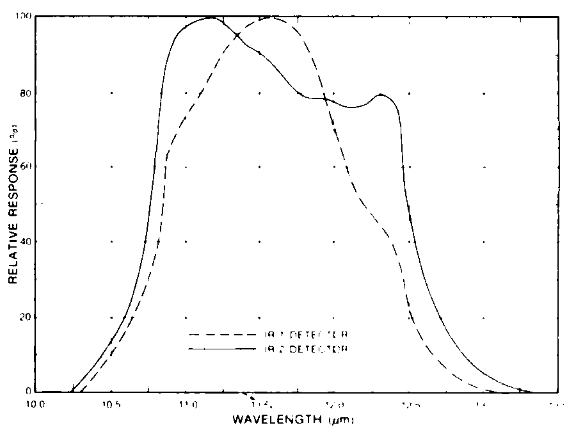

IB-33b. METEOSAT infrared channel normalized sensor response curve.

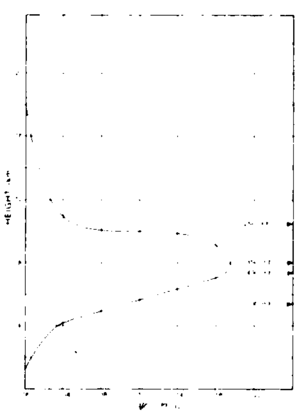

IB-33c. Weighting function curve, based on standard atmosphere assumptions, of the METEOSAT water vapor channel.

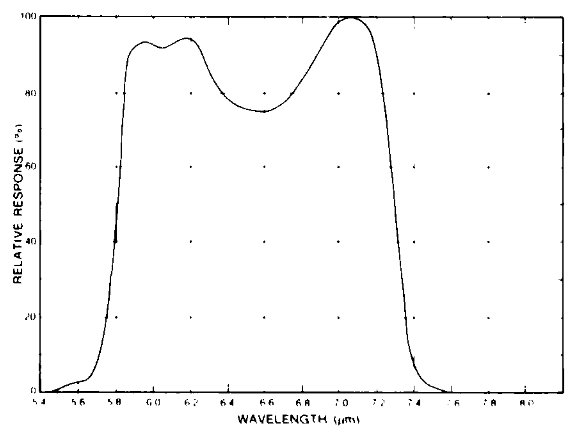

IB-33d. METEOSAT water vapor channel normalized sensor response curve.

Sample Imagery, METEOSAT

Imagery from the METEOSAT spacecraft is available in three spectral intervals: visible (Fig. 1B-34a), thermal infrared (Fig. 1B-35a), and water vapor absorption band (Fig. 1B-35b). The visible and infrared imagery can be interpreted using established analysis techniques. Guidelines for the interpretation of water vapor imagery are in the process of development. It is apparent from Fig. 1B-35b that features appear in the water vapor imagery that cannot be discerned in either the visible or infrared imagery. At the same time some features, such as low-level cloudiness, are not detected at all in the water vapor channel.

In general the data obtained from the water vapor channel are representative of the humidity content of the middle troposphere (600 300 mb). Brighter regions correspond to lower radiative temperatures where radiation comes from higher altitudes, while darker regions correspond to higher temperatures where the radiation comes from lower altitudes.

1B-34a. METEOSAT, Visible Picture, 1.6 n mi Resolution, 1225 GMT 6 May 1978. (© European Space Agency, 1978)

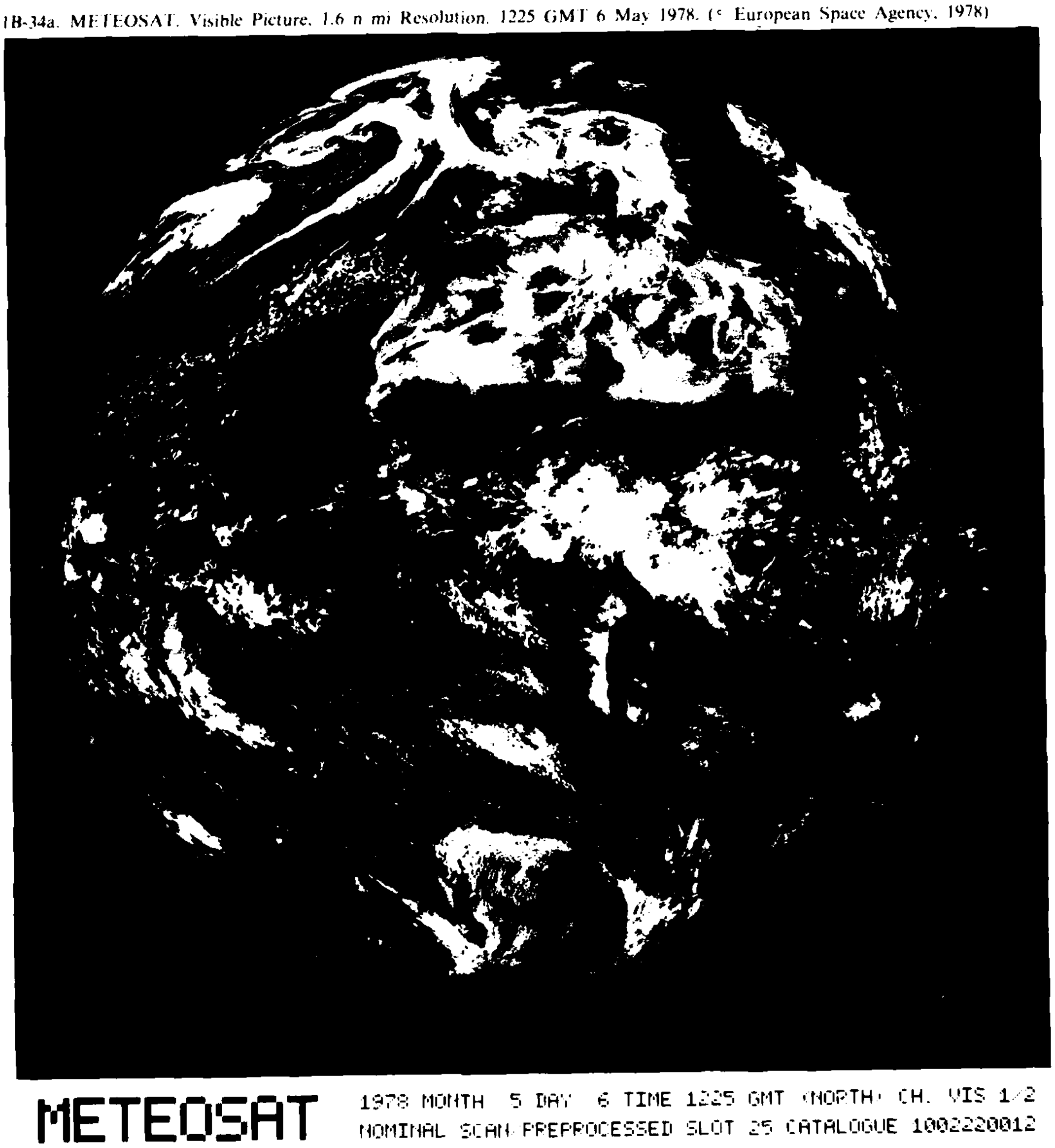

1B-35a. METEOSAT. Infrared Picture. 3.2 n mi Resolution. 1225 GMT 6 May 1978. (© European Space Agency, 1978)

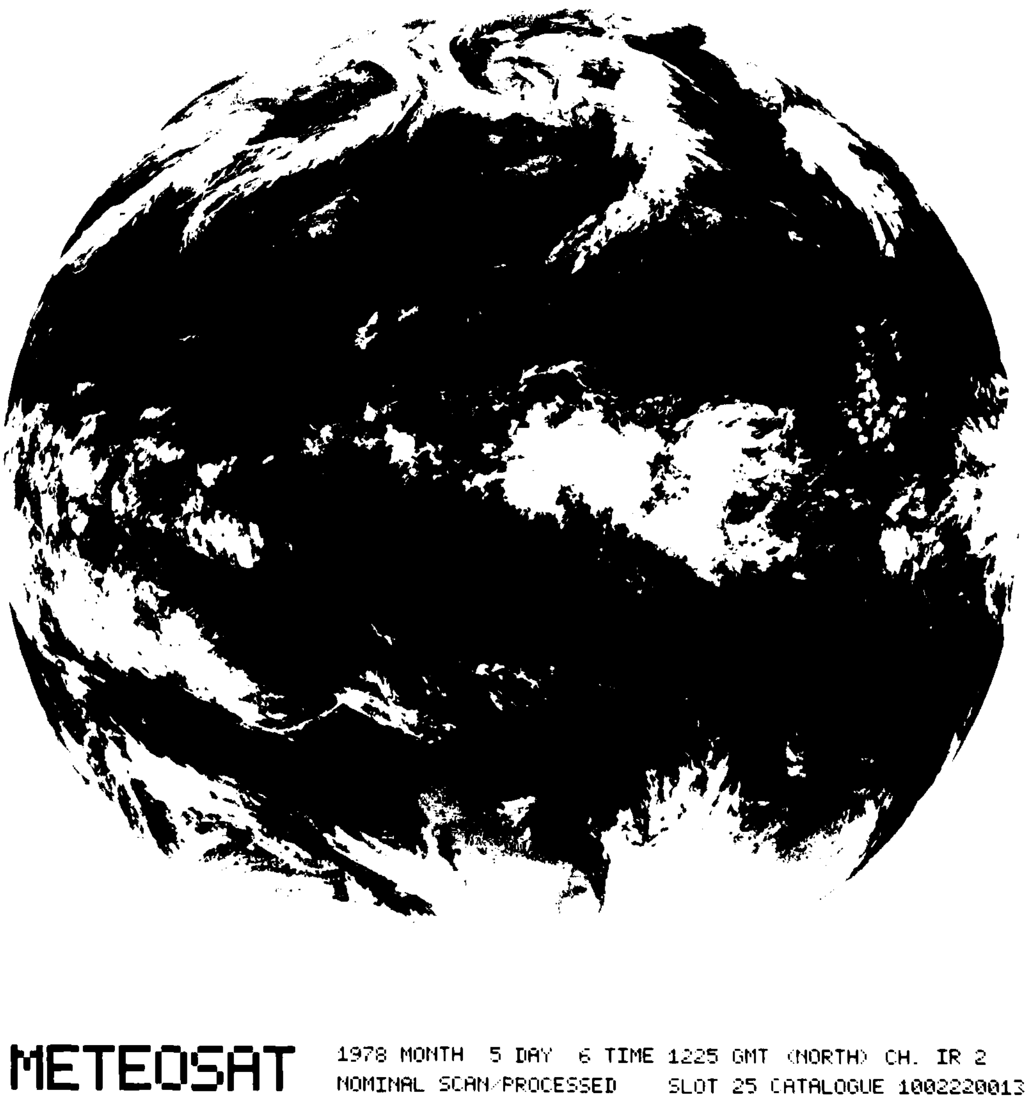

1B-35b. METEOSAT Water Vapor Picture, 3.2 n mi Resolution 1155 GMT 6 May 1978 (© European Space Agency, 1978)

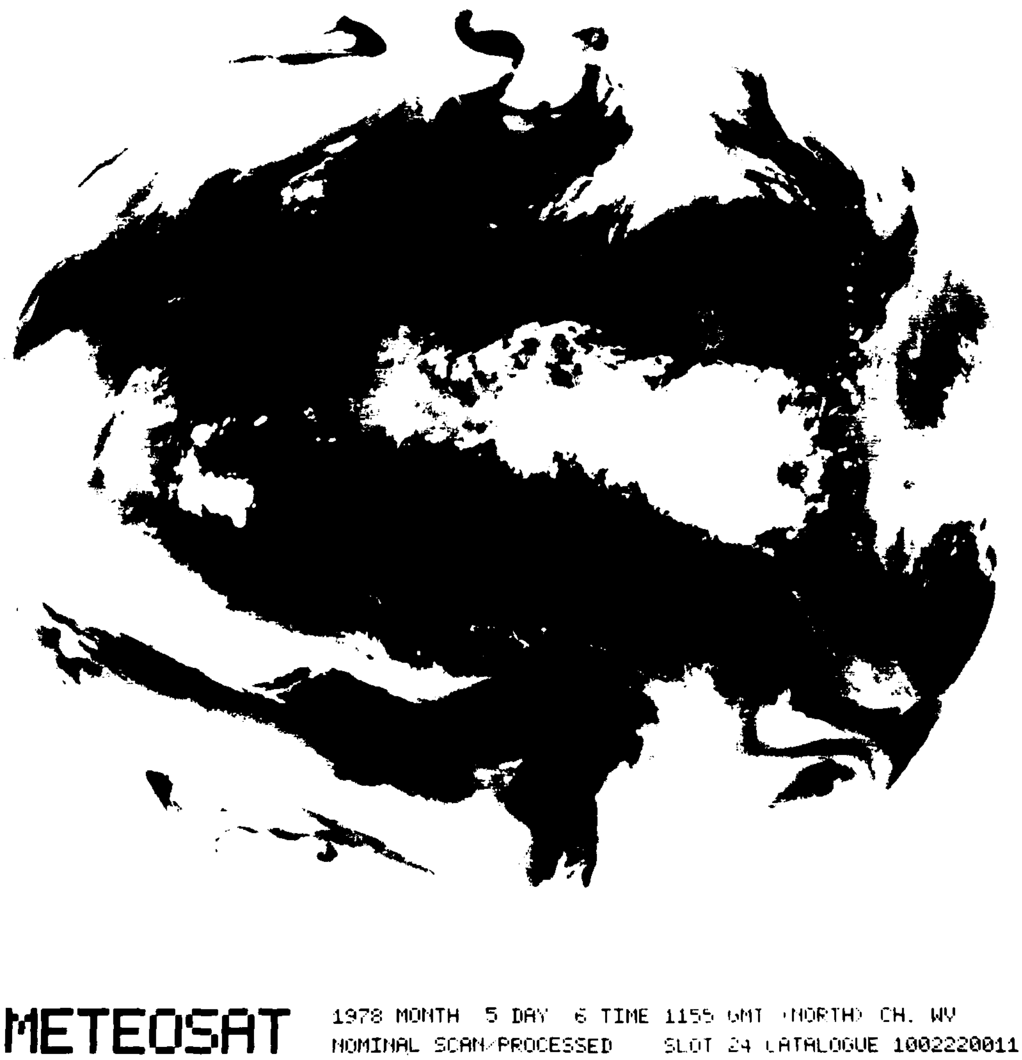

This section is under development and will be forwarded for inclusion in this volume.

Section 3

Cyclogenesis

3A Introduction

3B Case Studies

Cyclogenesis

3A Introduction

Extratropical Cyclogenesis in the North Atlantic and Mediterranean

Cyclogenesis is defined as any development or strengthening of a cyclonic circulation in the atmosphere. It is applied to the intensification of an existing cyclonic disturbance, and to the development of a cyclonic circulation where one did not previously exist. In this section, extratropical cyclones that occur during the cold season, from October through April, will be discussed.

Polar-Front Cyclogenesis

Polar-front cyclones are extratropical disturbances that originate as perturbations on polar fronts. The mean winter location of the North Atlantic polar frontal zone is shown in Fig. 3A-1a. The actual position may vary between the Great Lakes and Iceland in the north and the Gulf of Mexico and Portugal in the south. Note that the patterns of percent frequency of extratropical cyclogenesis show a maximum over the Gulf Stream off the U.S. East Coast and the eastern Mediterranean (Gulf of Genoa). The high frequency of cyclogenesis off the U.S. East Coast is due to the strong land/water thermal contrasts; in the Gulf of Genoa, which has the highest frequency of cyclogenesis in the North Atlantic Mediterranean area, the cyclogenesis is due to a combination of thermal and orographic effects.

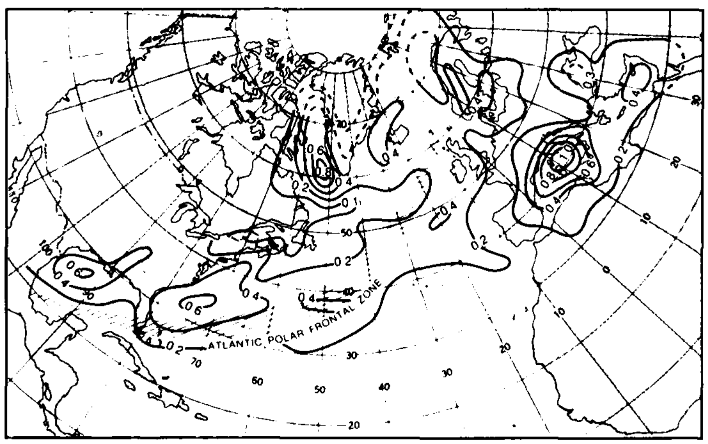

3A-1a. Mean position of the Atlantic and Mediterranean Polar Frontal Zone and frequency of cyclogenesis. (After Petterssen, 1956.)

Junker and Haller (1980) show that there are certain recurring cloud patterns in intense winter season cyclones that form in strong baroclinic zones over the oceans. They also show that the central pressure can be estimated from the appearance of these cloud patterns in satellite pictures. On the following pages, GOES-East infrared pictures illustrate the characteristic cloud patterns of intense cyclones over the North Atlantic, and the corresponding lowest observed surface pressures in these systems.

References

Junker, N.W., and D.J. Haller, 1980: Estimation of surface pressure from satellite cloud patterns. *Mar. Wea. Log.*, **24**, 83 87.

Petterssen, S., 1956: *Weather Analysis and Forecasting*, Vol. 1. McGraw-Hill Book Co., New York, 428 pp.

Surface Pressure Estimates from Cloud Patterns of Developing Intense Extratropical Cyclones

The most intense cyclones are formed in strong baroclinic zones identified by a broad band of multi-layered clouds in satellite imagery. The earliest indication of cyclogenesis can be seen as a thickening and bulging of a segment of the frontal cloud band toward the cold air (Fig. 3A-3a). At this stage of development, the central pressure of the incipient cyclone is usually more than 1000 mb. As the system continues to develop, the cloud pattern takes on a wave-like appearance (Fig. 3A-3b). The first evidence of a V-shaped dry slot on the rear edge of the wave indicates that the pressure is in the mid 990–1000 mb range. This intrusion of dry air into the system is a characteristic feature of rapidly developing cyclones. In Fig. 3A-3c, the distinct curved cloud band indicates that the cyclonic circulation is well-developed, and the central pressure is now below 990 mb. Since the curved cloud band extends from $\frac{1}{2}$ to $\frac{3}{4}$ of the distance around the cyclonic circulation center, the pressure is near 980 mb.

These cloud feature changes indicate the development of a deep surface low with an intense cyclonic vortex extending to high levels. Figure 3A-3d shows the clouds taking on a definite spiral pattern, reflecting the intense cyclonic circulation, and making a complete spiral into the center of the vortex. At this time the surface pressure is in the mid 970–980 mb range. Six hours later (Fig. 3A-3e) the clouds have circled the center of the vortex $1\frac{1}{2}$ times, and the pressure is in the mid 960–970 mb range. The more circular the cloud pattern, the lower the central pressure. An elongated spiral cloud pattern indicates a less intense or filling system. During the mature stage (Fig. 3A-3f), the spiral bands have become fragmented, with cloud-free areas appearing between the bands; and the surface pressure can no longer be accurately estimated from the cloud pattern.

These examples show that a useful relationship exists between the cloud patterns and the lowest observed surface pressure in intense extratropical cyclones. Note that the identifiable cloud pattern changes correspond to intervals of 10 mb in surface pressure. Thus, in practice, when the cloud pattern of a developing cyclone falls into one of the categories of development, the actual surface pressure estimate selected can be from the upper values of the range if the cloud pattern features are stronger, the mid-values of the range for typical situations, and from the lower values of the range if the cloud features are weaker than specified by the category. If the initial stage of cyclone development is observed in an area where the surrounding pressure is already less than 1000 mb, later stages will also generally show lower surface pressures. Estimates of the surface pressure should be correspondingly adjusted downward in each of the basic categories to reflect the more intense cyclonic disturbances.

1000 mb or more
The low center is not well defined by the cloud pattern. The multi-layered cloud band shows a slight brightening and anticyclonic bending.

Central pressure: 1011 mb

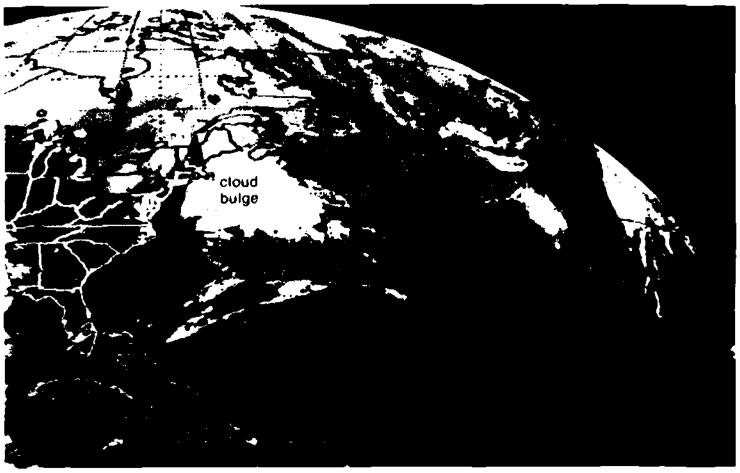

3A-3a. GOES-E. Infrared Picture, 5 n mi Resolution. 0000 GMT 22 November 1980.

990–999 mb
A dry slot of clear air forms on the rear edge of the cloud pattern. The system should be watched closely for possible rapid deepening.

Central pressure: 996 mb

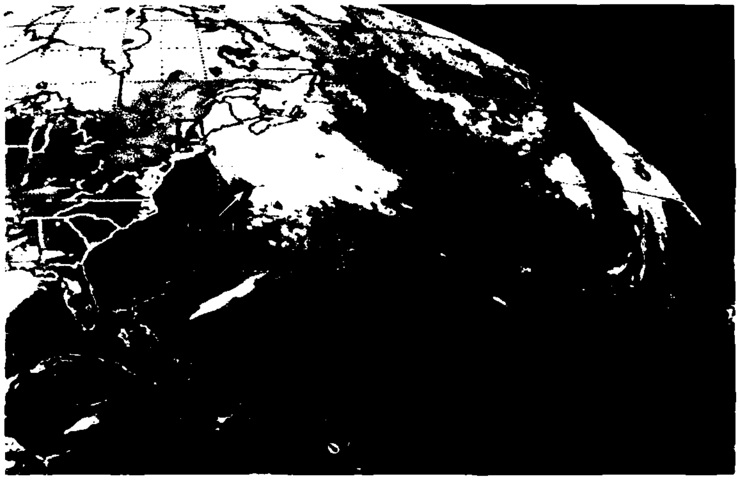

3A-3b. GOES-E. Infrared Picture, 5 n mi Resolution. 0600 GMT 22 November 1980.

980–989 mb
The cloud band develops a distinct hook to the north and west of the surface low. By 980 mb the cloud band wraps around the low ½ to ¾ times.

Central pressure: 981 mb

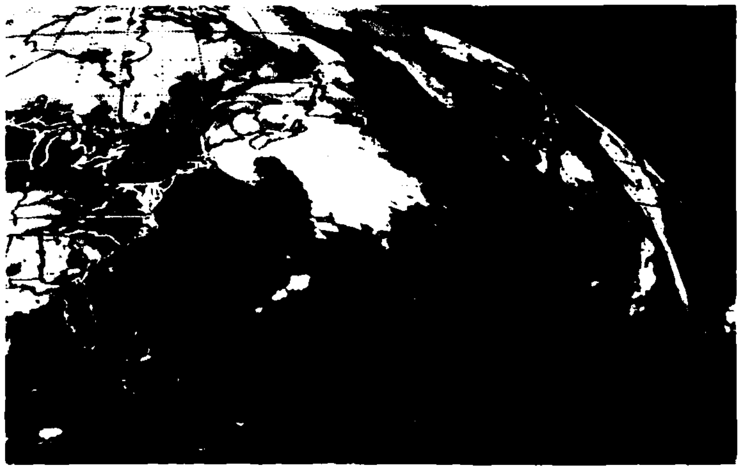

3A-3c. GOES-E. Infrared Picture, 5 n mi Resolution. 1200 GMT 22 November 1980.

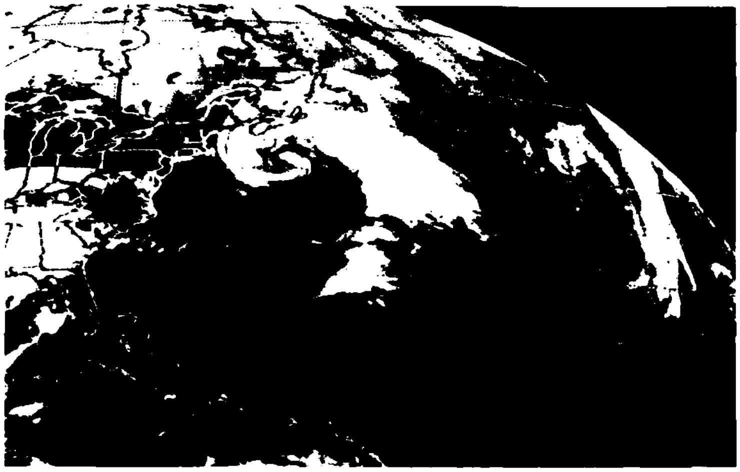

3A-3d. GOES-E. Infrared Picture. 5 n mi Resolution. 1800 GMT 22 November 1980.

970–979 mb
The cloud band wraps around the low center almost one full time.

Central pressure: 974 mb

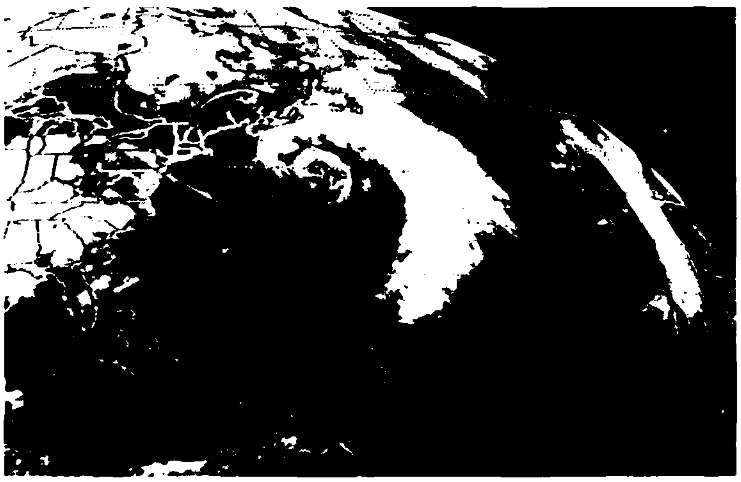

3A-3e. GOES-E. Infrared Picture. 5 n mi Resolution. 0000 GMT 23 November 1980.

Below 969 mb
The cloud band wraps around the low center $1\frac{1}{2}$ times with low and middle clouds sometimes filling in between the encircling cloud band. The circulation center is concentrically located within the spiral formed by the clouds.

Central pressure: 966 mb

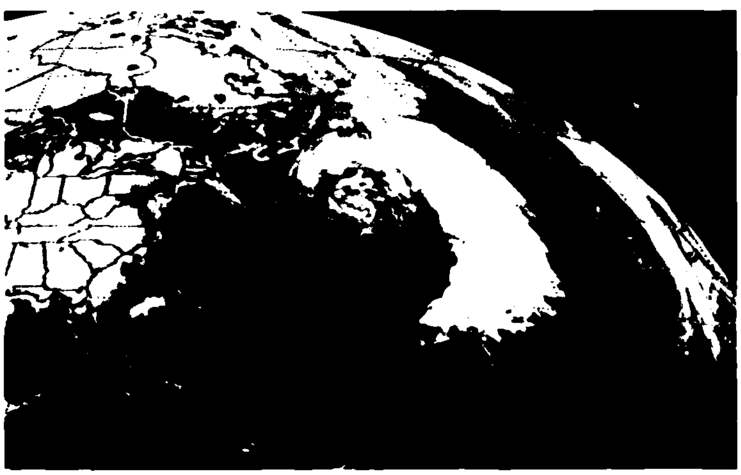

3A-3f. GOES-E. Infrared Picture. 5 n mi Resolution. 0600 GMT 23 November 1980.

Mature stage
The spiral bands have become fragmented, with cloud-free areas appearing between the bands; and the surface pressure can no longer be accurately estimated from the cloud pattern.

Explosive Cyclogenesis

Explosive cyclogenesis is a rapidly deepening extratropical low in which the central pressure at sea level falls at the rate of at least one mb/hr for 24 hr. These storms are a predominately maritime, cold season weather event, and it has been found that explosive deepening is a characteristic of the vast majority of the deepest cyclones (Sanders and Gyakum, 1980).

Explosive cyclogenesis occurs frequently in the western North Atlantic (Fig. 3A-4a). Although these storms occur over a wide range of sea surface temperatures, they have a strong preference for development near regions of strong sea surface temperature gradients. (Note the position of the Gulf Stream.)

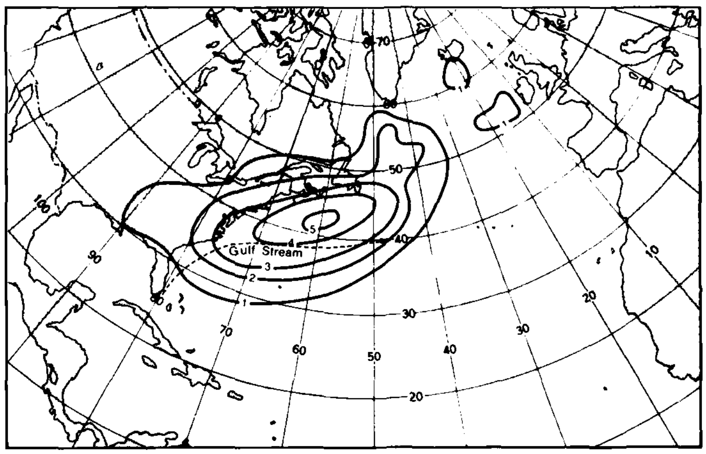

3A-4a. Frequency of explosive cyclogenesis in the North Atlantic. (After Sanders and Gyakum, 1980.)

Satellite pictures can be used to identify explosive developing storms. A DMSP visible picture (Fig. 3A-5a) shows the characteristic cloud pattern of an explosively developing cyclone in the North Atlantic. The cloud pattern consists of a compact cirrus canopy, resembling a cloud head configuration, over the center of the disturbance, and a large field of open cellular cumulus surrounding the system on the cold air side.

Reference

Sanders, F., and J.R. Gyakum, 1980: Synoptic-dynamic climatology of the "bomb". *Mon. Wea. Rev.*, **108**, 1589 1606.

3A-5a. F-1. DMSP LF Low Enhancement. 1249 GMT 22 December 1978.

Cyclogenesis in Polar Air Streams

In winter over the oceans, cyclones are observed to form in polar air streams behind or poleward of major frontal systems and in the western and southern peripheries of large polar low pressure areas (Reed, 1979). These cyclones do not originate, in the classical sense, as wave perturbations on polar fronts separating tropical and polar air masses. They are upper-level phenomenon and are found in regions of deep baroclinity and vorticity maxima. Because of their small size, satellite imagery can be used in locating and tracking these cyclones, particularly in regions of sparse data.

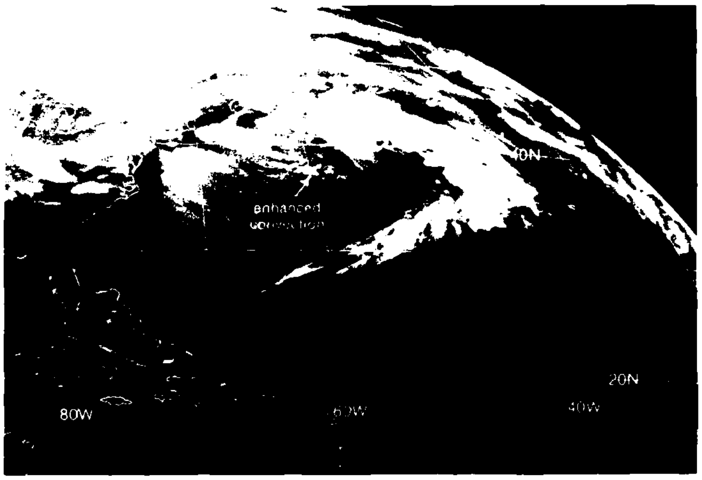

3A-6a. GOES-E. Infrared Picture, 5 n mi Resolution. 1730 GMT 10 February 1979.

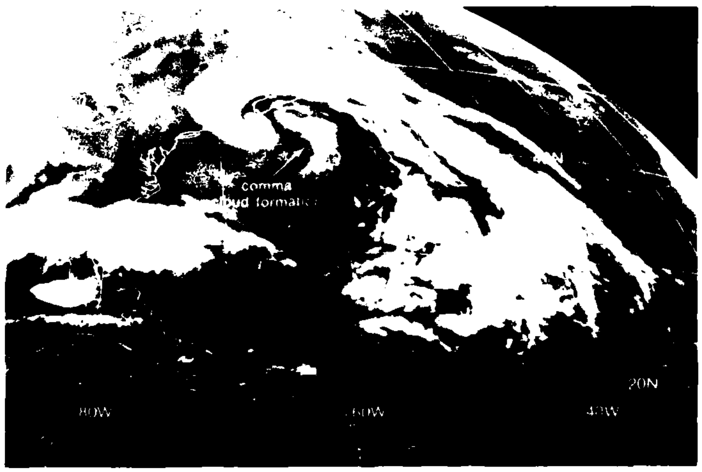

3A-6b. GOES-E. Infrared Picture, 5 n mi Resolution. 1500 GMT 27 January 1979.

Typically, cyclogenesis in polar air streams is preceded by the development of a region of enhanced convection (Fig. 3A-6a). In the mature stage, the convection becomes larger and deeper, and the cirrus clouds from the deep convection merge and spread out into a comma-shaped cloud formation (Fig. 3A-6b). The poorly organized regions of

Reference

Reed, R.J., 1979: Cyclogenesis in polar air streams. *Mon. Wea. Rev.*, **107**, 38-52.

enhanced convection may circulate around the periphery of the major low in which they are embedded and not develop any further. However, it is a common occurrence for the mature comma-shaped cloud pattern disturbances to give rise to wave perturbations on the main frontal band if they approach sufficiently close to the front.

In satellite imagery, these cyclones are characterized in their mature stage by a comma-shaped cloud pattern (typically 500–1000 km in length). The U.S. National Weather Service depicts these cyclones by a dashed line on surface charts, labeled TROF, since in the initial stages they do not develop closed isobars at the surface. A TROF is defined as a line of maximum cyclonic curvature in the surface isobars not having the thermal characteristics of a front. In the more vigorous cases, frontal characteristics may be acquired and a surface low formed; the trough symbol is replaced by that of a cold or occluded front—sometimes called an "instant occlusion" because the cyclone development does not follow the normal wave cyclone occlusion process.

Orographic Cyclogenesis

Mountains influence atmospheric motion by deflecting the airflow horizontally and vertically. On the largest scale, mountains can perturb the large-scale flow and the waves produced can penetrate into the stratosphere. On the synoptic scale, the flow across and around mountains can alter the temperature and vorticity fields so as to facilitate baroclinic growth and cyclogenesis. In the large-scale flow pattern the lee side of mountains are the strongly cyclogenetic areas. The Gulf of Genoa, to the south of the Alps, is statistically one of the most cyclogenetic regions of the North Atlantic Mediterranean area and in the world (Fig. 3A-7a). The onset of Gulf of Genoa cyclogenesis is rapid and can be attended by severe weather and violent and often devastating surface winds (mistral).

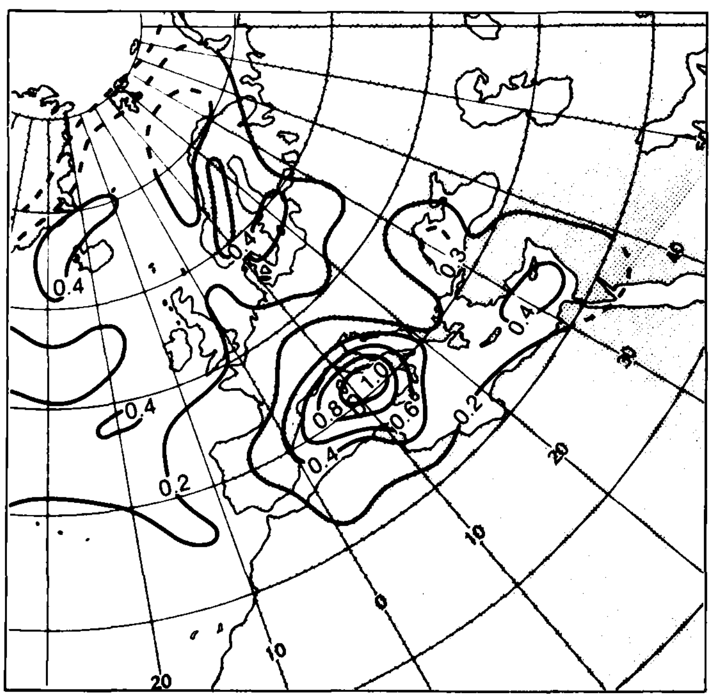

3A-7a. Frequency of cyclogenesis in the Mediterranean Region. (After Petterssen, 1956.)

An example of a Gulf of Genoa cyclone is shown in Fig. 3A-8a. At the time of this DMSP picture there is a surface low (central pressure about 1004 mb, not shown) in the gulf. The area is covered with convective clouds; however, there is no well organized circulation pattern in the cloudiness due to the weak surface pressure pattern.

These depressions are generally of smaller scale in comparison to those of higher latitudes and their development is characteristically more rapid. The formation of Gulf of Genoa lows are a consequence of thermal blocking by the Alps, airflow around and over the mountains (lee vorticity sources), and baroclinic instability in the flow in the middle and upper troposphere.

3A-8a. FTV-33. DMSP WHR Normal Enhancement. 1943 GMT 30 November 1975.

Cutoff Lows and Upper-Cold Lows

When the usual polar trough and ridge flow pattern in mid-latitudes grows in amplitude, cold air is able to flow to low latitudes in the troughs. Frequently one of these large amplitude troughs will develop a closed wind circulation at its southern end, which extends vertically through the troposphere. This results in a mass of polar air cut off from its source region to the north. At the surface, fronts at the leading edge of the cold air are diffuse and difficult to define. The upper-level closed circulation formed by this cutting-off process is called a cutoff low. They are most intense during the winter season; however, they form at all times of the year. Favored regions are in the western Atlantic, off the U.S. southeast coast, between Portugal and the Azores, and over the central Mediterranean Sea.

Cutoff lows are also called upper-cold lows because of their cold-core structure, particularly when they have persisted for some time and have come under the influence of environmental flow patterns different from those in which they formed. They may move to the east, or to the west, depending on the structure of the low in which they are embedded.

The cloud patterns observed in upper-cold lows depends on the depth of the closed circulation and the stability of the environment. Upper-cold lows that develop over stable areas appear different in satellite imagery than upper-cold lows that develop over unstable areas. Over stable areas, the circulation of upper-cold lows is only weakly reflected at lower levels, if at all. Upper-cold lows that develop over unstable areas will strongly influence the low-level circulation.

When a weak upper-cold low is located over a stable low-level environment, such as in the eastern quadrant of a subtropical anticyclone (Fig. 3A-9a), generally the presence of the low can be identified by cirrus clouds in a spiral pattern. Some limited upper-level convection may also be present in the form of bright cumuliform cloudiness. Similarly, a cold low aloft that has a deep closed circulation and is located over an unstable area can be readily identified by an extensive region of enhanced convection (Fig. 3A-9b). Note that the wide-spread convective clouds are organized in a spiral vortex that reflects the presence of the low aloft. A large band of convection appears in the eastern quadrant—this is typical of upper-cold low circulation systems under these conditions. These systems are not rapid developers; however, they can produce heavy rains, strong, gusty winds, and can persist for several days.

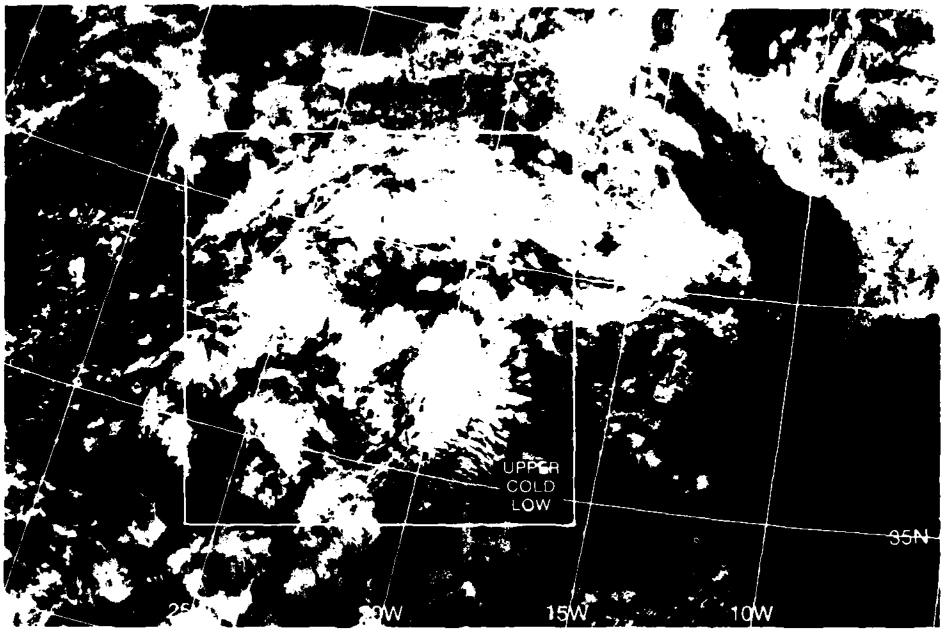

3A-9a. F-2. DMSP TF I-Normal Enhancement. 0826 GMT 18 May 1978.

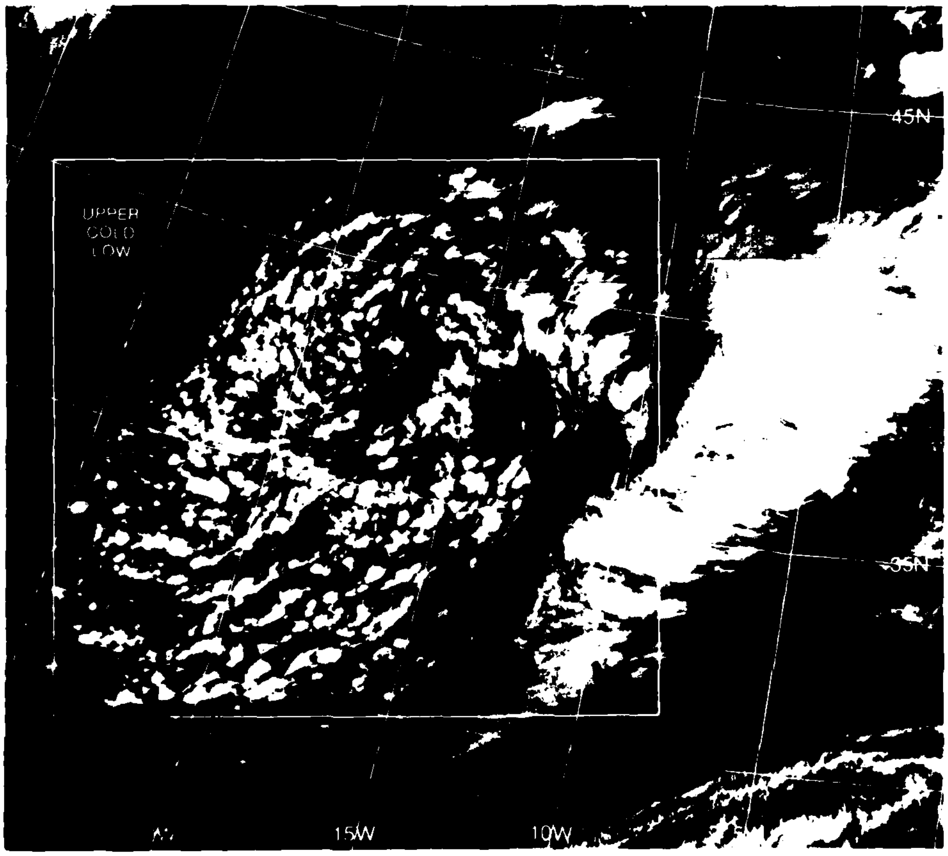

DMSP WHR I-Normal Enhancement. 0715 GMT 4 February 1976.

Cyclogenesis in Elongated Polar Troughs

The deformation of upper-tropospheric flow connected with the deepening of waves in the westerlies often results in the formation of elongated polar troughs that extend over long distances equatorward of the main polar jet stream. When this flow regime exists over the western Mediterranean, cyclogenesis is often observed in the polar trough. The cyclones that form are generally small-scale vorticies that do not deepen appreciably unless there is an interaction with strong low-level baroclinity. Rapid deepening of these cyclones is observed during the winter when strong cold fronts penetrate into the region.

A typical example of an elongated polar trough pattern over the western Mediterranean is shown in the 300-mb analysis in Fig. 3A-10a. The main polar jet is located north of 60° N and extends east and west in a broad sinusoidal wave pattern. A branch of the flow curves sharply westward around the anticyclone over the British Isles and then eastward over the Mediterranean, where an equatorward branch of the polar jet can be identified by the high wind speeds over the area. The polar trough over the western Mediterranean is well defined at 300 mb and has persisted in this region for the past several days.

The DMSP view on this day (Fig. 3A-11a) shows a comma-shaped cloud pattern associated with a cyclone that has formed in the polar trough over the western Mediterranean. There is a weak surface low-pressure area beneath the cyclone and a closed circulation at 700 mb (not shown). The bright cirrus cloud band to the south is a branch of the subtropical jet and, in combination with the polar jet, produces the broad band of high wind speeds aloft over North Africa.

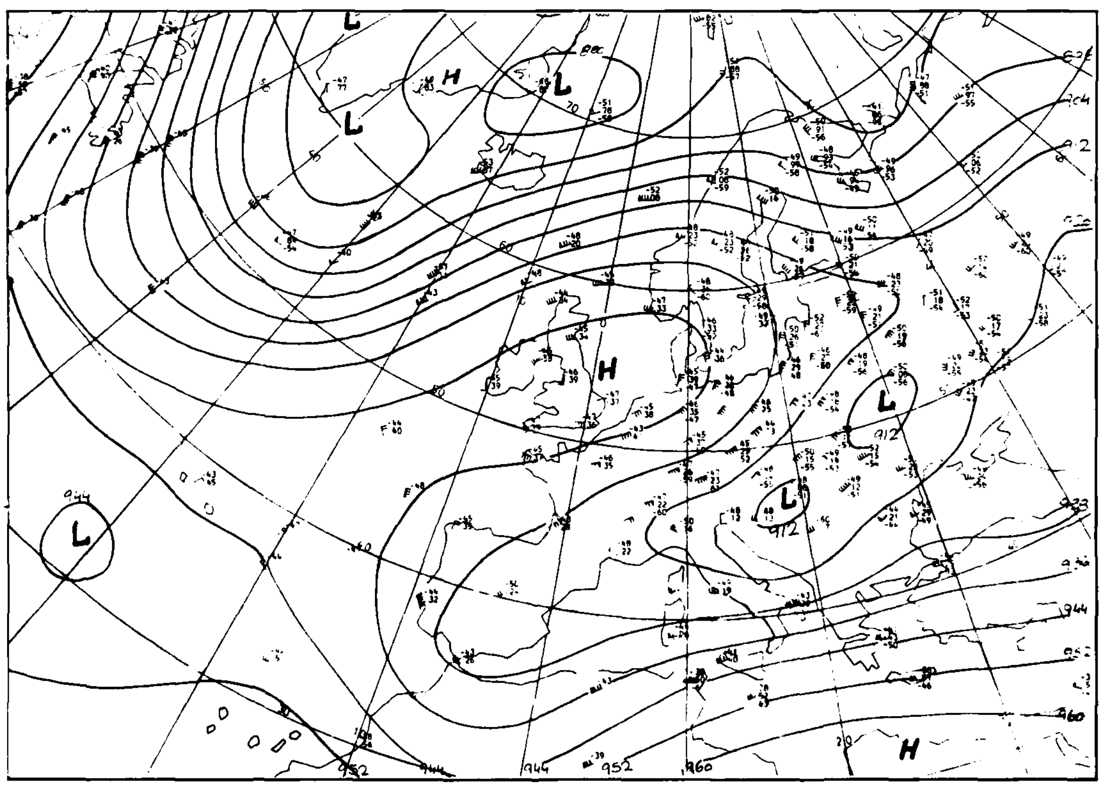

3A-10a. European Meteorological 300-mb Analysis 0000 GMT 28 May 1978.

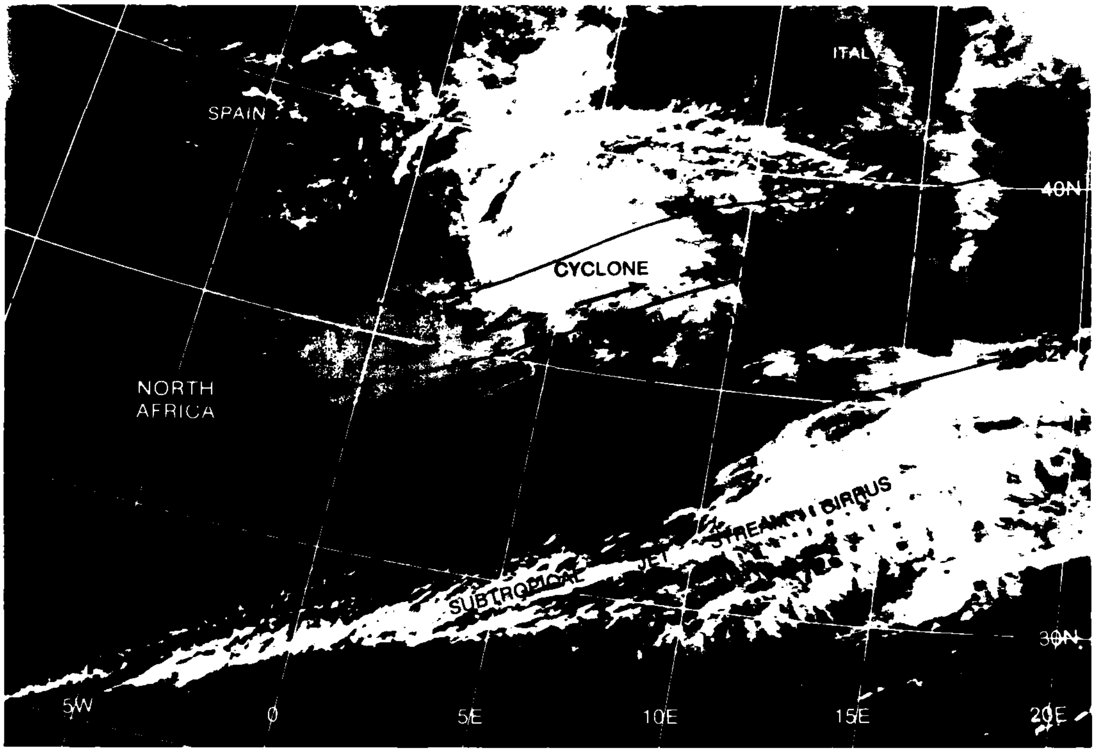

3A-11a. F-1. DMSP FS I-Normal Enhancement. 1033 GMT 28 May 1978.

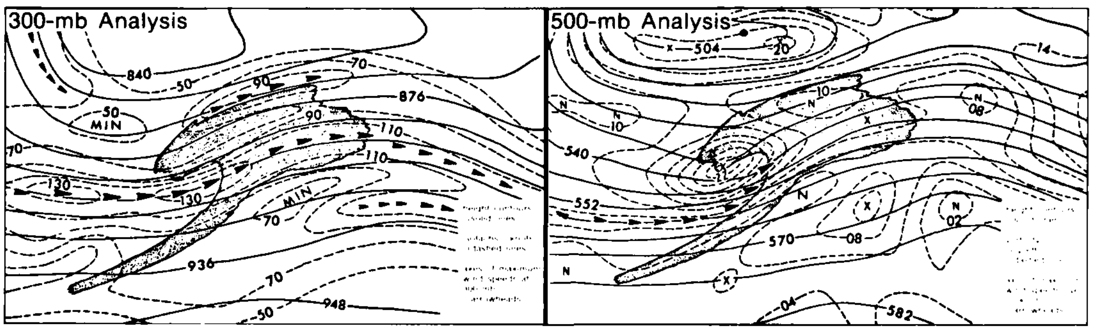

3A-11b. Cloud comma system in an early phase of development.

These cyclones form in areas of positive vorticity advection associated with wind speed maxima in nearly straight flow polar jet streams. In Fig. 3A-11b, Weldon (1979) gives an example of the early phase of development of such cyclones, as revealed by the attendant comma-shaped cloud pattern and wind field at 300 mb and at 500 mb. Note that the curved cirrus cloud band north of the cyclone is an area of higher wind speeds as shown in the cloud pattern at 300 mb. In these schematic drawings, a jet maximum (or jet streak) is found in the notch under the comma head. This is typical for the early phase of development. The left front quadrant of the jet maximum is an area of strong upper-level divergence and is therefore the most favorable sector for cyclogenesis along jet streaks, as shown in the accompanying diagram. In developing cyclones this sector is superimposed on the surface low.

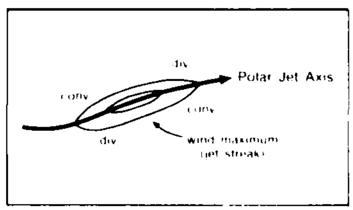

Reference

Weldon, R., 1979: Cloud Patterns and the Upper Air Wind Field. Part 4. Satellite Training Course Notes, Applications Laboratory, NESS, Washington, D.C.

Intense Cyclogenesis—Hurricane Flossie/Frontal Zone Interaction
Central North Atlantic
September 1978

15 September

At 0000 GMT the 500-mb analysis (3B-2a) shows an upper-level trough which has moved from North America into the North Atlantic. Ahead of the trough is a frontal zone marked by a long, broad band of cirrus as seen in the DMSP infrared image (3B-3a). The sharp edge along the cirrus cloudiness to the northwest indicates a strong polar jet stream. South of the frontal zone is Hurricane Flossie which has been moving slowly northeastward ahead of the trough. The concurrent surface analysis (3B-2b) shows the location of Hurricane Flossie relative to the frontal zone.

In the descending DMSP pass (3B-5a), about 10 hours later, Hurricane Flossie has moved closer to the frontal cloud band. The superimposed 500-mb analysis reveals that Flossie and the frontal zone are located in advance of the upper trough; an area of maximum positive vorticity advection (PVA MAX). The juxtoposition of these systems also enhances the baroclinicity along the frontal zone. The PVA MAX and enhanced baroclinicity favor explosive cyclogenesis and absorption of the hurricane within the frontal zone.

The FNOC PE 24-hour surface prognosis (3B-4a) shows a 1003-mb low near 48°N, 31°W, and the 48-hour prognosis (3B-4b) shows a 1011-mb low centered near 50°N, 20°W. These prognoses do not indicate a particularly intense development.

It is evident from the DMSP image at 2100 GMT (3B-6a) that *Hurricane Flossie* is merging with the frontal zone. In the extreme northwest portion of the picture, note the distinct S-shaped edge to the cirrus cloudiness. This pattern indicates that a frontal-wave development is in progress.

16 September

The NMC surface analysis at 0000 GMT (3B-7a) does not show the frontal-wave development in the vicinity of Flossie that was implied from the satellite image. However, the curvature of the front on the analysis suggests that a frontal wave could be accommodated, placing Flossie in the warm sector of the frontal wave.

The 24-hour FNOC PE surface prognosis (3B-7b), verifying at 0000 GMT on 17 September, shows a single low pressure system of 982 mb over the Norwegian Sea with a short-wave trough approaching Scotland.

17 September

The NMC surface analysis at 0000 GMT (3B-8a) shows a deep, occluded low (965 mb) centered over the Norwegian Sea, about 500 n mi south-southeast of the forecast position. Its speed of movement has averaged over 50 kt during the past 24 hours and the storm has a considerably lower central pressure than forecast.

In a DMSP image at approximately the same time (3B-9a) the low appears as a series of tight, concentric cloud spirals indicative of a very intense system. The streaky character of the high clouds around the vortex center suggests that strong winds are present at upper levels. The cloud lines and wave clouds, at lower levels southwest of the storm, are evidence of strong, low-level winds.

H.M.S. *Ark Royal*, operating in the southern Norwegian Sea, recorded the series of observations shown in 3B-8b. The meteorological officer on board gave the following account of the storm: "The waves were among the largest I have ever observed, heights of 40 to 60 ft at times and 200 to 250 ft between peaks. Gusts frequently exceeded 70 kt, though the mean wind speed never exceeded hurricane force. For 16 hours the fleet made good about 2 to 3 kt."

Important Conclusions

1. An S-shaped poleward edge to frontal band cirrus cloudiness is indicative of a frontal-wave development in progress.

2. The absorption of a decaying tropical cyclone into an area of a frontal zone where a wave development is in progress can lead to intense cyclogenesis.

15 September

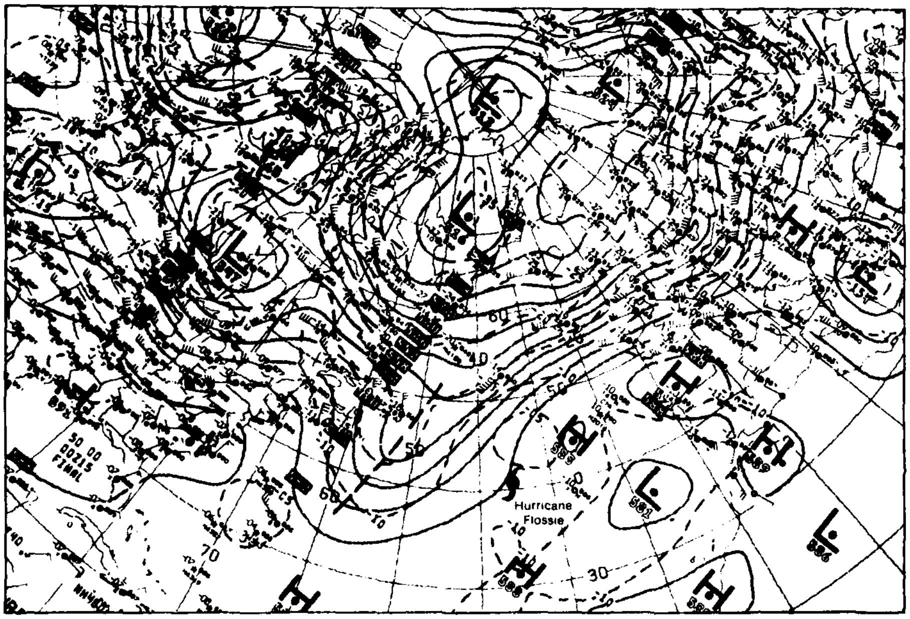

3B-2a. NMC 500-mb Analysis. 0000 GMT 15 September 1978.

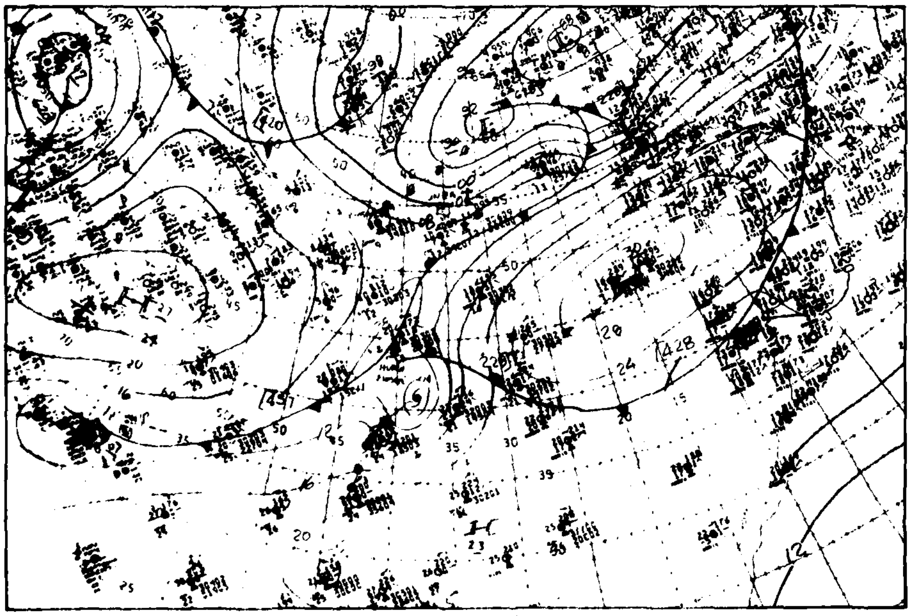

3B-2b. NMC Surface Analysis. 0000 GMT 15 September 1978.

Case 1 Cyclogenesis

Intense Cyclogenesis— Tropical Cyclone/Frontal Zone Interaction

Tropical cyclones often move poleward into midlatitudes where they encounter frontal zones and short-wave troughs in the westerlies. If the circulation of the tropical cyclone moves into the warm sector of a wave on the front, rapid intensification and an exceedingly strong extratropical cyclone may result (Petterssen, 1956).

Reference

Petterssen, S., 1956: *Weather Analysis and Forecasting*, Vol. I, McGraw-Hill Book Co., New York, pp. 364-370.

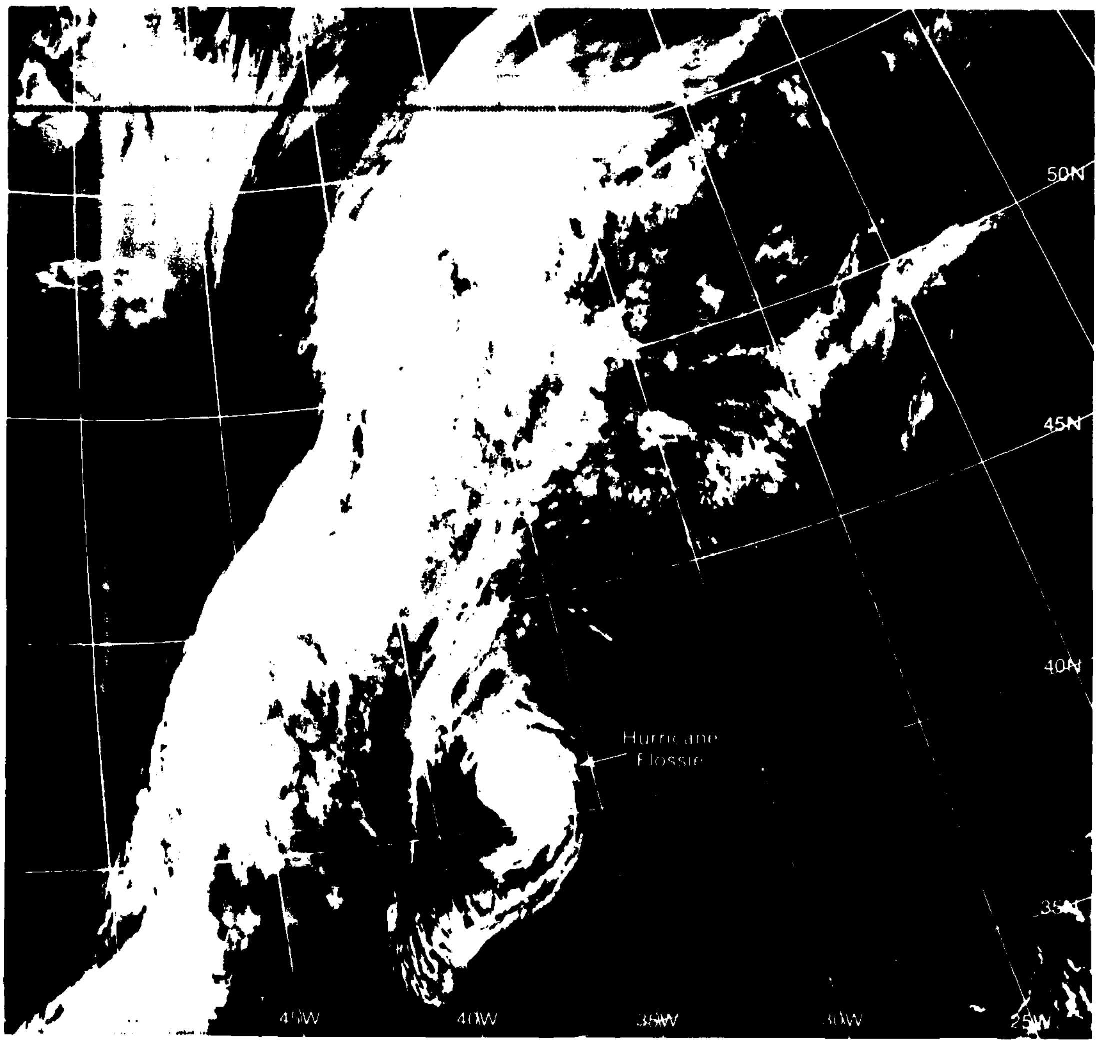

3B-3a. F-1. DMSP TF Normal Enhancement. 0229 GMT 15 September 1978.

15 September (continued)

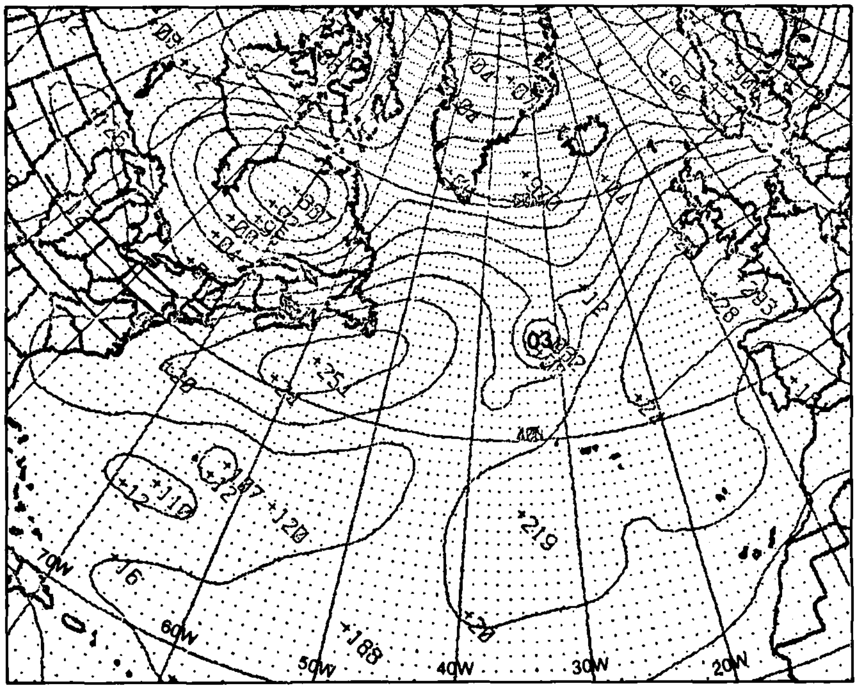

3B-4a. FNOC PE 24-Hour Surface Prognosis. Valid 0000 GMT 16 September 1978.

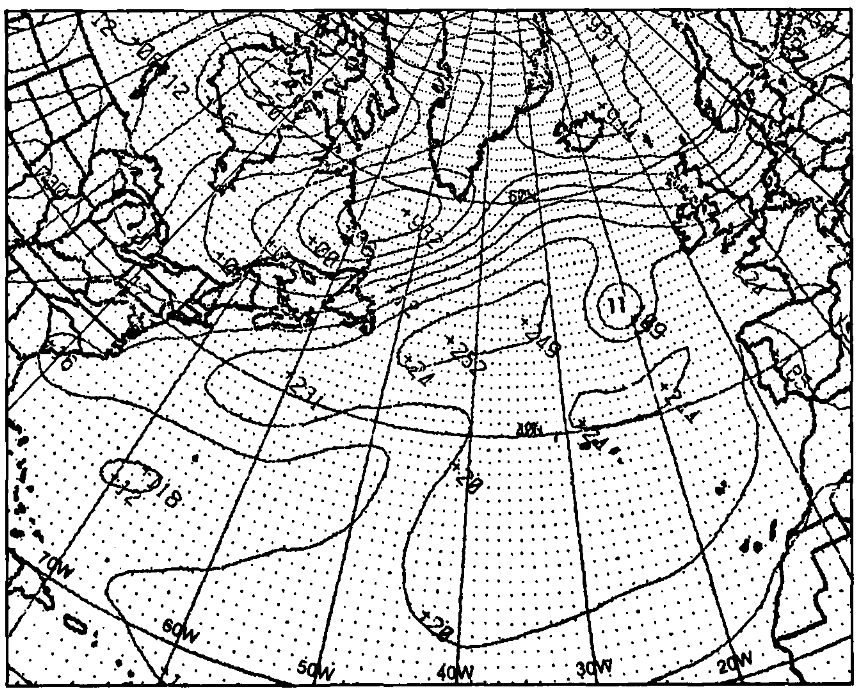

3B-4b. FNOC PE 48-Hour Surface Prognosis. Valid 0000 GMT 17 September 1978.

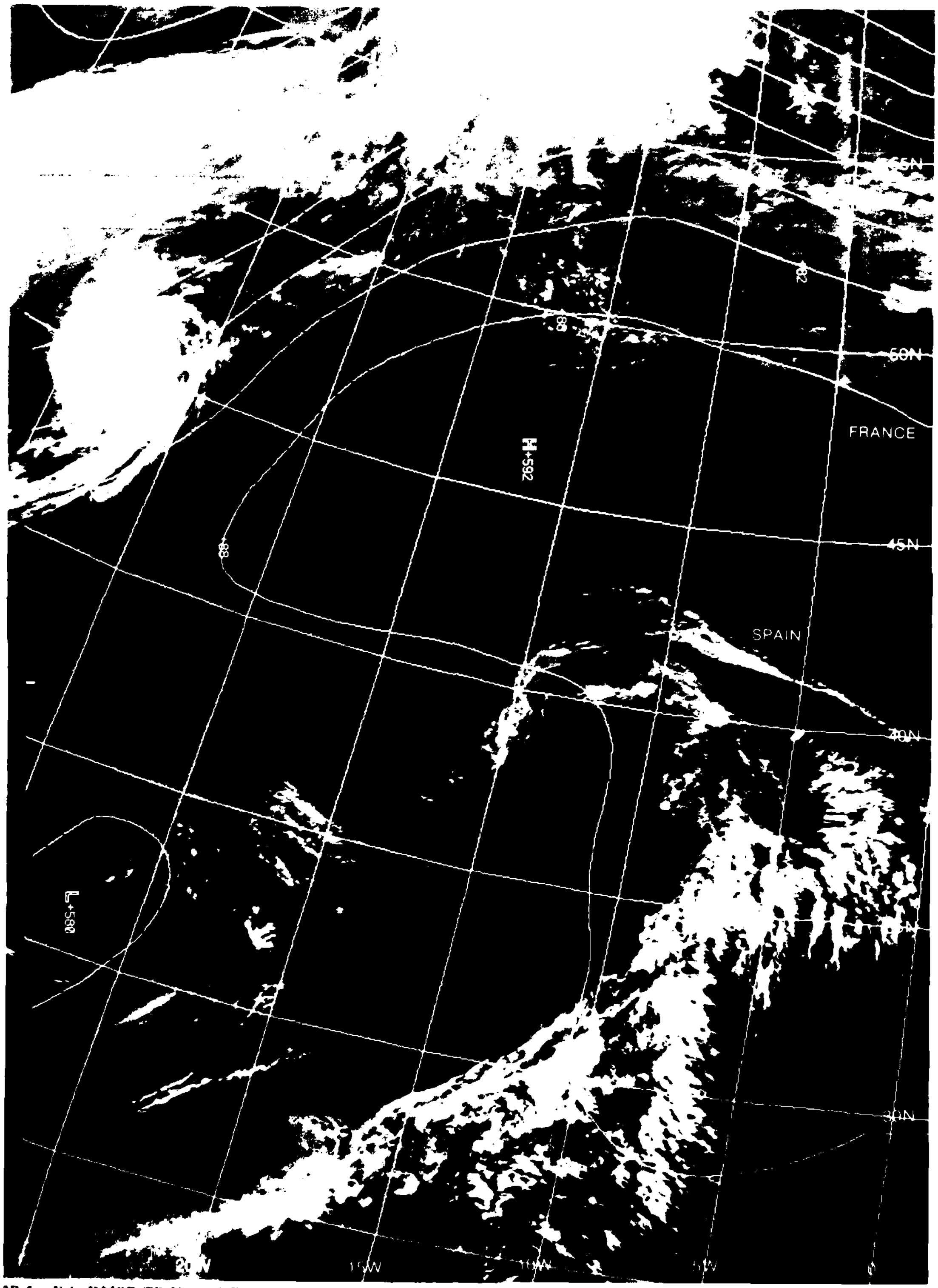

3B-5a. F-1. DMSP TS Normal Enhancement. 1148 GMT 15 September 1978.
FNOC PE Initial 500-mb Analysis. 1200 GMT 15 September 1978.

15 September (continued)

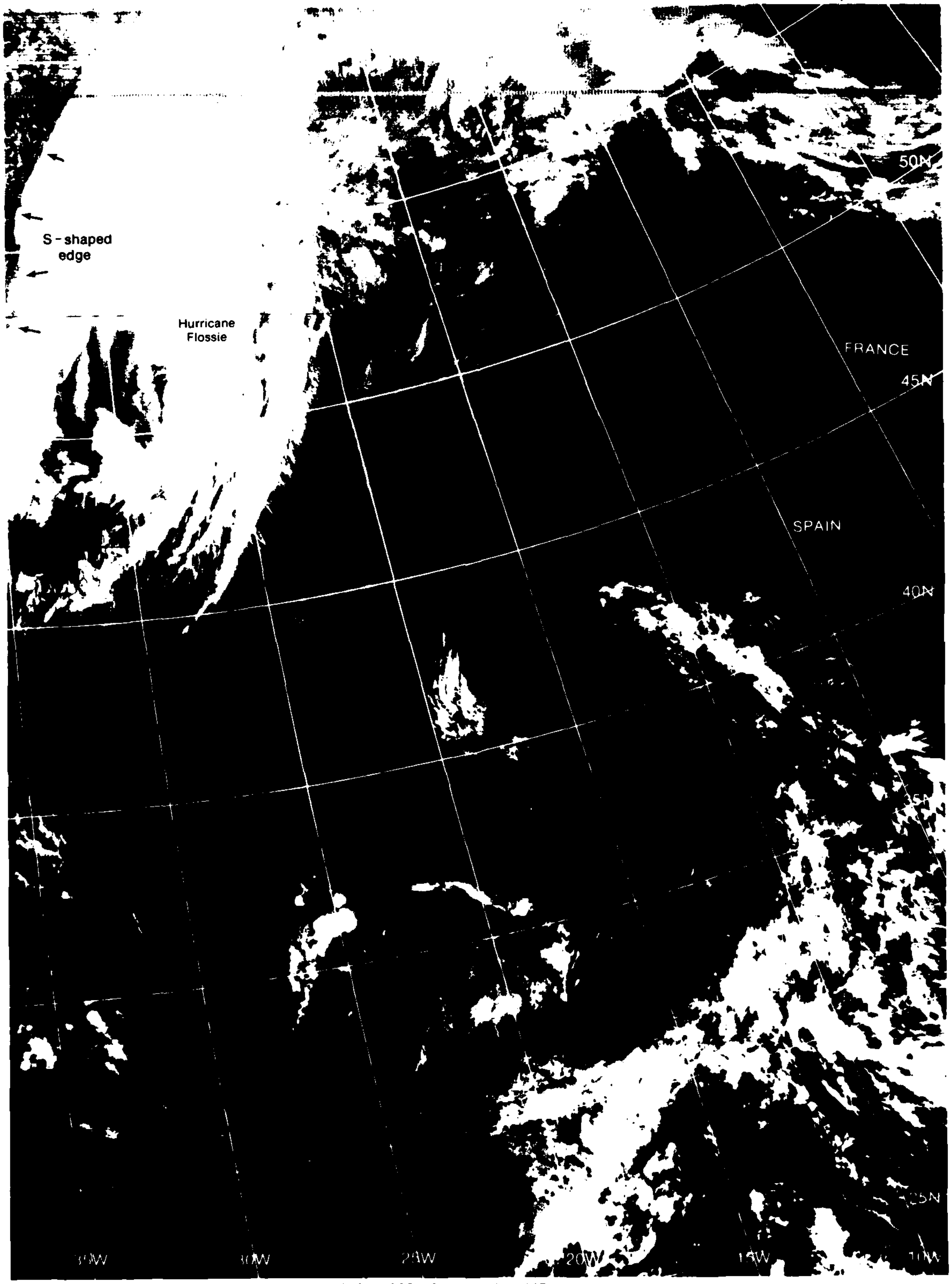

3B-6a. F-2. DMSP TF Normal Enhancement. 2154 GMT 15 September 1978.

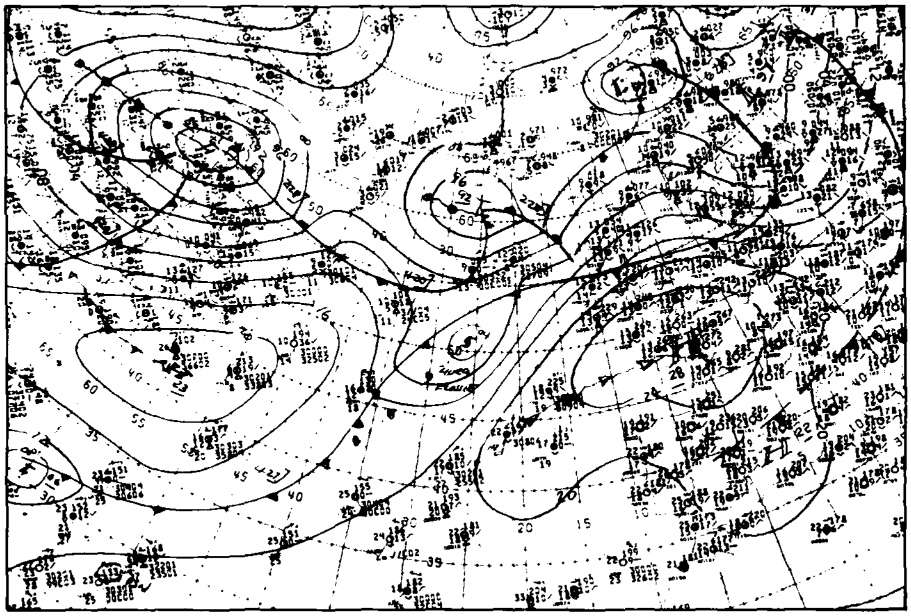

3B-7a. NMC Surface Analysis. 0000 GMT 16 September 1978.

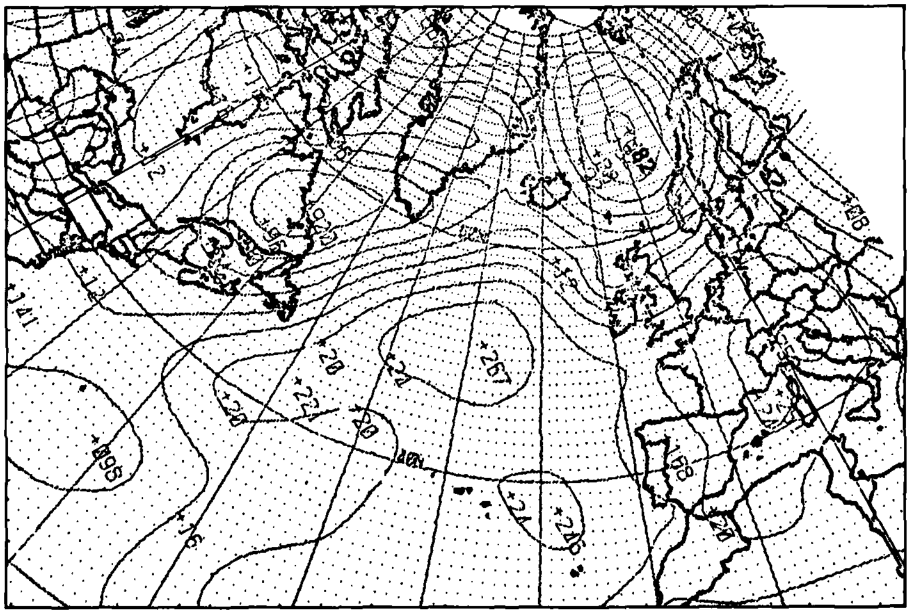

3B-7b. FNOC PE 24-Hour Surface Prognosis. Valid 0000 GMT 17 September 1978.

17 September

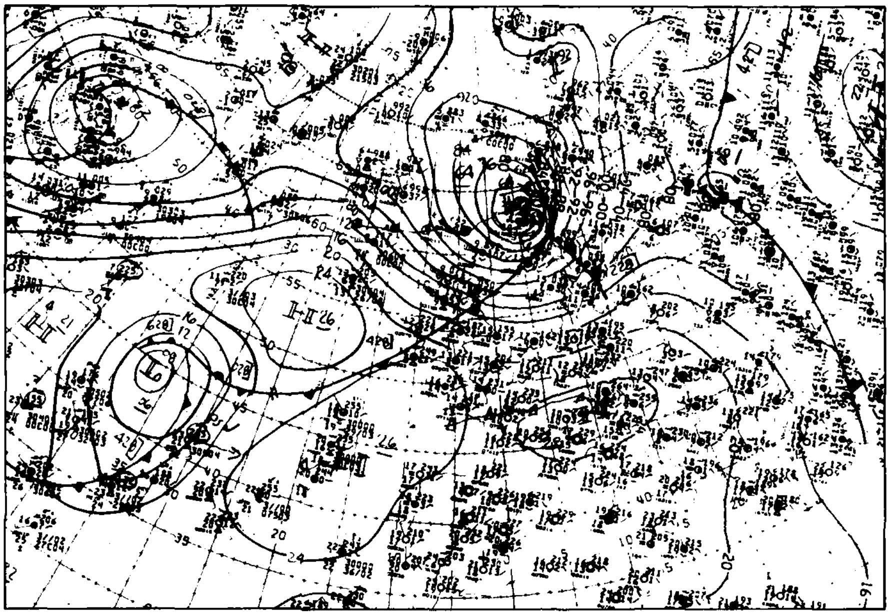

3B-8a. NMC Surface Analysis. 0000 GMT 17 September 1978.

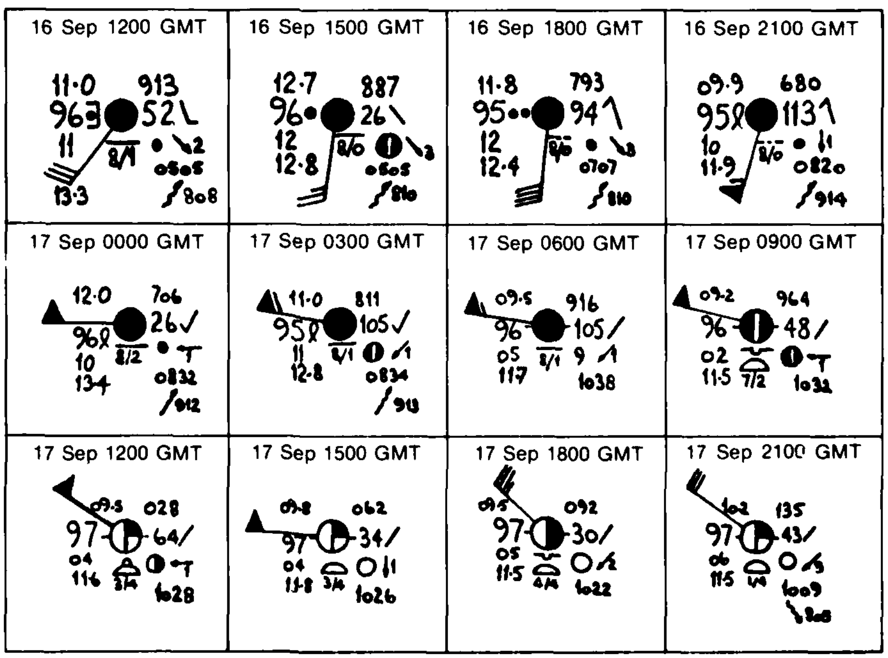

3B-8b. Surface Observations from H.M.S. *Ark Royal*.

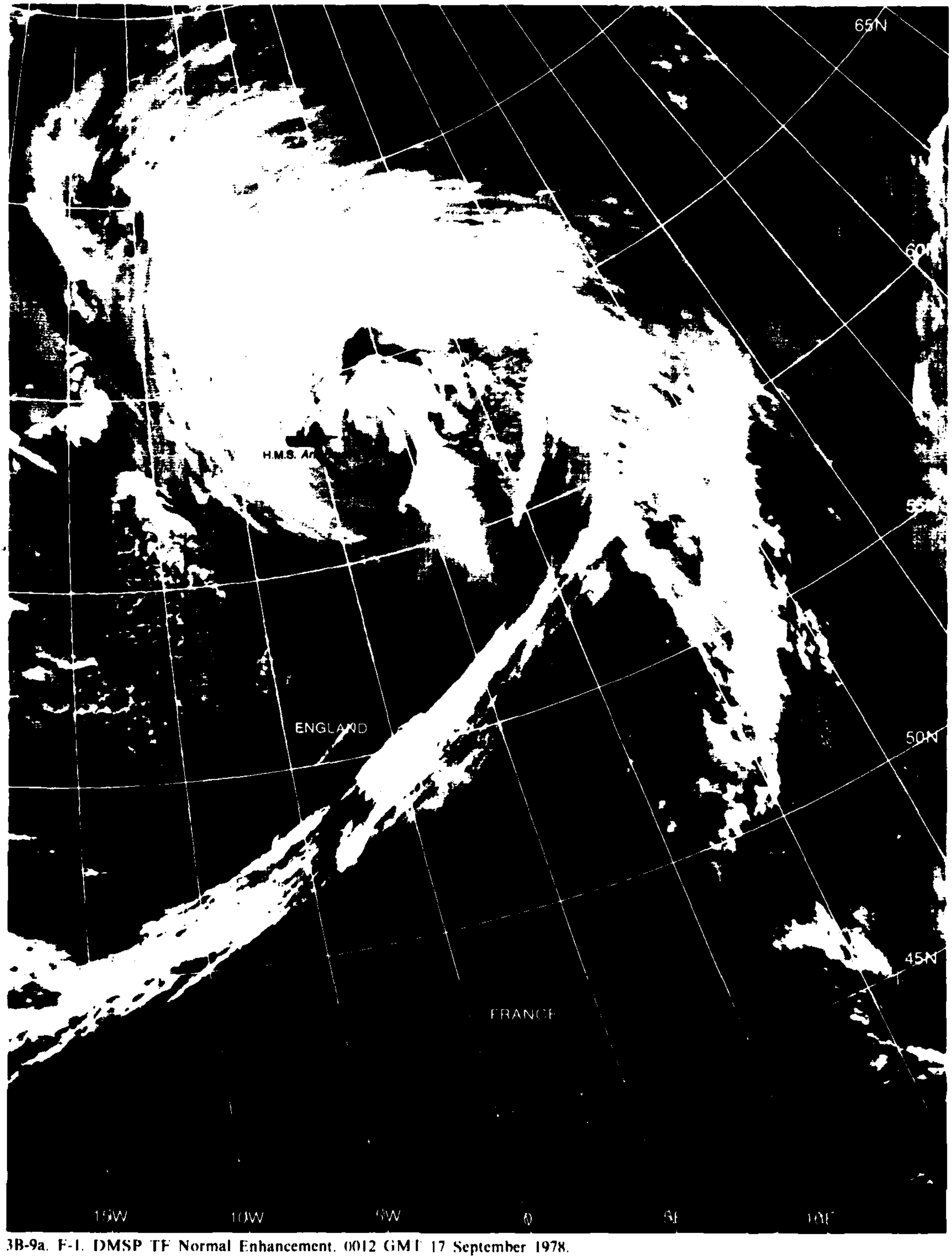

3B-9a. F-1. DMSP TF Normal Enhancement. 0012 GMT 17 September 1978.

Case 2 Cyclogenesis

Extratropical Storms of Hurricane Intensity

Information derived from satellite imagery is especially important over the oceans where surface observations tend to be sparse and erratic. Anderson and Veltishchev (1973) have described the normal life cycle of extratropical cyclones from the initial wave stage to the final occluded stage using satellite imagery. The development of a normal frontal wave is characterized by a widening and anticyclonic bending of the frontal cloud band. The associated vertical cloud development causes a bright appearance in both visible and infrared imagery.

In a study of severe extratropical cyclones over the eastern North Atlantic, Böttger, Eckardt, and Katergiannikis (1975) found that there were distinguishing cloud patterns which permit identification of the incipient stage of storms that will rapidly develop winds of hurricane intensity within a 12 to 24 hour period. These cloud patterns are characterized by a compact, anticyclonically curved cirrus canopy distinctly separate from other clouds and an extensive area of cellular convection behind the cold front.

References

Anderson, R.K., and N.F. Veltishchev, Eds., 1973: The use of satellite pictures [illegible] weather forecasting and analysis. WMO Tech. Note 124. World Meteorological Organization, New York, 275 pp.

Böttger, H., M. Eckardt, and U. Katergiannakis, 1975: Forecasting extra[illegible] cyclones with hurricane intensity using satellite information. *J. Appl. Met.*, 14, 1259-1265.

PRECEDING PAGE BLANK-NOT FILMED

AD-A099 591 BOHAN (WALTER A) CO PARK RIDGE IL F/G 4/2
NAVY TACTICAL APPLICATIONS GUIDE. VOLUME 3. NORTH ATLANTIC AND --ETC(U)
MAR 81 R W FETT, W A BOHAN N00228-79-C-3202

UNCLASSIFIED NEPRF-TR-80-07-VOL-3 NL

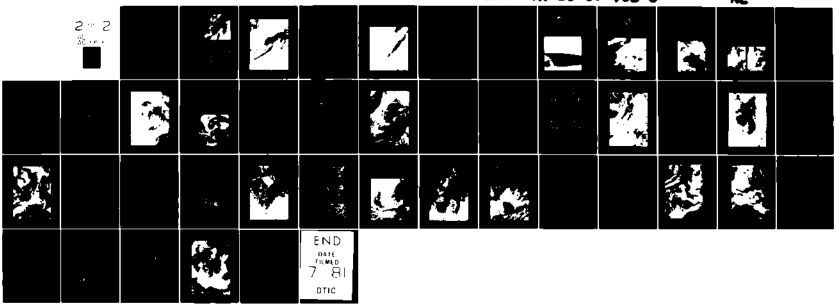

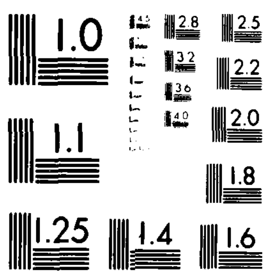

MICROCOPY RESOLUTION TEST CHART
NATIONAL BUREAU OF STANDARDS 1963 A

22 December

Two views of a developing wave disturbance are shown in 3B-12a (NOAA-5 infrared picture) and 3B-13a (DMSP visible picture). Note that a compact, anticyclonically curved cirrus canopy or "cloud head" is present over the disturbed area. West of the disturbance, an extensive area of open cellular cloudiness marks the advection of cold, unstable air into the developing system. These are precursors of a storm which will rapidly develop winds of hurricane intensity.

At the surface (3B-12b) the depression is centered near 35°N, 31°W with a central pressure of 990 mb. The occlusion process has begun and the strongest winds are to the west of the storm center. The FNOC 500-mb analysis, superimposed on the DMSP picture (3B-13a), reveals that this disturbance has formed along the leading edge of a short-wave trough at upper levels.

The FNOC PE 500-mb prognosis (3B-14a) is in good overall agreement with the position of the long-wave trough in the verifying analysis (3B-14b), but the short-wave trough shown initially on the 500-mb analysis of 3B-13a has been smoothed out of the prognosis in 3B-14a. The result of this smoothing on the surface prognosis (3B-14c) is extreme, with the rapidly developing wave shown on the verifying analysis (3B-14d) being missed entirely.

23 December

In the DMSP picture near verifying time (3B-15a) the storm appears as a large, comma-shaped cloud pattern. The field of short cumulus cloud line segments south of the storm center suggests that surface wind speeds are high in that area (see NTAG, Vol. 2, Sec. 1B, Case 5). This is confirmed by a ship report of 55 kt winds within this cloud field. The center of the storm is near ocean weather station Romeo (47°N, 17°W), with a central pressure of 978 mb. Romeo reported a pressure of 983 mb with winds of 40 kt and 20 ft seas.

The storm continued at near hurricane intensity and, on December 24, moved over the North Sea. A breakwater was rammed by the Belgian tank ship *Laguana* which then sank with the loss of a woman and three children. Additional loss of lives occurred as other ships sank, went adrift or aground in the hurricane force winds off southwest England, Wales, and in the English Channel (Mar. Wea. Log, 1978).

Important Conclusion

1. Distinguishing features of an explosively developing storm likely to develop hurricane force winds within the next 24 hours are a compact, anticyclonically curved cirrus canopy over the central area of the disturbance, and an extensive field of open cellular cloudiness marking the advection of cold, unstable air into the system.

Reference

NOAA, 1978: Monster of the Month, December 1977. *Mar. Wea. Log*, **22**, 129 130.

22 December

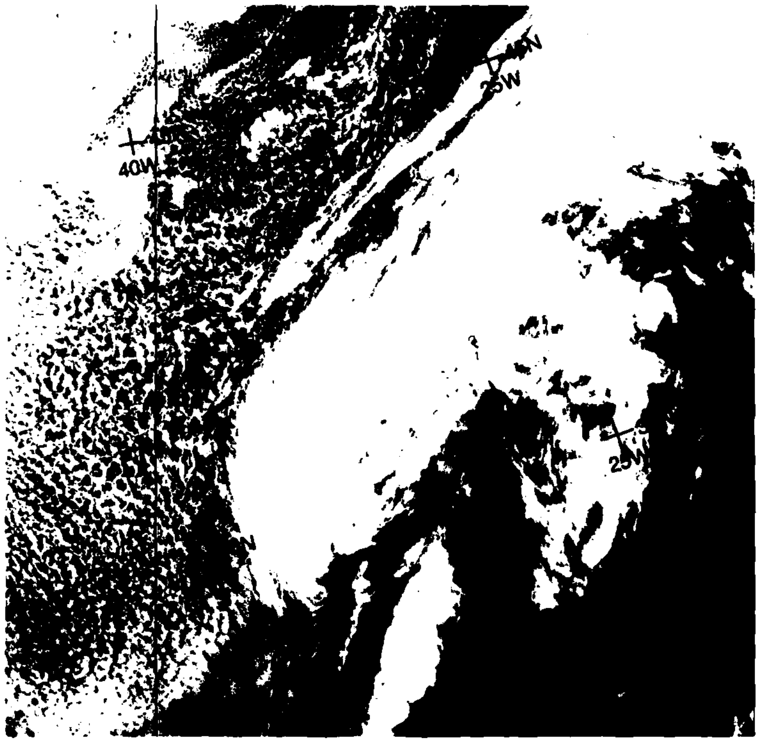

3B-12a. NOAA-5. Infrared Picture, 0.5 n mi Resolution. 1051 GMT 22 December 1977.

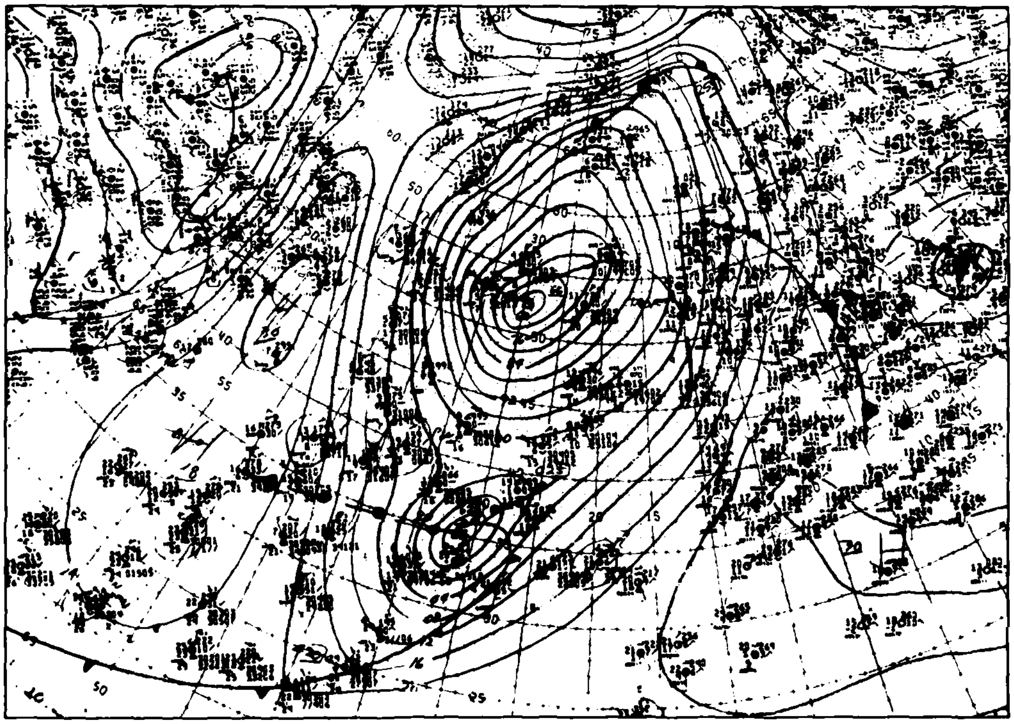

3B-12b. NMC Surface Analysis. 1200 GMT 22 December 1977.

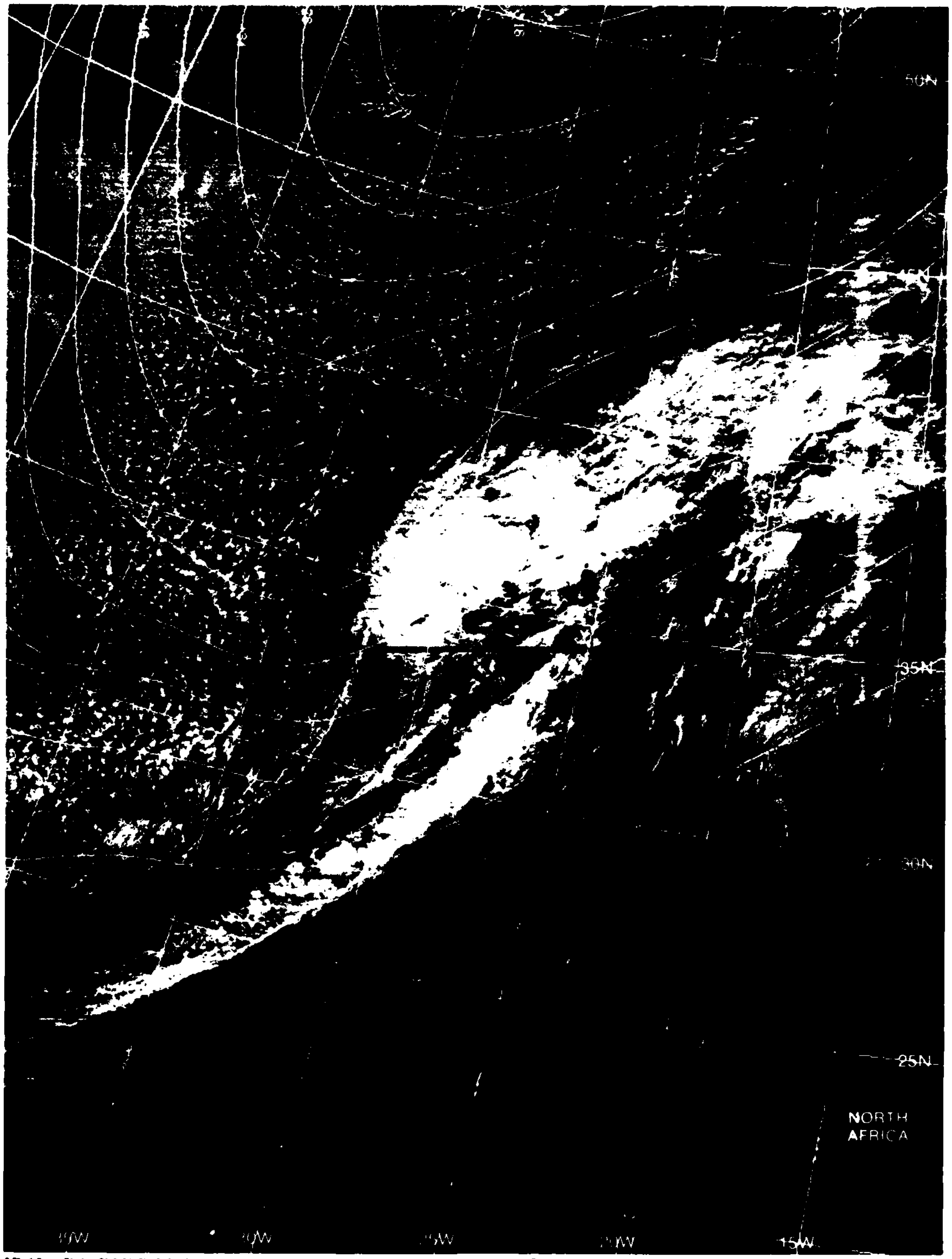

3B-13a. F-1. DMSP LF Low Enhancement. 1249 GMT 22 December 1977.
FNOC PE Initial 500-mb Analysis. 1200 GMT 22 December 1977.

23 December

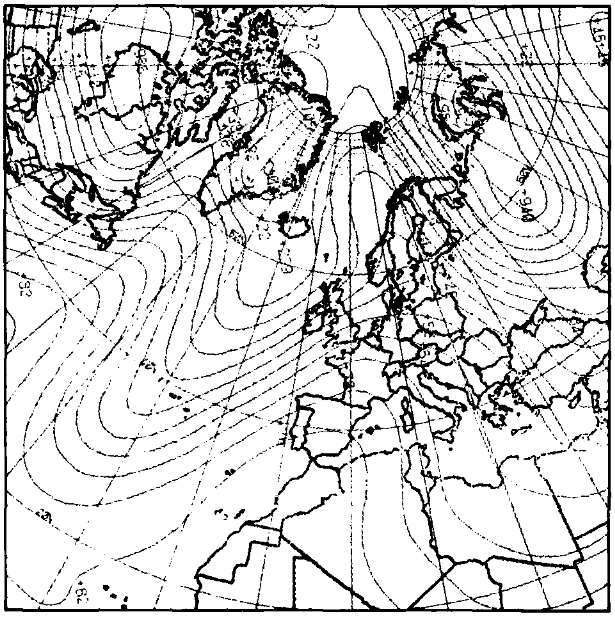

3B-14a. FNOC PE 24-Hour 500-mb Prognosis.
Valid 1200 GMT 23 December 1977.

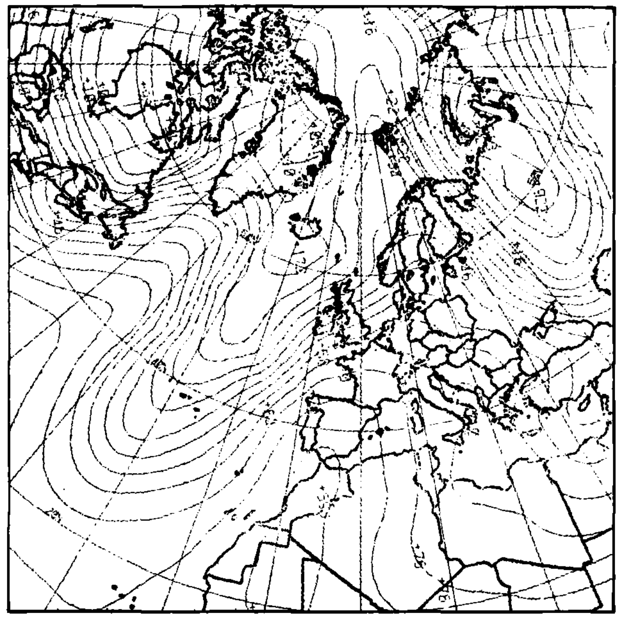

3B-14b. FNOC PE Verifying 500-mb Analysis.
1200 GMT 23 December 1977.

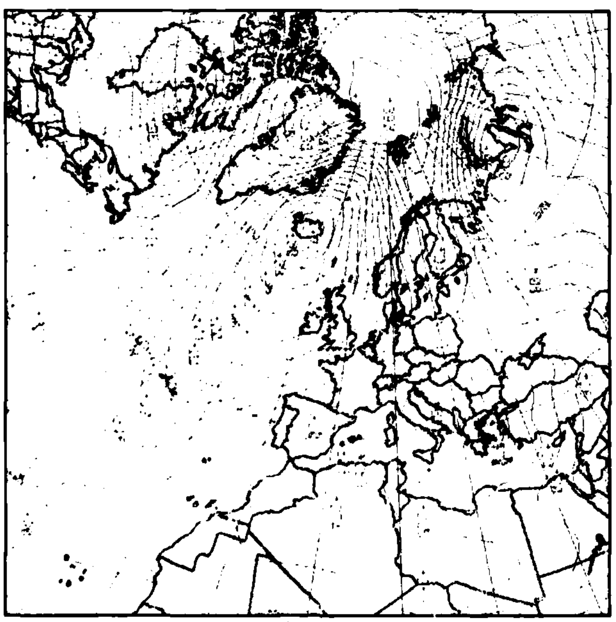

3B-14c. FNOC PE 24-Hour Surface Prognosis.
Valid 1200 GMT 23 December 1977.

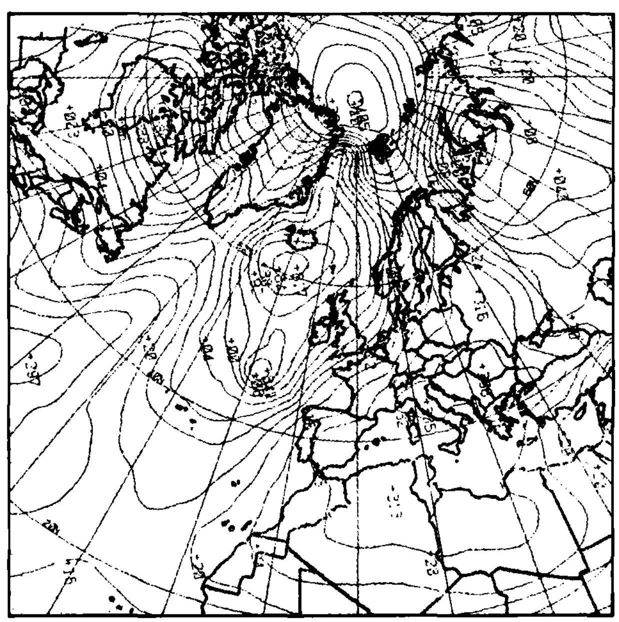

3B-14d. FNOC PE Verifying Surface Analysis.
1200 GMT 23 December 1977.

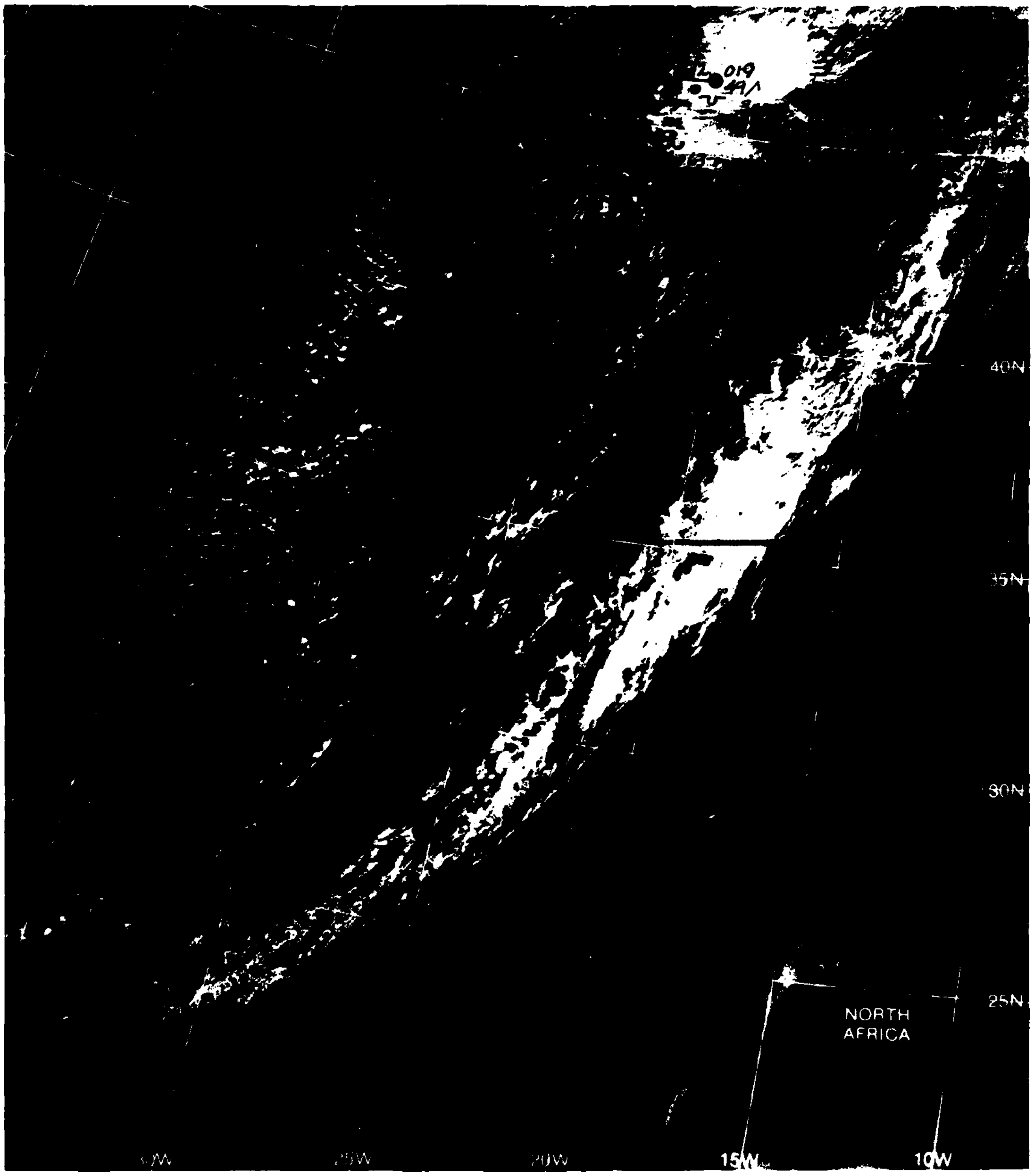

3B-15a. F-1. DMSP LF Low Enhancement. 1234 GMT 23 December 1977. Surface Observations. 1200 GMT 23 December 1977.

Case 3 Cyclogenesis

Intensification of Orographically Induced Vorticies

The occurrence of a mesoscale cloud eddy over the Atlantic Ocean to the west of the Strait of Gibraltar has been described by Anderson et al. (1974) to be the result of orographically induced cyclonic shear at low levels. This cyclonic shear is the combined result of both northerly and easterly flow (3B-17a). Northerly flow is modified by the higher terrain of the Iberian Peninsula creating a shear zone between the calm air in the lee of the land and the unobstructed northerly flow further west. Easterly flow is funneled in Venturi fashion through the Strait of Gibraltar producing cyclonic shear to the southwest. Also helping to maintain the eddy circulation is channeling created by the coastal mountain range of Morocco. These vorticies can further develop through interaction with a short-wave trough and can become significant local weather producers.

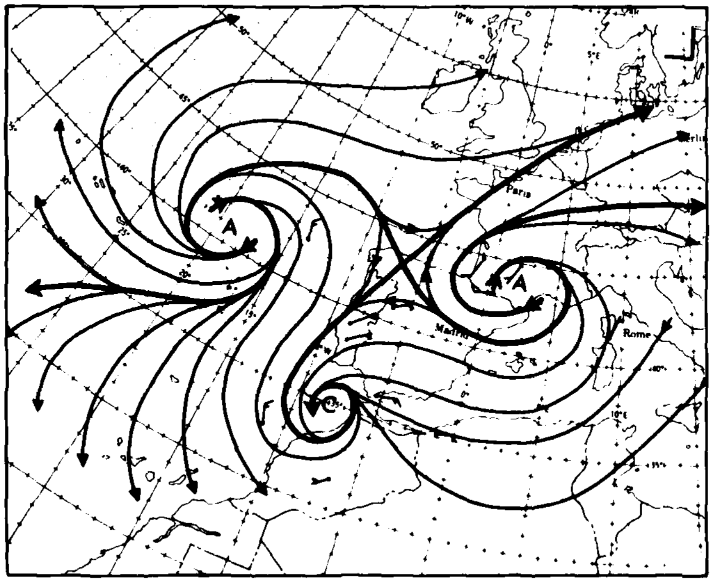

3B-17a. Surface Wind Reports and Streamline Analysis. 6 June 1966 (after Anderson et al., 1974).

Reference

Anderson, R.K., et al., 1974: Applications of meteorological satellite data in analysis and forecasting. ESSA Tech. Report NESC 51 (including supplement, Nov. 1971, and supplement No. 2, Mar. 1973)., National Environmental Satellite Service, NOAA, Washington, D.C., 350 pp.

PRECEDING PAGE BLANK-NOT FILMED

Orographically Induced Vortex/Short-wave Trough Interaction
Eastern North Atlantic
June 1975

19 June

Views of two different mesoscale cloud eddies west of the Strait of Gibraltar are shown in 3B-18b and 3B-19b. The first view is a Gemini 10 photograph taken on 20 June 1966, while the second is a DMSP visible picture from 19 June 1975. The synoptic situation in these two cases is very similar. Both views show a build-up of low clouds along the North African coast and over the Alboran Channel. Under conditions of easterly flow, the mountain ranges of Spain and North Africa cause funneling of air into the Strait of Gibraltar resulting in convergence and cloud formation. Thus, the presence of such low cloudiness is a good indication that the low-level flow is easterly. The larger amount of cloudiness in the DMSP picture suggests that there is a greater supply of moisture present on this day. Both views also show a field of closed cellular stratocumulus in the stable northerly flow to the west of the eddy. The surface analysis for 1200 GMT (3B-19a) shows the flow patterns in the vicinity of the eddy on that day. Note the presence of a heat low over central Spain.

Normally this vortex is not a major weather producer and it remains stationary as long as favorable conditions persist. However, the 500-mb analysis at 1200 GMT (3B-18a) shows a weak, upper-level trough to the west of the area. This trough, in conjunction with the low-level convergence and ample moisture supply, suggests that further development or intensification of this mesoscale vortex may occur.

20 June

A series of DMSP visible pictures taken this day show the development of cloudiness in the eastern portion of the mesoscale vortex. Notice that in the early morning picture (3B-20a), considerable high-level convective cloudiness has developed over the Gibraltar area. The low solar elevation angle highlights this cloudiness.

DMSP pictures taken later in the morning (3B-21b and 3B-21c) show that convection has developed through a deep layer and has spread into central Spain. Note that the cloud vortex, however, remains stationary west of Gibraltar.

Upper-air wind data from Gibraltar (3B-21a) reveals the passage of a weak trough during this day. Between 0000 GMT 19 June and 0000 GMT on 20 June the 700-mb and 500-mb winds backed from westerly to southerly indicating the approach of a trough from the west. In addition, temperature-dew point data (not shown) revealed a considerable moistening of the atmosphere. By 0000 GMT 21 June winds have returned to a westerly direction, marking the passage of the trough.

This example is interesting in that it indicates a mesoscale development not normally taken into consideration in numerical forecasts. It also shows how satellite imagery can alert a tactical forecaster to watch more closely a situation which is developing, in situ, in his forecast area.

Important Conclusions

1. Small, orographically induced eddies are normally not major weather producing systems.

2. When an upper-level, short-wave trough interacts with such an eddy, however, the eddy may develop and become a major weather producing system.

19 June

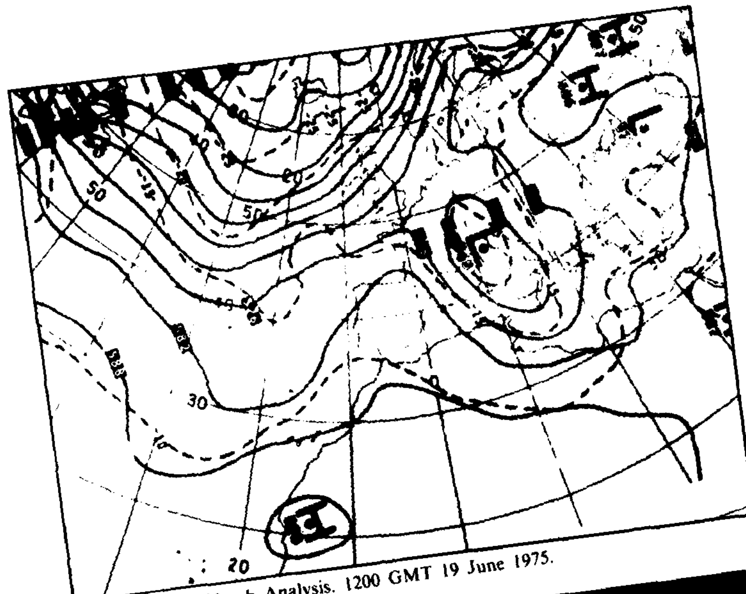

3B-18a. NMC 500 mb Analysis. 1200 GMT 19 June 1975.

3B-18b. Gemini 10 Photograph, Orbit 26, Frame 28. 20 July 1966.

19 June (continued)

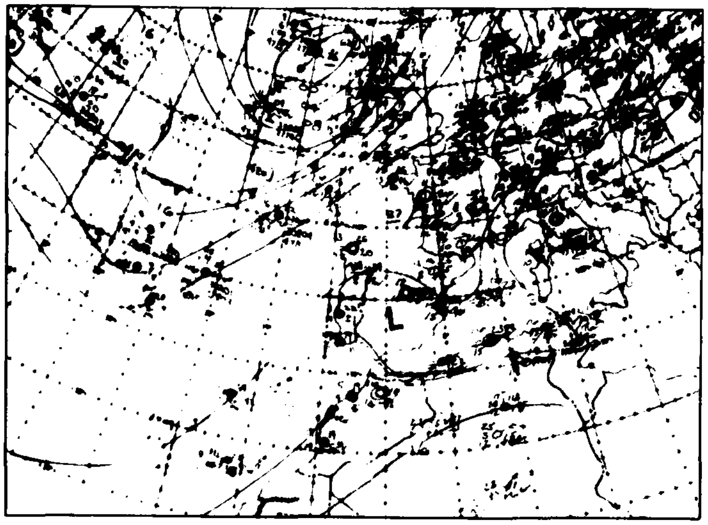

3B-19a. NMC Surface Analysis. 1200 GMT 19 June 1975.

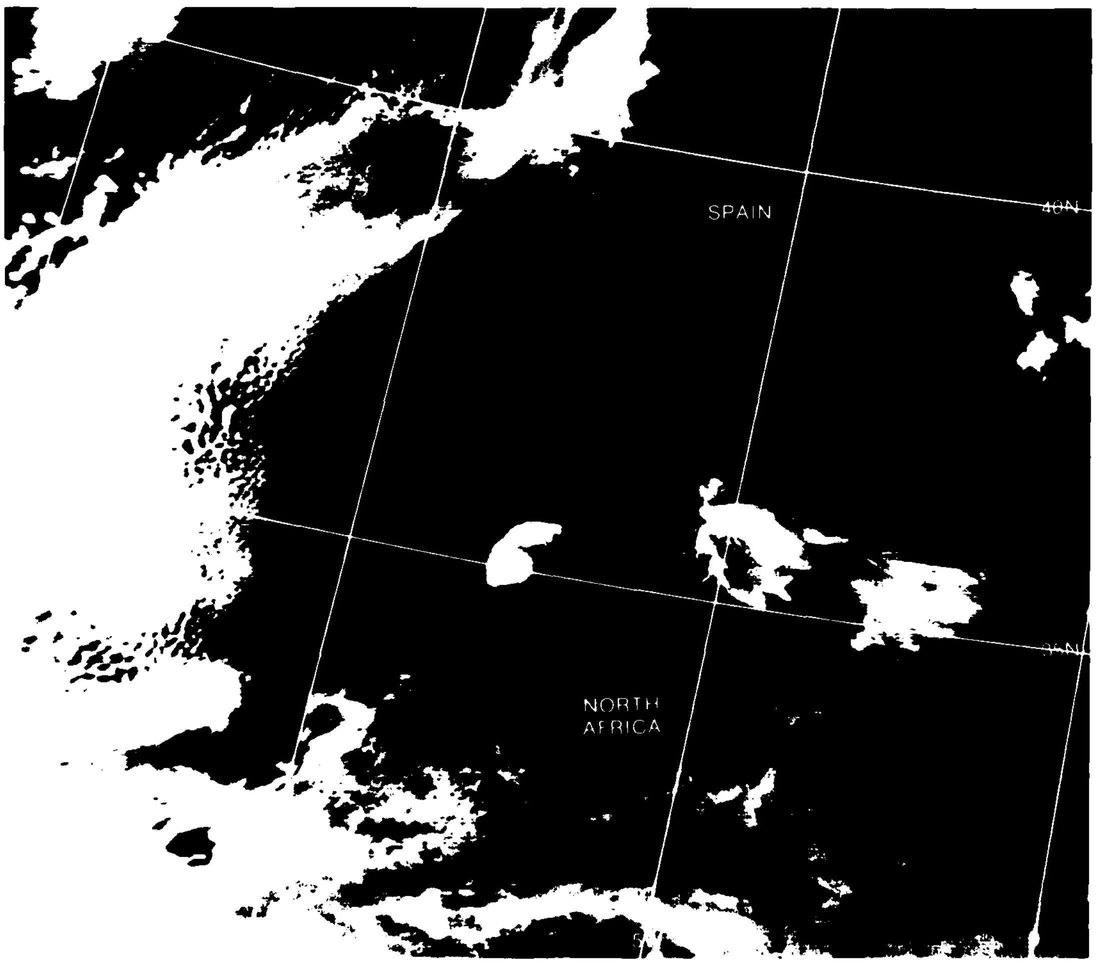

3B-19b. Enlarged View. FTV-33. DMSP VHR Low Enhancement. 0800 GMT 19 June 1975.

3B-20a. FTV-3.. DMSP VHR Normal Enhancement. 0549 GMT 20 June 1975.

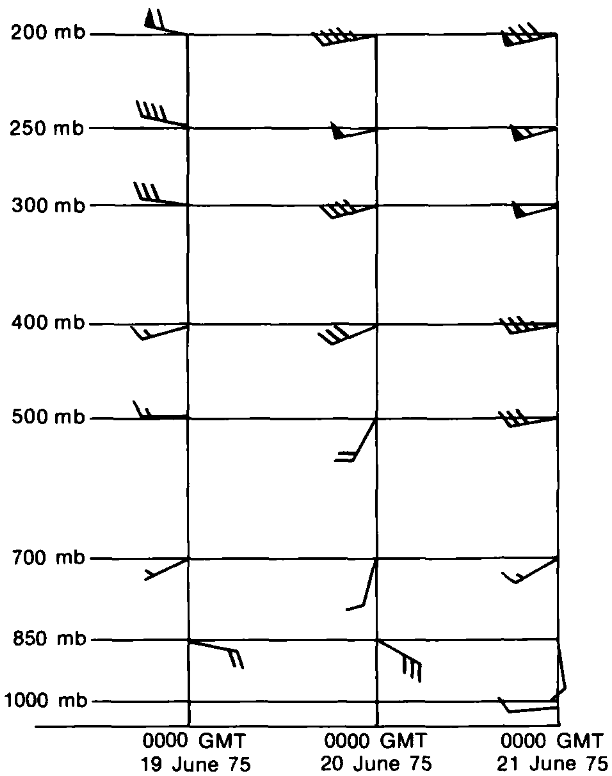

3B-21a. RAOB Winds from Gibraltar.

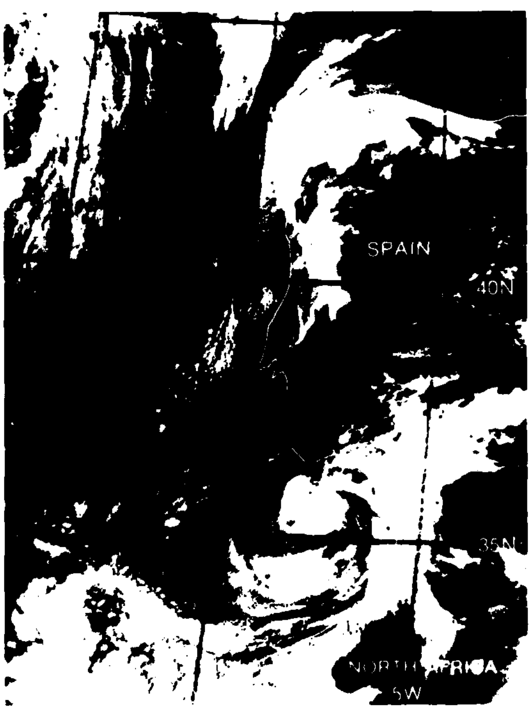

3B-21b. FTV—33. DMSP VHR Low Enhancement.
0930 GMT 20 June 1975.

3B-21c. FTV-31. DMSP VHR Low Enhancement.
1150 GMT 20 June 1975.

Case 4 Cyclogenesis

North African Depressions

Depressions which form to the south of the Atlas Mountains are referred to as North African lows or Atlas lee depressions. These storms are of concern to mariners since they may give rise to severe winds in the Strait of Sicily and sirocco conditions along the North African coast. They are to be differentiated from the Saharan heat low which, in itself, is not a significant weather producer.

Reiter (1975) states that a reliable criteria for the development of a North African depression is the presence of an upper-level trough over Spain with its axis oriented approximately northeast-southwest, producing deep southwesterly flow over northwest Africa. This trough may be mobile and, in a typical pattern, moves in conjunction with a surface low advancing southeastward across Europe, while the associated cold front advances southeast toward the Atlas Mountains. Brown (1964) suggests that the influx of moisture over the Atlas Mountains, due to the upper-level trough, appears to be necessary for the development of these storms.

References

Brown, W.F., 1964: Local area forecasters handbook. Naval Weather Service Environmental Detachment, Sigonella, Sicily, 48 pp.

Reiter, E.R., 1975: Handbook for forecasters in the Mediterranean, Part 1. ENVPREDRSCHFAC Technical Paper 5-75, Naval Air Systems Command, Dept. of the Navy, Washington, D.C., 344 pp.

High Winds and Sand during the Initial Development of a North African Depression Western Mediterranean May 1977

16 May

The 0000 GMT NMC surface analysis for this day (3B-24b) shows a weak low centered over the Bay of Biscay. Past positions for the low indicate that it is moving to the southeast. A cold front, also moving to the southeast, extends from the low through northern Italy, Morocco, and into the Atlantic. A Saharan heat low is present over southern Algeria near 22°N, 4°W. The 500-mb analysis (3B-24a) shows an upper-level, short-wave trough extending from a low over southern England. There is strong westerly flow at upper levels over north : Africa.

A DMSP infrared picture near this time (3B-25a) reveals cloudiness associated with the low over England and frontal cloudiness extending from northeast to southwest over the western Mediterranean. The Saharan heat low is centered on the west side of large cloudy area south of the frontal band.

The FNOC PE 36-hour surface prognosis (3B-24c) shows that the low initially over the Bay of Biscay will continue moving southeast into the western Mediterranean and deepen slightly. It also shows that the Saharan heat low will move to the northeast and deepen slightly. The two lows form a larger complex low pressure area over the western Mediterranean.

In a NOAA-5 visible picture taken later in the day (3B-26b), a comma-shaped cloud pattern is visible near 25°N, 0°W. This is in the vicinity of the Saharan heat low shown in the 1200 GMT surface analysis (3B-26a).

17 May

The surface analysis for 0000 GMT (3B-27b) shows that the cold front has now moved across the Atlas Mountains and has interacted with the Saharan heat low, resulting in the formation of a North African depression. The low over the Bay of Biscay has moved southeast into the western Mediterranean along with a second, weak cold front. At 500 mb (3B-27a), the low over England has become cut-off, while moving south over Spain, producing strong southwesterly flow over North Africa and the western Mediterranean. Since the criteria for development has been established, further intensification of the North African depression should be anticipated.

During the next 12 hours (3B-28b), the low over the Mediterranean dissipated, while the North African depression deepened and continued to move to the northeast. The development of the North African depression intensified the pressure gradient over the western Mediterranean. During the course of this intensification, large quantities of Saharan sand and dust were advected over the Mediterranean at low levels.

The DMSP picture at 1105 GMT (3B-29a) shows a large area of cloudiness in the region of southwesterly flow at 500 mb (3B-28a). The position of the North African depression remains well to the south of this cloudiness, according to the surface analysis (3B-28b).

The increasing pressure gradient and funneling effects caused a rapid increase in the easterly winds over the Mediterranean, particularly in the Sicilian Channel and downwind between Tunisia and Sardinia. U.S.S. *Pensacola*, operating near the southern tip of Sardinia, was reporting light and variable winds until 1100 GMT, but by 1300 GMT winds had increased to 24 kt from 070°. Winds continued to increase throughout the afternoon and by 2000 GMT reached 45 kt from 090°. Such a rapid increase in easterly winds over the Mediterranean is typical of North African depressions. Other ships operating in the area reported severe restrictions to visibility as a result of blowing sand and dust. In addition, there were reports of steady rain from middle-level cloudiness falling through the dust layer producing "red rain".

It is important to note that the major weather associated with the initial development of the North African depression was located well to the north of the depression center, under the southwesterly flow aloft. The weather was a result of the hot Saharan air ascending over the cool, moist air that had been advected southward behind the original cold front. The intensification of the surface pressure gradient, as the depression moved northward, was enhanced by strong upper-level divergence in the southwesterly flow of the trough aloft.

Important Conclusions

1. Over the Mediterranean, strong winds and steady rain (containing Saharan dust) are often observed as the forerunners of a North African depression, whose center may be located several hundred miles to the south over Africa.

2. During the intensification and northward movement of a North African depression, funneling effects can produce a rapid increase in easterly winds through the Strait of Sicily and to the south of Sardinia.

16 May

3B-24a.
NMC 500-mb Analysis.
0000 GMT 16 May 1977.

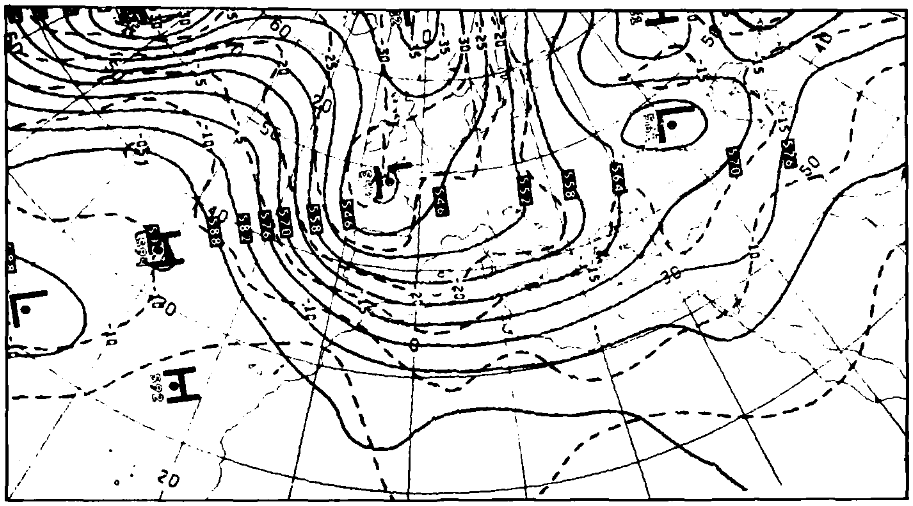

3B-24b.
NMC Surface Analysis.
0000 GMT 16 May 1977.

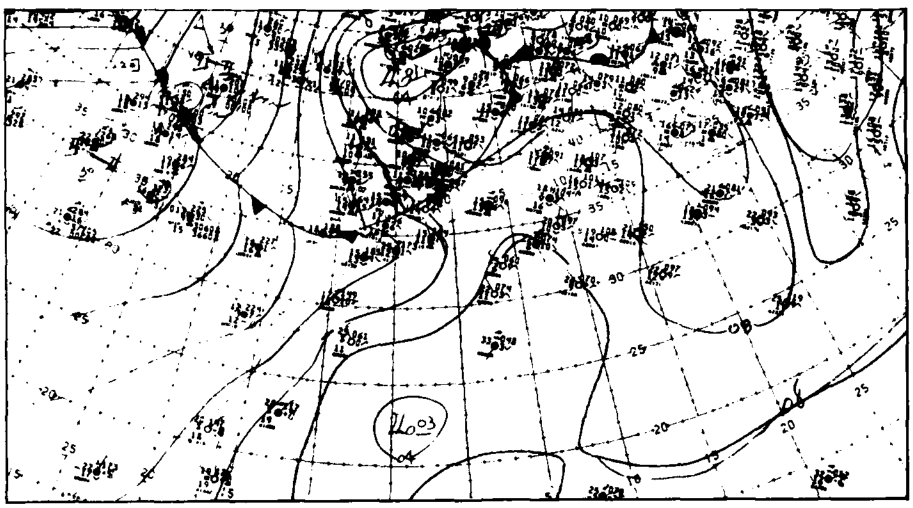

3B-24c
FNOC PE 36-Hour
Surface Prognosis
Valid 1200 GMT
17 May 1977.

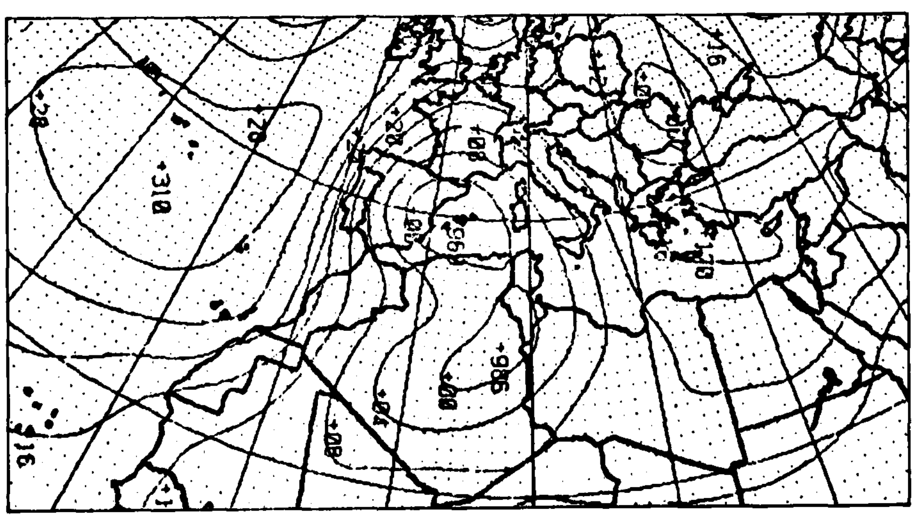

16 May (continued)

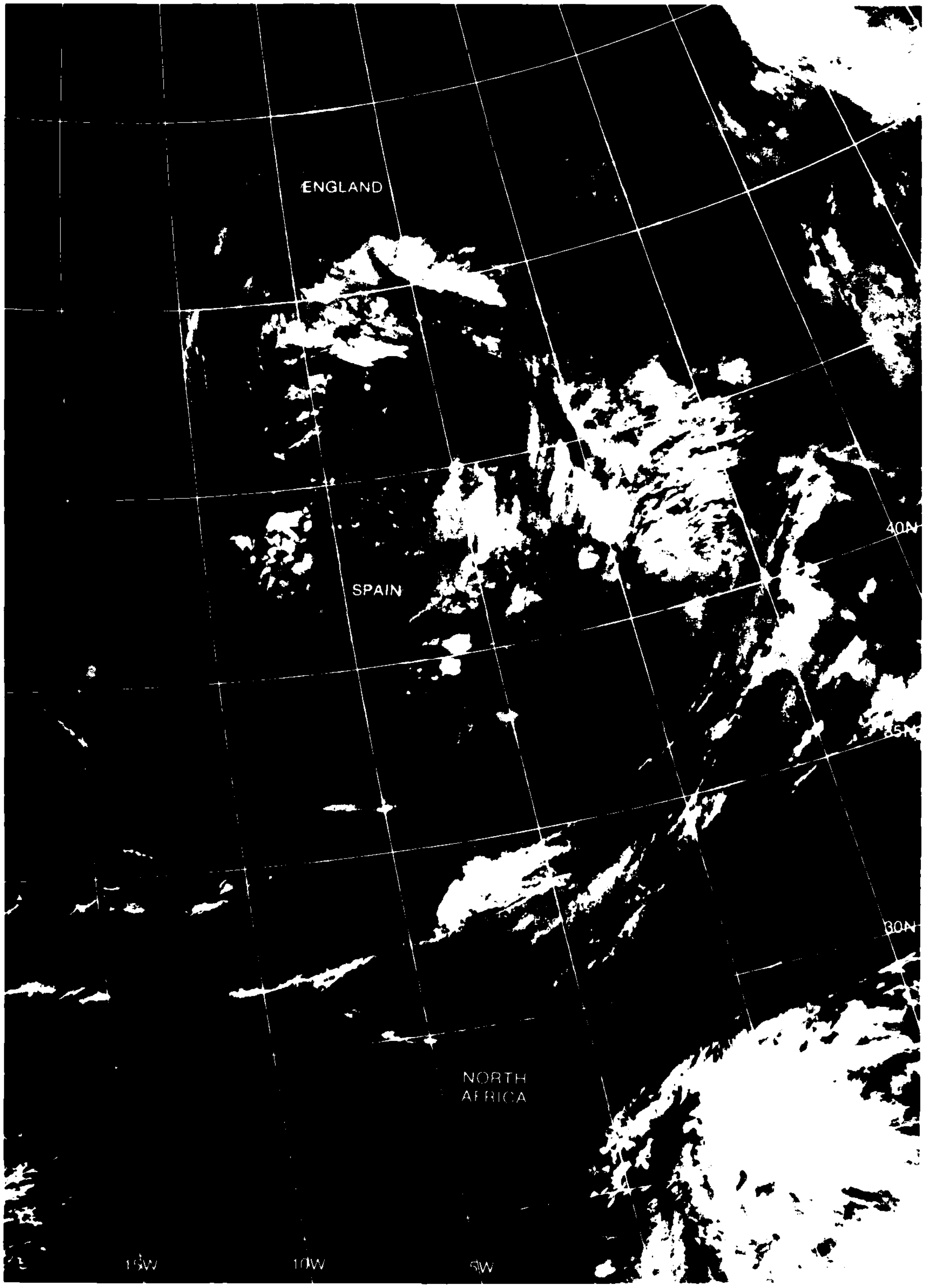

3B-25a. F-1. DMSP TF Normal Enhancement. 0010 GMT 16 May 1977.

16 May (continued)

3B-26a.
NMC Surface Analysis.
1200 GMT 16 May 1977.

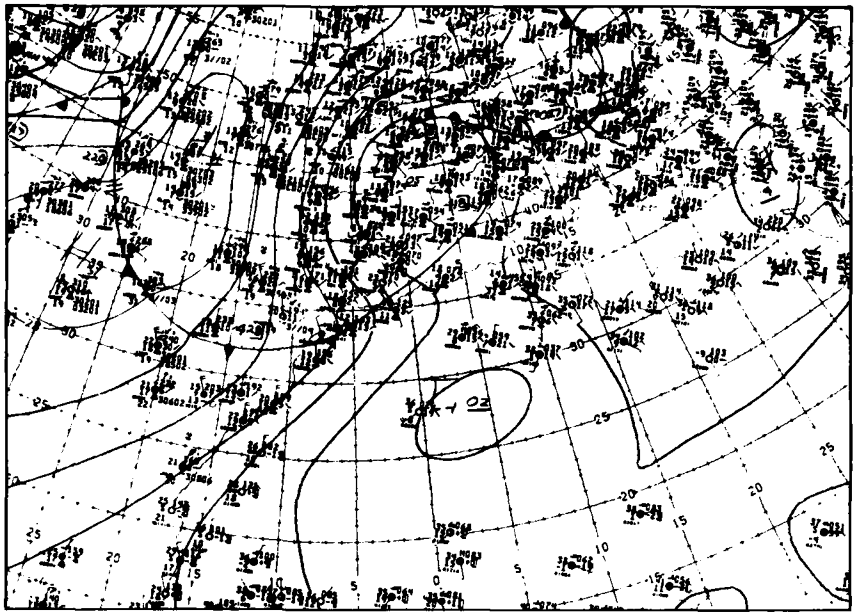

3B-26b.
NOAA-5 SR Visible Picture.
0932 GMT 16 May 1977.

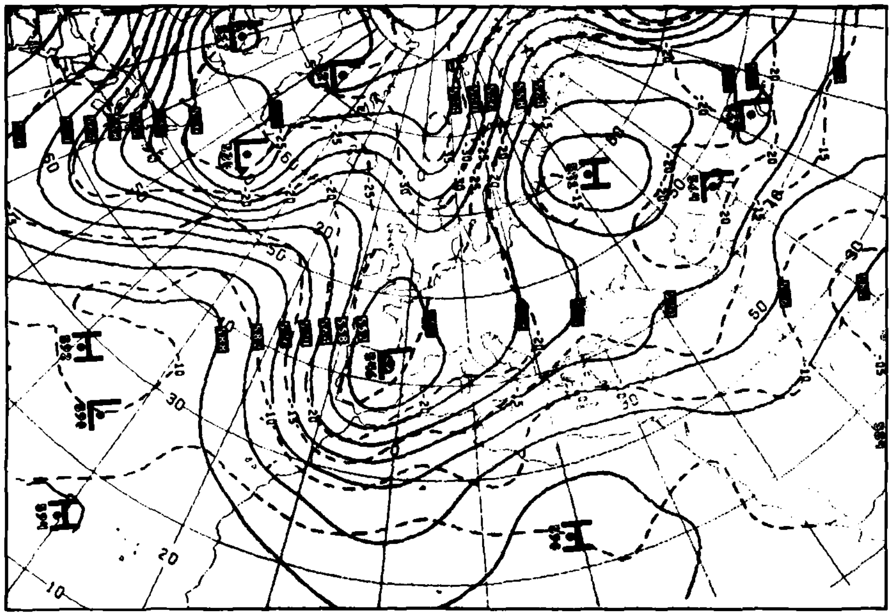

3B-27a. NMC 500-mb Analysis. 0000 GMT 17 May 1977.

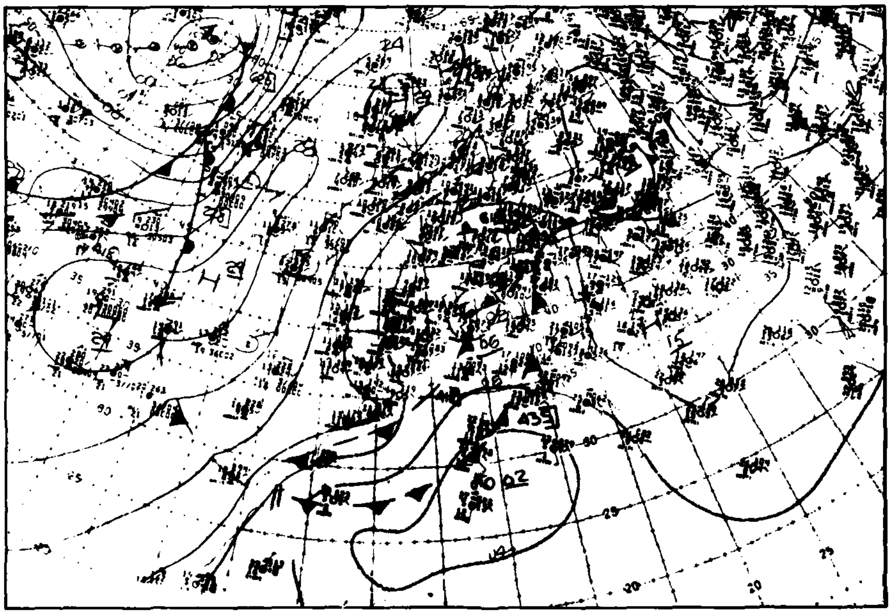

3B-27b. NMC Surface Analysis. 0000 GMT 17 May 1977.

17 May (continued)

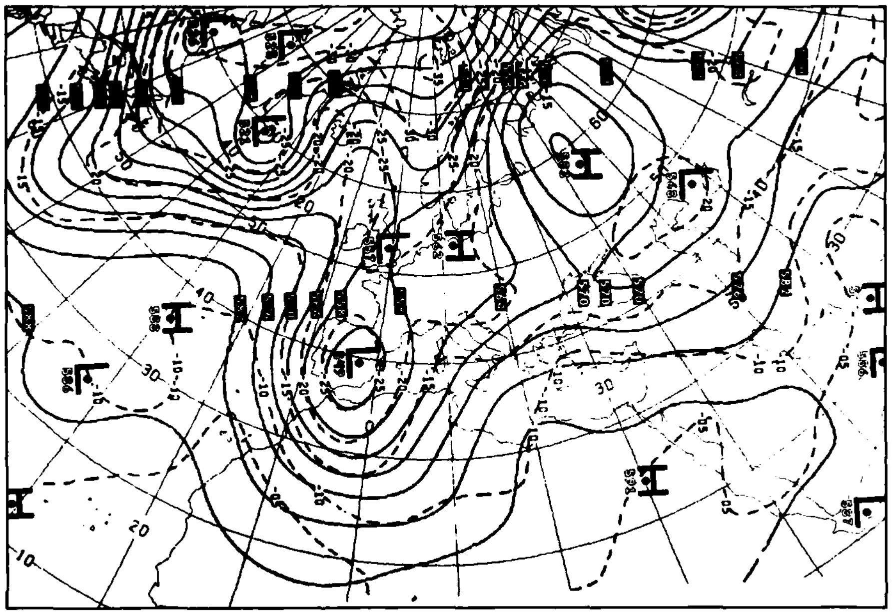

3B-28a. NMC 500-mb Analysis. 1200 GMT 17 May 1977.

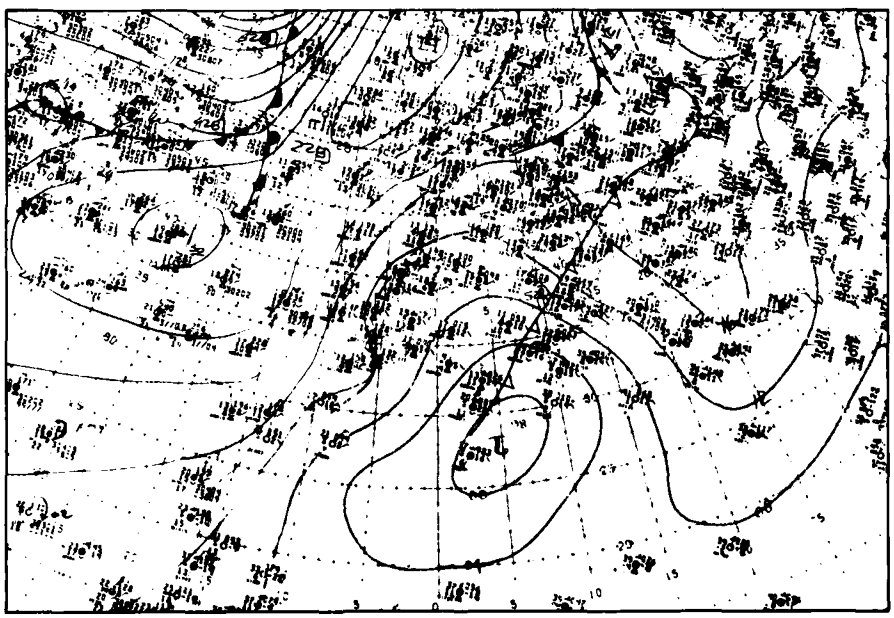

3B-28b. NMC Surface Analysis. 1200 GMT 17 May 1977.

3B-29a. F-1. DMSP LF Low Enhancement. 1105 GMT 17 May 1977.

Case 5 Cyclogenesis

Cyclogenesis over the Western Mediterranean

It has been established that the vast majority of cyclogeneses at sea level take place when an area of positive vorticity advection, ahead of a progressive trough at upper levels, becomes superimposed upon a quasi-stationary or slowly moving cold front (Petterssen, 1956). This event is one of the most reliable indications of cyclone development at the surface and is normally accompanied by a steepening and intensification of the frontal zone.

The forecast problem is knowing where the area of maximum positive vorticity advection is located and, consequently, when and where the subsequent surface development will take place. In satellite imagery, areas of maximum positive vorticity advection over the oceans often appear as an area of enhanced cumulus activity in the unstable cold air behind the front. The movement of such areas can then be tracked in the pictures, permitting the forecaster to predict when and where surface cyclogenesis will take place.

Reference

Petterssen, S., 1956: *Weather Analysis and Forecasting*, Vol. 1. McGraw-Hill Book Co., New York, 428 pp.

PVA MAX/Frontal Zone Interaction
Western Mediterranean
March 1978

29 March

Figure 3B-33a is a DMSP infrared picture which shows a weak cold front over the eastern Atlantic, northwestern Spain, and England. The frontal cloud band consists of mainly low- and middle-level cloudiness indicating weak upward vertical motion. In the area of cold air advection behind the front, near ocean weather station Romeo, an area of enhanced cumulus activity is apparent within a large field of open cell cumulus. This is an area of maximum positive vorticity advection (PVA MAX) associated with the leading edge of a short-wave trough at upper levels. Individual cumulonimbus cells can be clearly identified by their bright, globular appearance. Ships in the area are reporting showers, some heavy with hail. The proximity of the PVA MAX to the frontal zone suggests that it may overtake the front, producing conditions favorable for cyclogenesis over France during the next 24 hours.

In the initial FNOC PE 500-mb analysis (3B-32a), the short-wave trough is clearly visible near the axis of a deep, long-wave trough. This feature is reflected as a trough along 20°W in the initial surface analysis (3B-32c). The 24-hour, 500-mb prognosis (3B-32b), however, has smoothed out the short-wave trough and retained only the long-wave trough. As a result, the surface prognosis (3B-32d) shows only a weak trough, and not a closed low, extending south through western France into Spain.

30 March

An infrared picture taken near 0000 GMT (3B-35a) shows that the PVA MAX has caught up with the frontal system, initiating cyclogenesis. The frontal zone has also intensified as evidenced by the increased convective activity. A closed low with a central pressure of 1008 mb is shown on the surface analysis (3B-34c). At 500 mb (3B-34b) the short wave is located at 7°W and has also intensified.

Thus, in only 24 hours, a weak cold front has become a significant weather producer in the western basin of the Mediterranean. The combination of the active frontal zone and the trough at upper levels ensures that deteriorating weather conditions can be reliably predicted for the central Mediterranean.

31 March

On the following day, a DMSP visible picture (3B-37a) shows that the front has remained active as it has moved slowly across the Mediterranean. At this time the frontal cloudiness extends from northern Italy southward into North Africa. The surface low (3B-36b) is located in the Gulf of Genoa. The closed surface circulation is reflected by the spiral cloud pattern over northern Italy. At upper levels (3B-36a), the trough has moved southeast to the Gulf of Genoa and is becoming separated from the main westerly current to the north.

Important Conclusions

1. In the unstable air behind a cold front over the oceans, a PVA MAX often appears as an area of enhanced cumulus. The PVA MAX identifies the location of an upper-level, short-wave trough.

2. A weak cold front, in advance of such a short-wave trough, can re-intensify as a result of vorticity advection and become a major weather-producing system.

3. When satellite data show a PVA MAX (area of enhanced cumulus), which also appears as a short-wave trough in the initial 500-mb analysis, numerical forecasts of trough deepening downstream can be considered reliable.

March

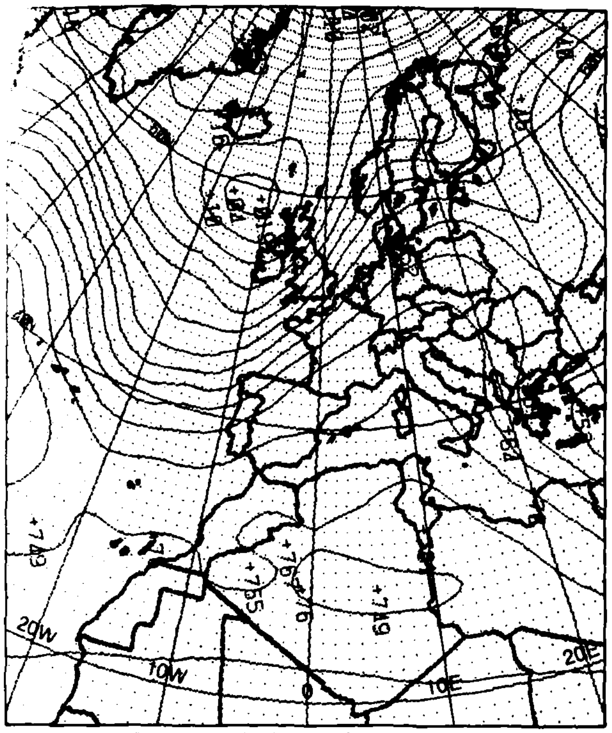

3B-32a. FNOC PE Initial 500-mb Analysis.
0000 GMT 29 March 1978.

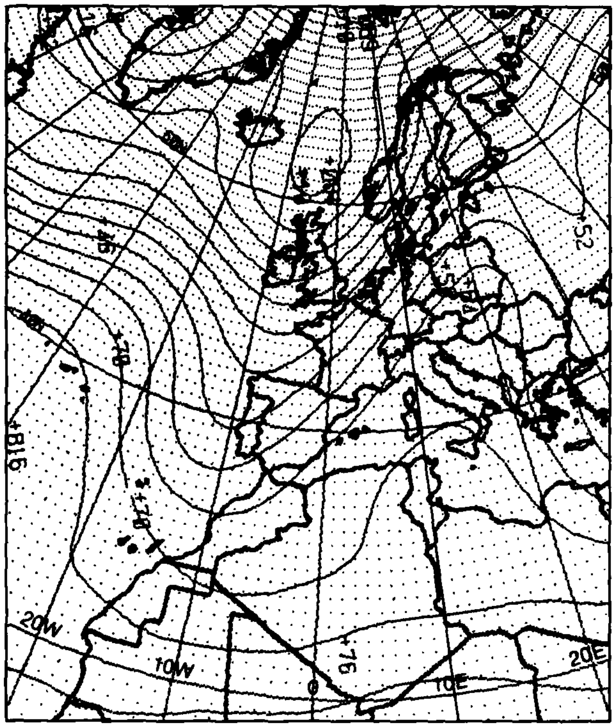

3B-32b. FNOC PE 24-Hour *500-mb Prognosis*.
Valid 0000 GMT 30 March 1978.

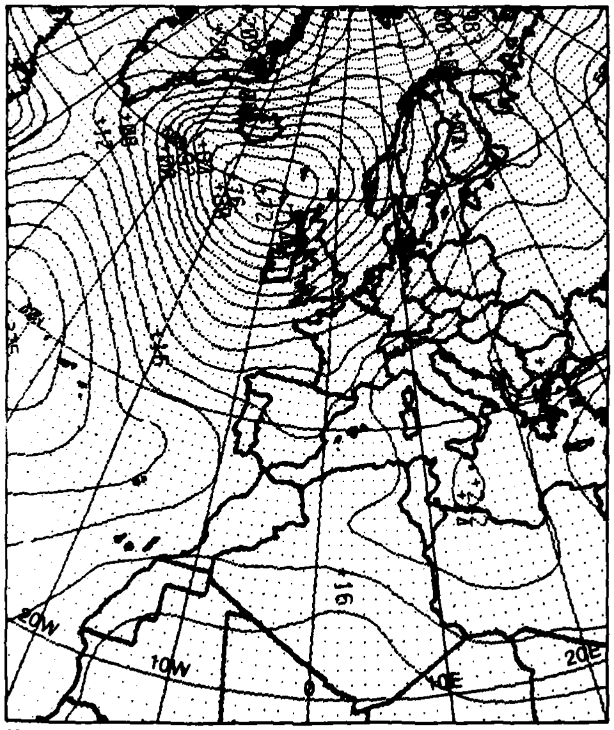

3B-32c. FNOC PE Initial Surface Analysis.
0000 GMT 29 March 1978.

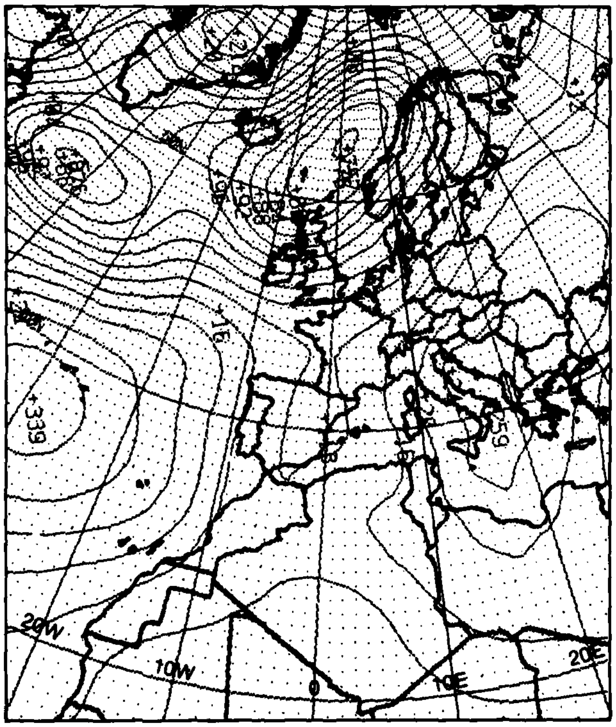

3B-32d. FNOC PE 24-Hour Surface Prognosis.
Valid 0000 GMT 30 March 1978.

29 March (continued)

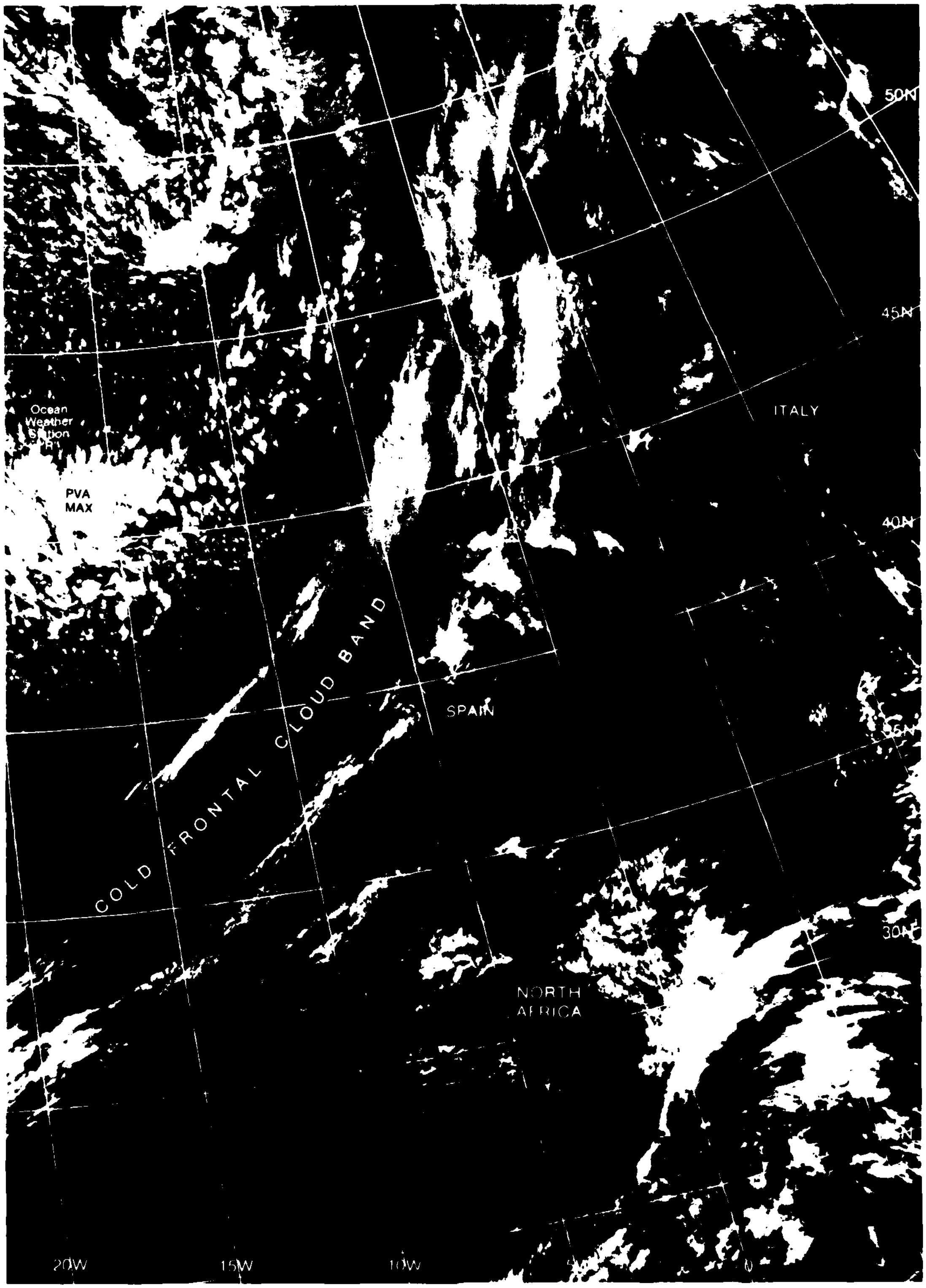

3B-33a. F-1. DMSP TF Normal Enhancement. 0021 GMT 29 March 1978.

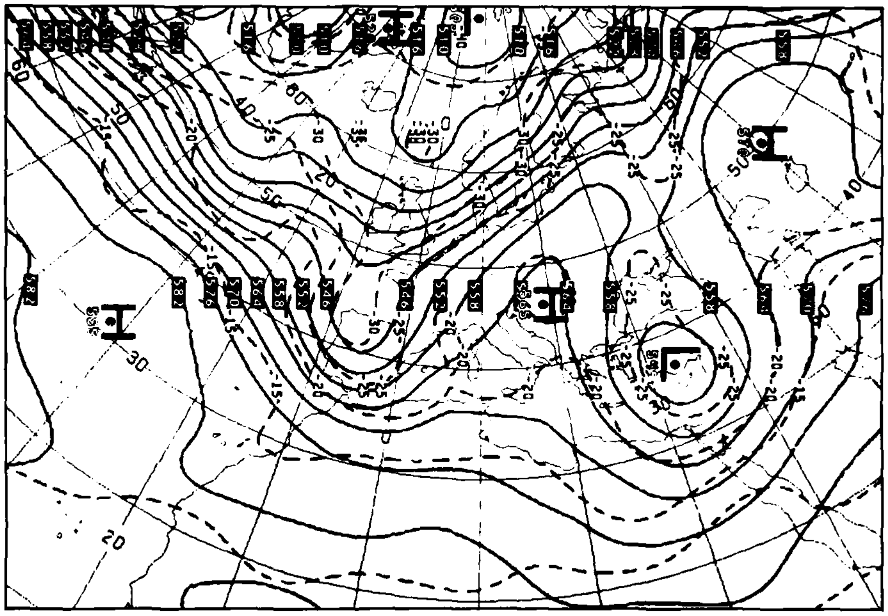

3B-34a. NMC 500-mb Analysis. 0000 GMT 30 March 1978.

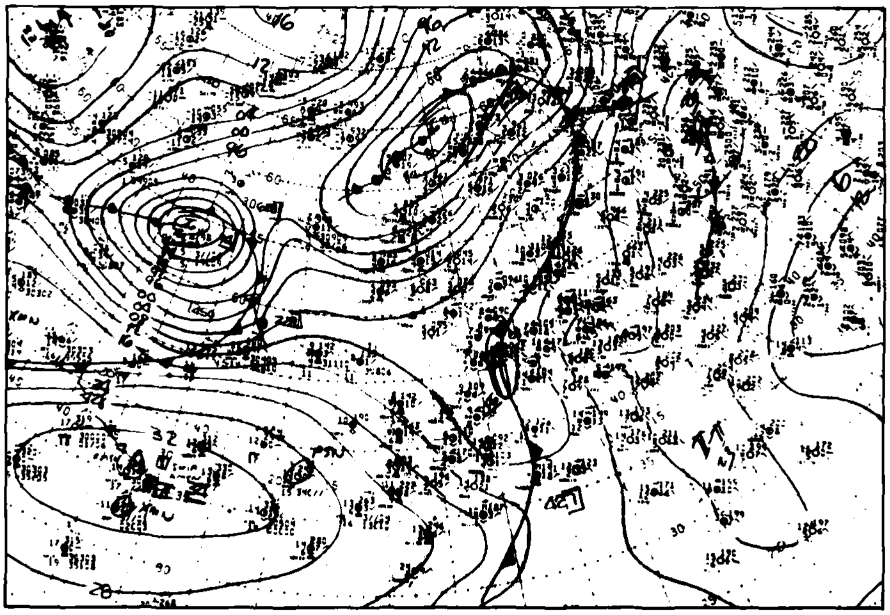

3B-34b. NMC Surface Analysis. 0000 GMT 30 March 1978.

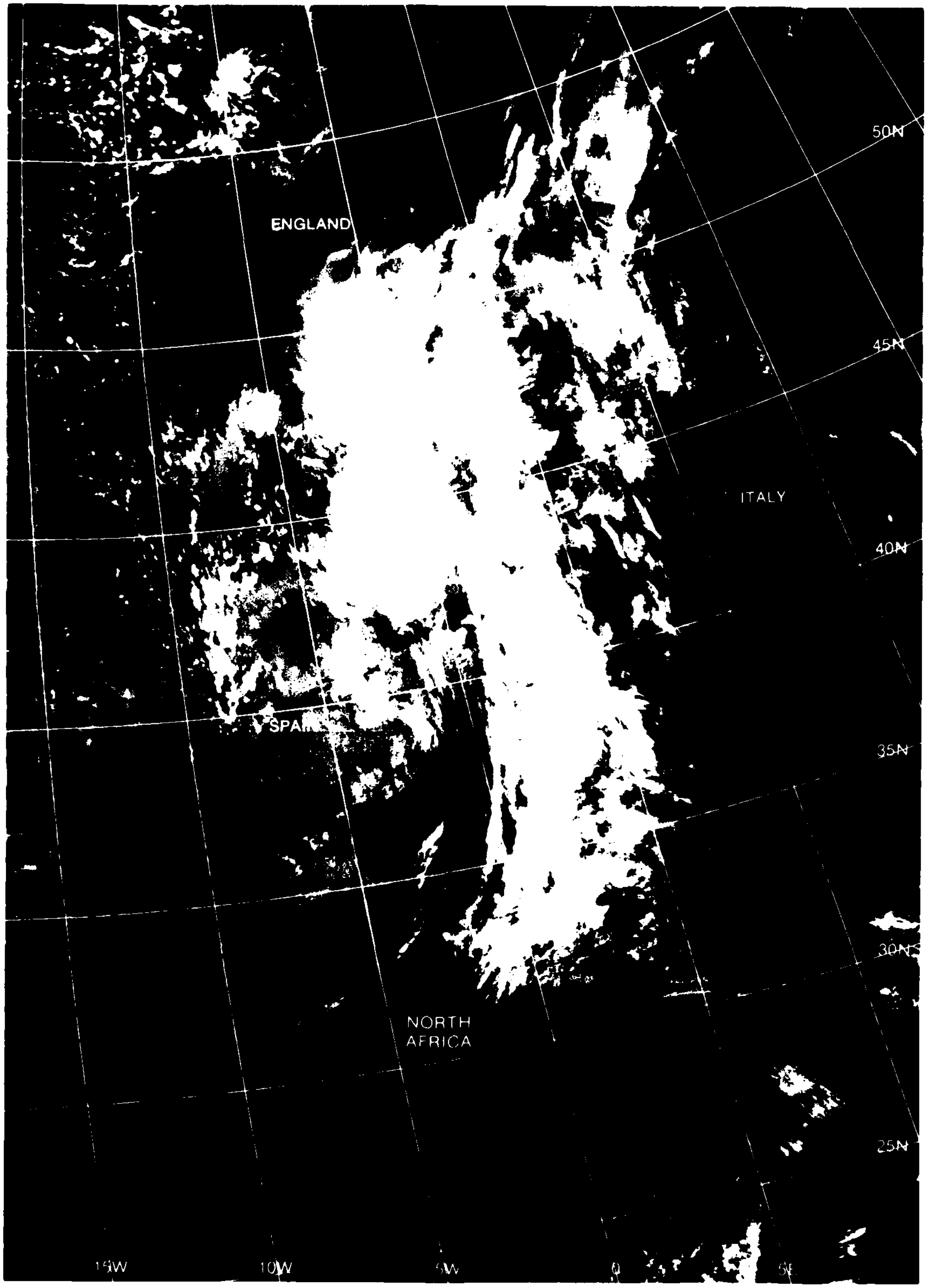

3B-35a. F-1. DMSP TF Normal Enhancement. 0003 GMT 30 March 1978.

31 March

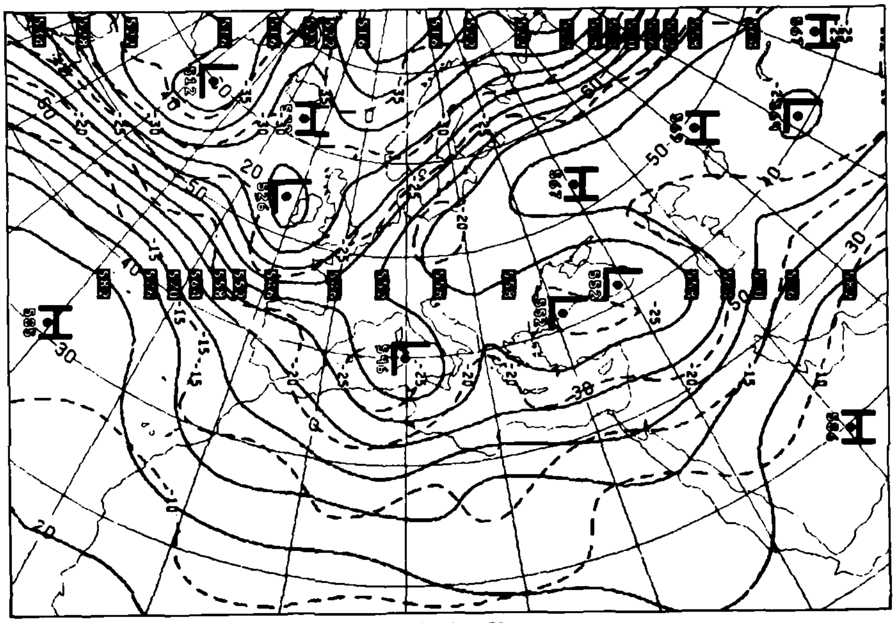

3B-36a. NMC 500-mb Analysis. 1200 GMT 31 March 1978.

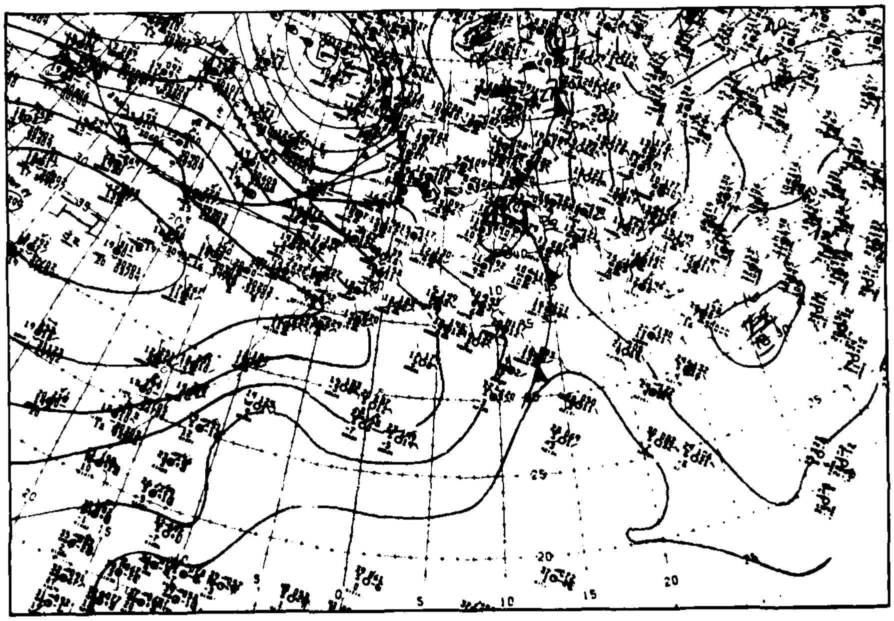

3B-36b. NMC Surface Analysis. 1200 GMT 31 March 1978.

3B-37a. F-1. DMSP LF Low Enhancement. 1046 GMT 31 March 1978.

Case 6 Cyclogenesis

Cyclogenesis in the Gulf of Genoa

One favored pattern for cyclogenesis in the Gulf of Genoa is the movement of a surface cold front into the gulf in advance of a short-wave trough at upper levels. The upper-level trough produces south-westerly flow aloft and positive vorticity advection over the position of the cold front in the gulf.

In this development pattern, higher surface pressure exists to the west over Spain and North Africa, and to the east over the Balkans. As a result, the cyclogenetic area in the Gulf of Genoa tends to remain stationary, positioned between the two higher pressure areas.

When the upper-level trough progresses, so that northerly winds aloft are in phase with the northerly surface flow over southern France, strong mistral winds occur. This sequence of events follows the forecast rule (Brody, 1980) that the strongest winds associated with a mistral do not occur until after the passage of the upper-level trough, which is well after the surface cold front has passed.

Reference

Brody, R., 1980: Handbook for Forecasters in the Mediterranean, Part 2. Forthcoming ENVPREDRSCHFAC Technical Paper.

Frontal-wave Cyclogenesis in Advance of an Upper-level Trough
Mediterranean—Gulf of Genoa
November-December 1975

29 November

The NMC surface analysis for 1800 GMT (3B-40b) shows a frontal system that extends through southern Europe from a large low pressure area with centers over the Norwegian Sea and over the Baltic Sea. A wave development occurs along the front over southern France. Northerly winds behind the front are advecting cold air from the Arctic Ocean down a long fetch, suggesting that the cold front has an ample supply of cold air and will continue to penetrate further south and east.

A DMSP infrared picture at 1955 GMT (3B-41a) shows the cloudiness which occurs along the cold front over southern Europe. The gray, middle-level cloudiness over the Atlantic and southern Spain indicates that that portion of the front is inactive. In contrast, the bright cloudiness over France is evidence of greater lifting and an area of active convection. To the west, many individual cumulonimbus cells are apparent in the large field of open cellular cloudiness from England to Spain. Further north, spiral cloud bands associated with the low pressure centers over the Norwegian Sea and the Baltic Sea are evident.

30 November

A pronounced cold trough is found at the 500-mb level along 7° W on the analysis at 0000 GMT (3B-40a). The cumulonimbus activity south of England, in the DMSP picture, is related to instability created by the cold temperatures in this trough aloft.

By 0600 GMT (3B-42a) the front has moved into the western Mediterranean, with a sharp trough over the Gulf of Genoa. A DMSP VHR picture at 0835 GMT (3B-43a) shows that the frontal cloudiness has penetrated south to the coast of North Africa, through the western Mediterranean, and into Italy. The large field of open cellular cloudiness over the North Atlantic indicates strong cold air advection. Cyclogenesis proceeded rapidly and a closed low is analyzed in the Gulf of Genoa on the 1200 GMT surface chart (3B-42b).

The progression of the cold front to a position from Italy to Tunisia is shown in the surface analysis 6 hours later (3B-42c). It can be seen from this and the previous analyses that the cold front has moved rapidly eastward over the western Mediterranean, while the Genoa low has moved only slowly over the Po River Valley in northern Italy. By 1800 GMT, high pressure has moved in behind the front over Spain and France and is also present over the Balkans.

In a DMSP infrared picture taken later in the day (3B-44a), cumulonimbus activity can be seen in the southern portion of the Bay of Biscay and along the Pyrenees Mountains. Thunderstorms have also broken out behind the frontal cloud band from the Gulf of Lion past the Balearic Islands. This thunderstorm outbreak is indicative of the arrival of cold, unstable air aloft in the polar trough. The changing orientation of wave clouds over Spain, North Africa, and Italy suggests the position of the upper-level trough as shown by the arrows. Although northerly winds are flowing through the Rhone River Valley, at this time, at low levels, no mistral conditions are encountered because the northerly flow of the upper-level trough had not yet become superimposed on the low-level northerly winds.

1 December

The upper-level flow pattern suggested by the wave clouds is verified by the 500-mb analysis at 0000 GMT (3B-45a). Note that strong ridging now occurs east of the trough.

The movement of the upper-level trough, from near longitude 7° W on 30 November at 0000 GMT to near 5°E in 24 hours, suggests that northerly upper-level winds will soon be superimposed upon the low-level northerlies in southern France. When this happens, mistral conditions will occur in the Gulf of Lion. The Genoa depression should be expected to reach maximum intensity in the hours prior to superposition and then fill slowly as the cold air in the upper-level trough causes the surface pressure to rise. The speed of the upper-level trough should then slow considerably due to the strong ridging to the east.

The onset of a mistral in the Gulf of Lion is shown in an early morning DMSP visible picture (3B-45b). Offshore, anomalous gray shades, and then cloud lines, form as the cold air sweeps out over the warmer water. The anomalous gray shades develop in the marine layer as moisture accrues to condensation particles, which continue to grow to cloud droplet sizes. Poor low-level visibilities exist in these areas. The orientation of wave clouds over southern France indicates that northerly upper-level winds are now superimposed on the northerly surface flow. Marsailles reported persistent 30 kt winds from the north during the day. Winds were much stronger at sea.

By 1200 GMT, the upper-level trough overtook the surface low, which then became stationary. It subsequently filled the following two days, causing mistral conditions to gradually abate.

Important Conclusions

1. A typical sequence for the development of a mistral is the movement of a cold front into the western Mediterranean, followed by cyclogenesis in the Gulf of Genoa and, later, the passage of a cold, upper-level trough following the front.

2. Mistral-force winds occur when the northerly winds of the upper-level trough become superimposed upon the northerly flow through the Rhone River Valley, at the head of the Gulf of Lion.

3. The orientation of wave clouds can be used to infer upper-level flow features and, in particular, the location of the cold, upper-level trough preceeding the mistral.

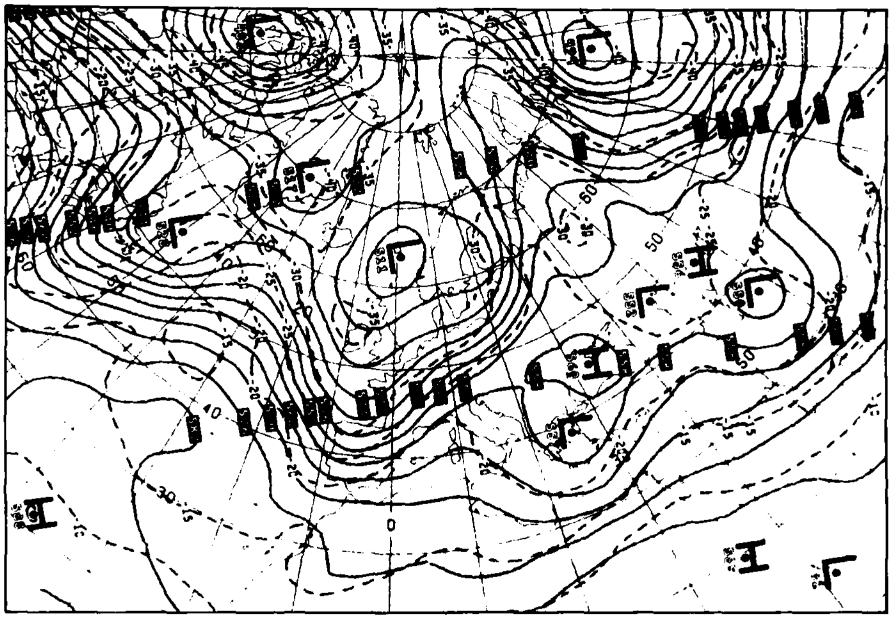

3B-40a. NMC 500-mb Analysis. 0000 GMT 30 November 1975.

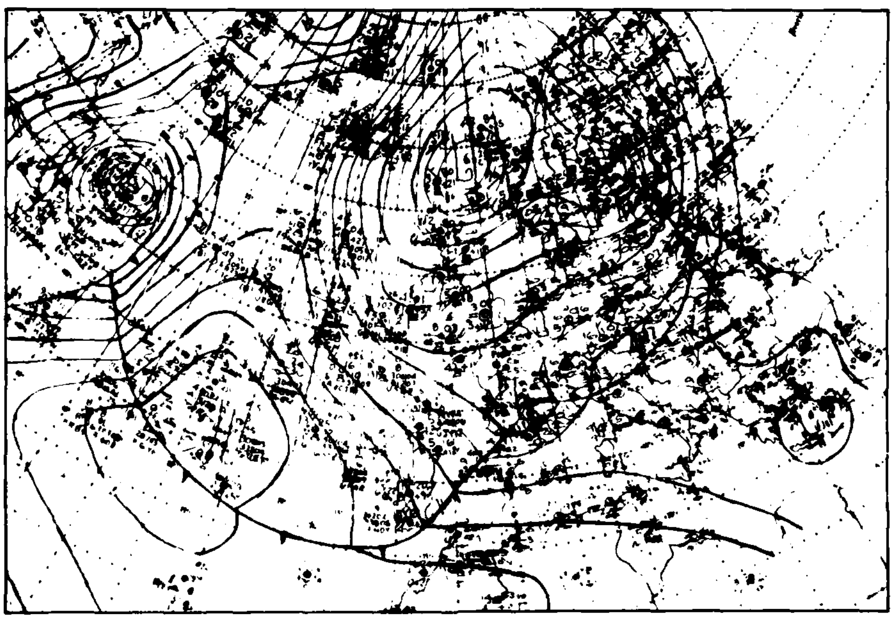

3B-40b. NMC Surface Analysis. 1800 GMT 29 November 1975.

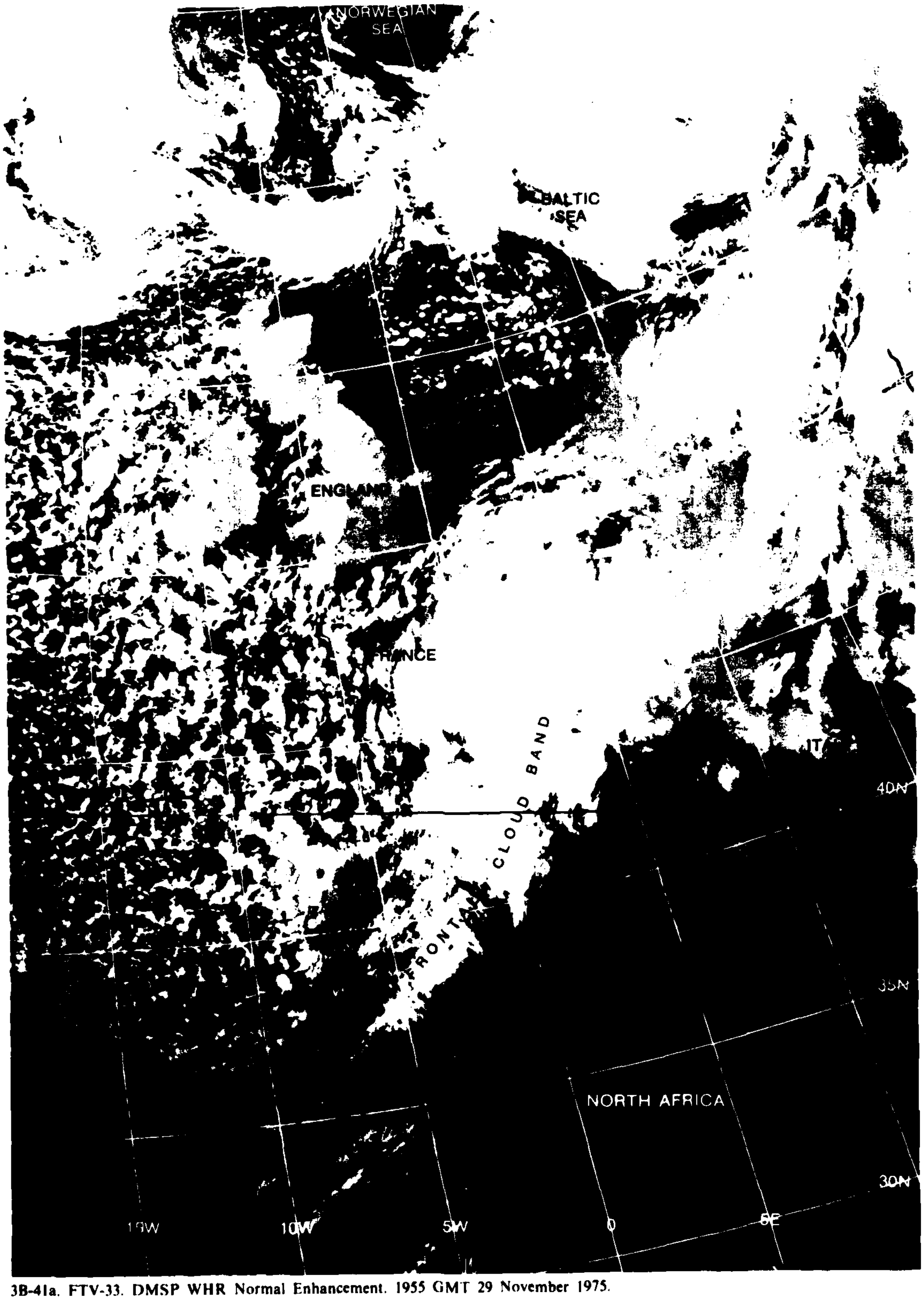

3B-41a. FTV-33. DMSP WHR Normal Enhancement. 1955 GMT 29 November 1975.

30 November (continued)

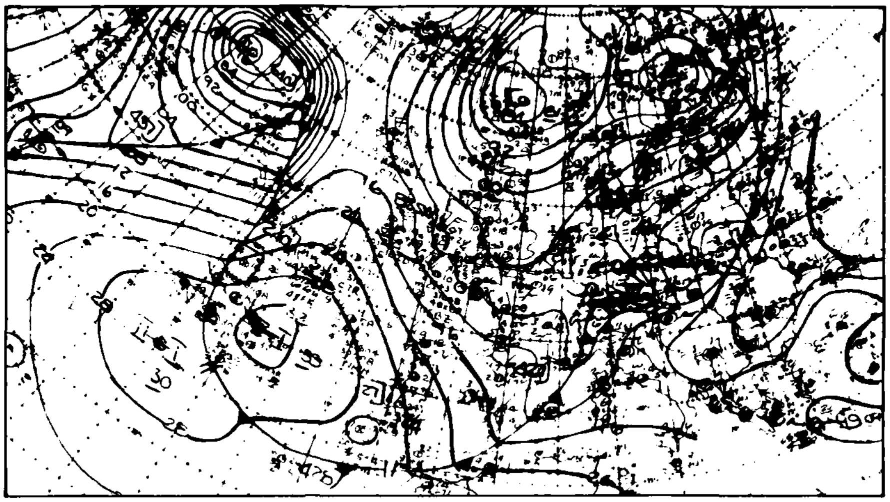

3B-42a.
NMC Surface Analysis.
0600 GMT
30 November 1975.

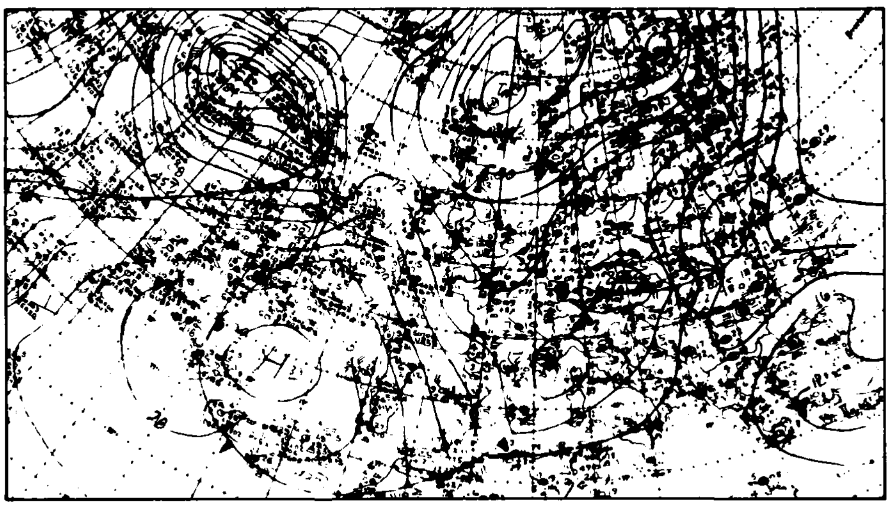

3B-42b.
NMC Surface Analysis.
1200 GMT
30 November 1975.

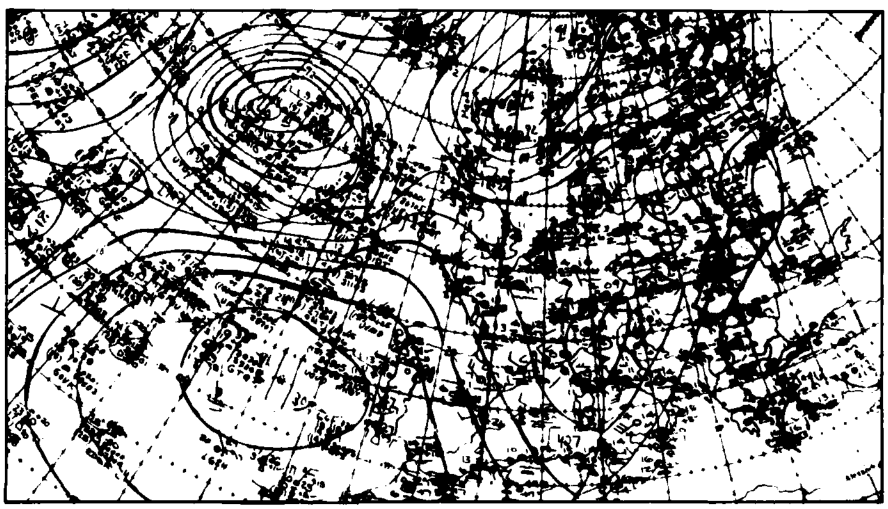

3B-42c.
NMC Surface Analysis.
1800 GMT
30 November 1975.

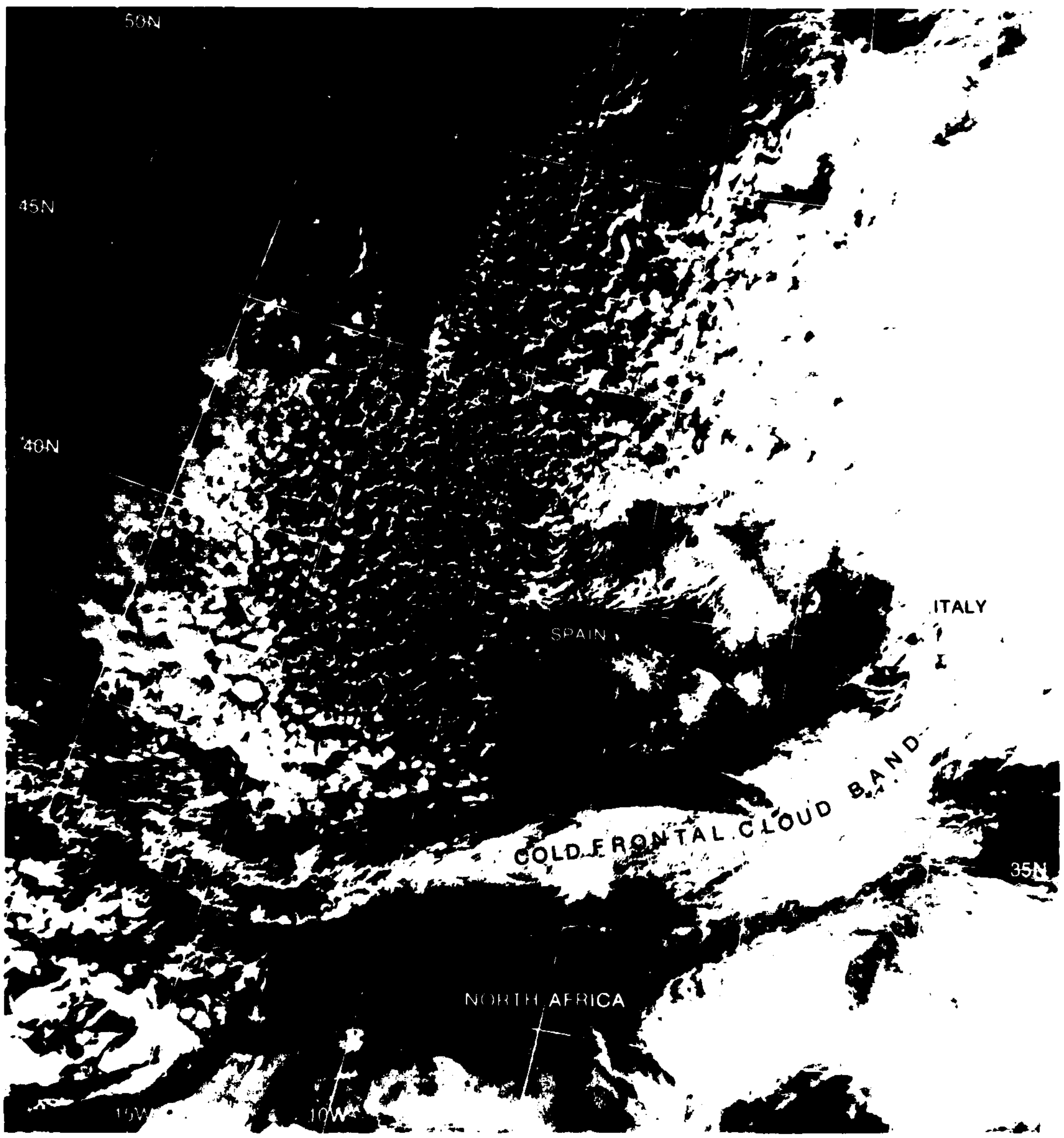

3B-43a. FTV-29. DMSP VHR Low Enhancement. 0835 GMT 30 November 1975.

30 November (continued)

3B-44a. FTV-33. DMSP WHR Normal Enhancement. 1943 GMT 30 November 1975.

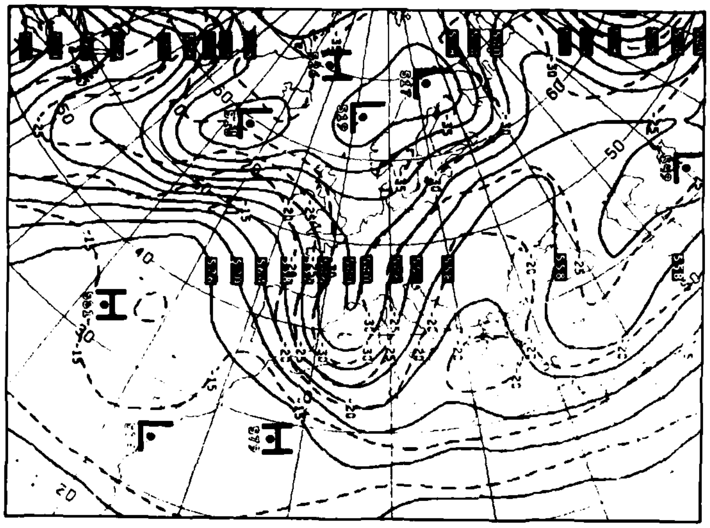

3B-45a.
NMC 500-mb Analysis.
0000 GMT
1 December 1975.

3B-45b. Enlarged View. FTV-29. DMSP VHR Low Enhancement. 0816 GMT 1 December 1975.

Case 7 Cyclogenesis

Cyclogenesis in the Gulf of Genoa

A second pattern favorable for cyclogenesis in the Gulf of Genoa is the establishment of a 500-mb, long-wave ridge over the eastern Atlantic, with general northwesterly flow into the western Mediterranean. The surface synoptic situation accompanying this development pattern is a low over the North Sea, a cold front extending to the Iberian Peninsula, and an extension of the Azores high over North Africa. As the cold front progresses southeastward, it is reflected in the upper air as a short-wave trough moving through the long-wave ridge. Upon reaching the Alps, the front becomes deformed and the pressure begins to fall in northern Italy. The persistence of this long-wave pattern gives rise to repeated cyclogenesis in the Gulf of Genoa, as periodic short waves move through (Brown, 1964).

Reference

Brown, W.F., 1964: Local area forecasters handbook. Naval Weather Service Environmental Detachment, Sigonella, Sicily, 48 pp.

Frontal-wave Cyclogenesis—Short Wave within a Persistent Long-wave Ridge/Trough
Mediterranean—Gulf of Genoa
March 1978

On 16 March 1978, a long-wave ridge became established over the eastern North Atlantic producing northwesterly flow aloft into the western Mediterranean. By 18 March, the first depression had developed over the Gulf of Genoa and subsequently moved off over the Adriatic Sea. A total of three more depressions formed over the Gulf of Genoa, until 28 March, each moving off to the east over the Adriatic Sea and eastern Mediterranean. After 28 March, a long-wave trough replaced the ridge in the eastern North Atlantic and the sequence terminated.

21 March

Two DMSP visible images taken on consecutive passes (1019 and 1201 GMT) are shown in 3B-49a and 3B-48a. At this time, the second in the series of four cyclones has formed and moved into the northern Adriatic Sea. The relationship between the cloud patterns in these pictures and the synoptic situation can be used to infer the upper-level flow patterns over the eastern North Atlantic and Europe. In 3B-48a, billow clouds along the cold frontal cloud band indicate turbulence and a strong southwesterly flow. Ahead of the front, anticyclonically turning, upper-level flow is indicated by cirrus streamers and the presence of closed cellular stratocumulus. Further east, in 3B-49a, the orientation of wave clouds (arrows) over Spain, Majorca, Tunisia, Sicily, and Italy indicate a northwesterly flow over Spain that gradually turns cyclonically, becoming westerly over Italy. These clouds can be used to locate the position of the upper-level ridge over the eastern Atlantic and the upper-level trough over southern Europe. In addition, cloud lines over southern England and northern France are evidence of strong, low-level, northerly winds which, in conjunction with the northwesterly flow aloft, are giving rise to mistral conditions in the Gulf of Lion (see NTAG Vol. 2, Sec. 2D, Case 4). These flow patterns are verified by the NMC surface and 500-mb analysis for 1200 GMT (3B-49c and 49b).

The long-wave ridge/trough pattern deduced from the satellite imagery is forecast to persist for 72 hours, as shown in the FNOC PE 500-mb prognosis (3B-50a). This suggests that the short-wave trough to the west, extending from the low centered near 60° N, 40° W, will be steered by the long-wave pattern and lead to another probable cyclogenesis in the Gulf of Genoa, in the following 48 to 72 hours. This development, however, is not shown in the FNOC 72-hour surface prognosis (3B-50c) as a closed low center, but is reflected as a weak trough.

22-23 March

During this two day period, the upper-level, short-wave trough moved through the long-wave ridge position in the eastern North Atlantic and began to move south over western Europe (3B-50b and 51a). The cold front continued to move eastward (3B-50d), and by 1200 GMT 23 March (3B-51c) extended from the Iberian Peninsula to a low center over the North Sea. Note the deep trough of low pressure along the cold front through the Gulf of Genoa.

24 March

Surface pressures continued to fall rapidly in the Gulf of Genoa as the front moved through, and by 0600 GMT (not shown) a closed low was analyzed over the gulf. The rapid movement of the upper-level, short-wave trough, and thus the surface low, are shown in the NMC analyses at 1200 GMT (3B-51b and 51d).

The verifying FNOC PE 500-mb analysis (3B-52a) shows a deep trough over northern Italy with strong northwesterly flow into the western Mediterranean. The concurrent surface analysis (3B-52b) has a closed low over the Adriatic Sea with a deep trough over the Po River Valley.

In a DMSP visible picture near this time (3B-53a), wave clouds over Corsica, Sardinia, and Greece again can be used to locate the position of the upper-level trough in southern Europe. Cloudiness associated with the surface low is evident over Yugoslavia, the Adriatic Sea, and central Italy.

Important Conclusions

1. A persistent long-wave ridge over the eastern Atlantic, coupled with a long-wave trough over the central Mediterranean, is a pattern which tends to steer short-wave disturbances into the Gulf of Genoa and leads to repeated episodes of cyclogenesis in the gulf.

2. Cloud patterns observed in satellite imagery are helpful in delineating the features of such a long-wave pattern. In addition, by using satellite imagery to identify the position of the short waves within the long-wave pattern, reasonably accurate 48- to 72-hour forecasts can be made of cyclogenesis episodes in the Gulf of Genoa.

3B-48a. F-1. DMSP LF Low Enhancement. 1201 GMT 21 March 1978.

21 March (continued)

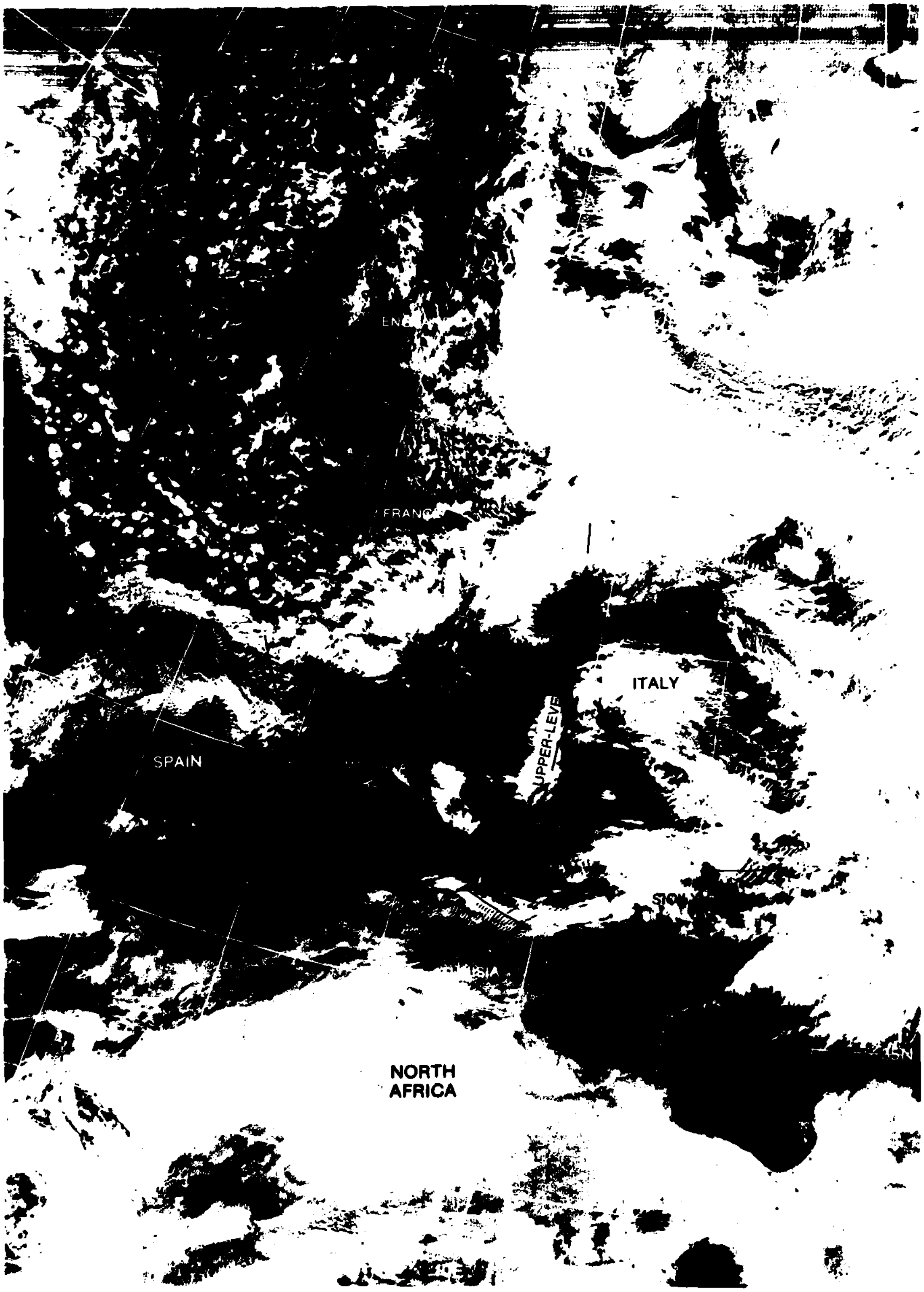

3B-49a. F-1 DMSP LF Low Enhancement. 1019 GMT 21 March 1978.

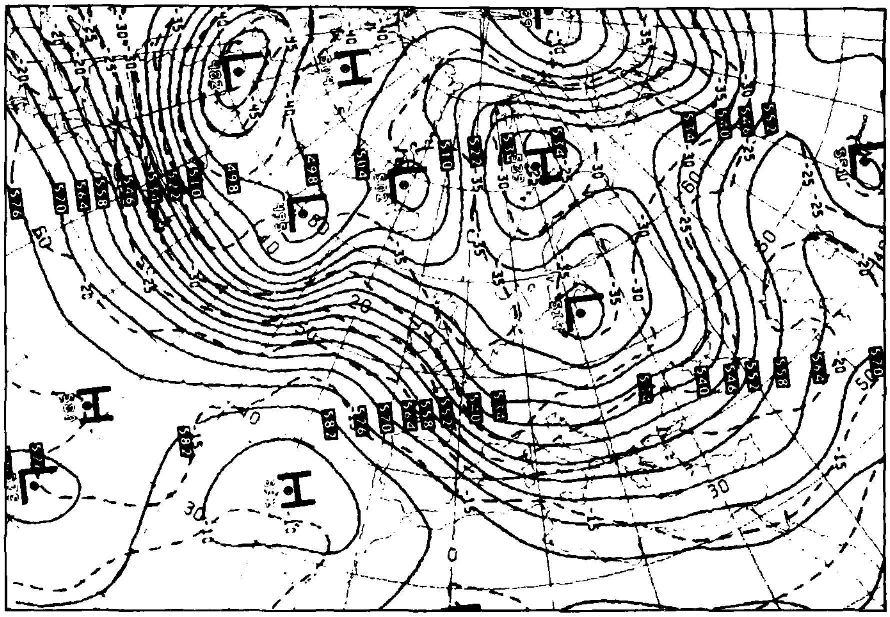

3B-49b. NMC 500-mb Analysis. 1200 GMT 21 March 1978.

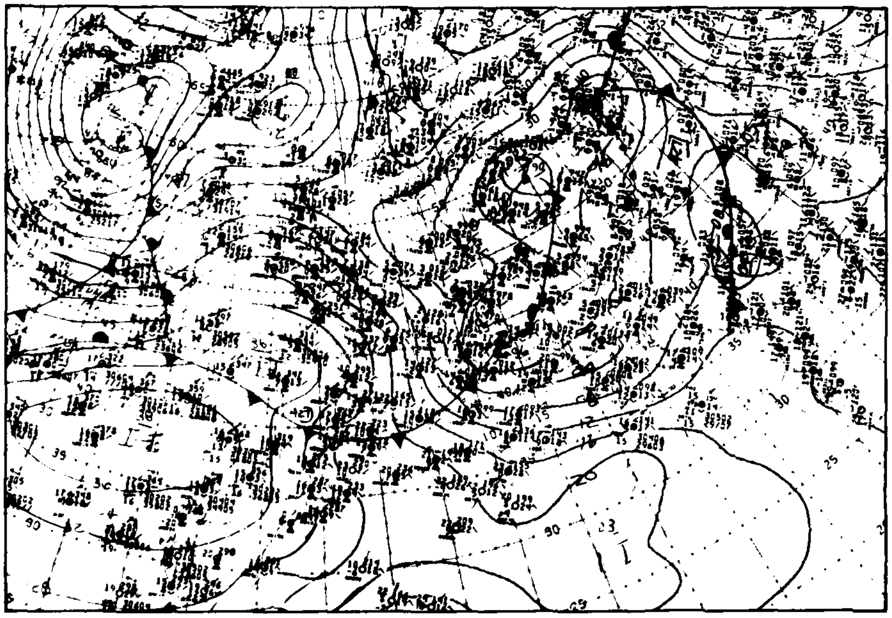

3B-49c. NMC Surface Analysis. 1200 GMT 21 March 1978.

21 March (continued)

22 March

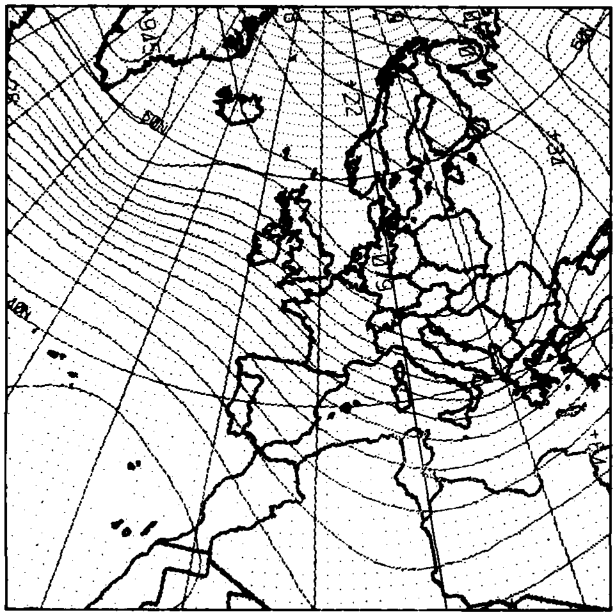

3B-50a. FNOC PE 72-Hour 500-mb Prognosis.
Valid 1200 GMT 24 March 1978.

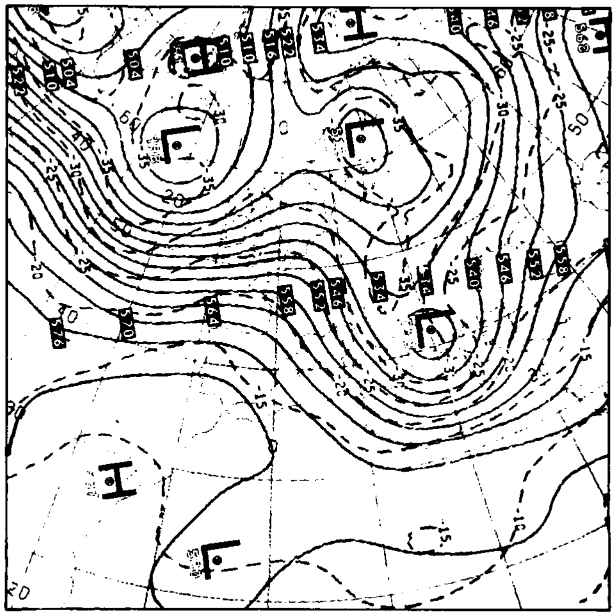

3B-50b. NMC 500-mb Analysis.
1200 GMT 22 March 1978.

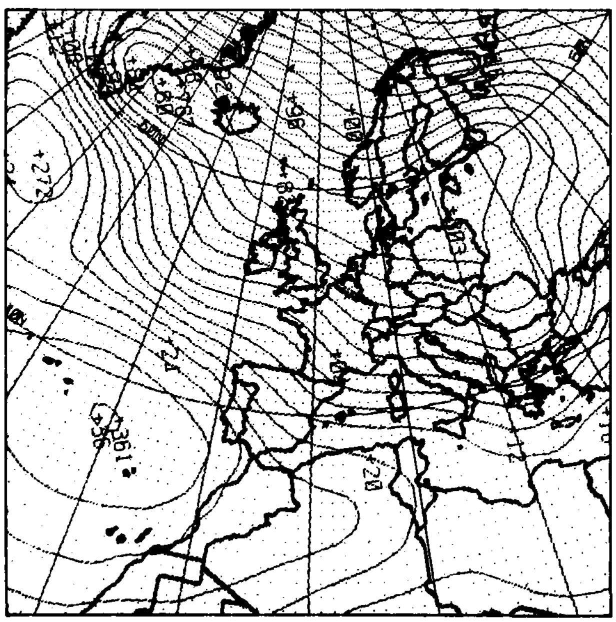

3B-50c. FNOC PE 72-Hour Surface Prognosis.
Valid 1200 GMT 24 March 1978.

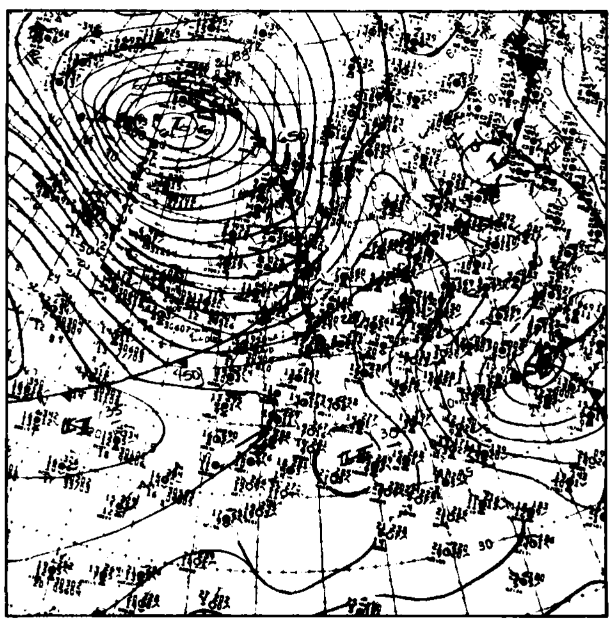

3B-50d. NMC Surface Analysis.
1200 GMT 22 March 1978.

23 March **24 March**

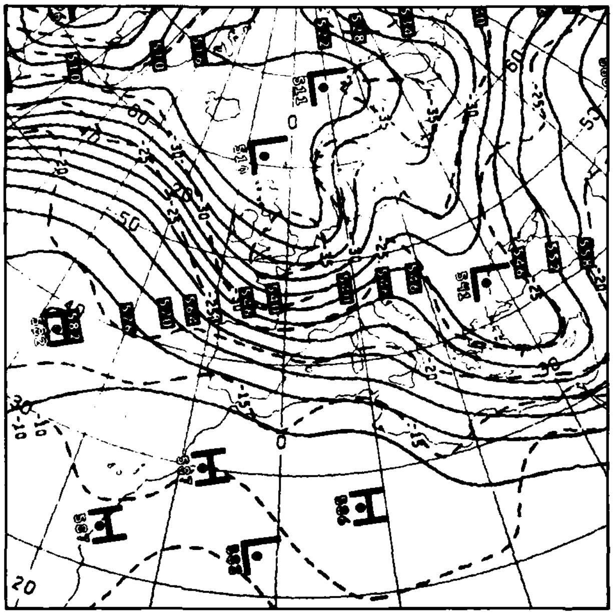

3B-51a. NMC 500-mb Analysis.
1200 GMT 23 March 1978.

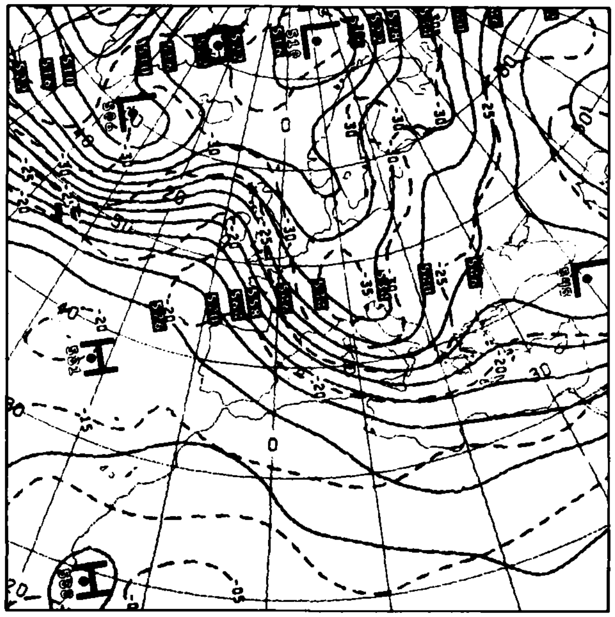

3B-51b. NMC 500-mb Analysis.
1200 GMT 24 March 1978.

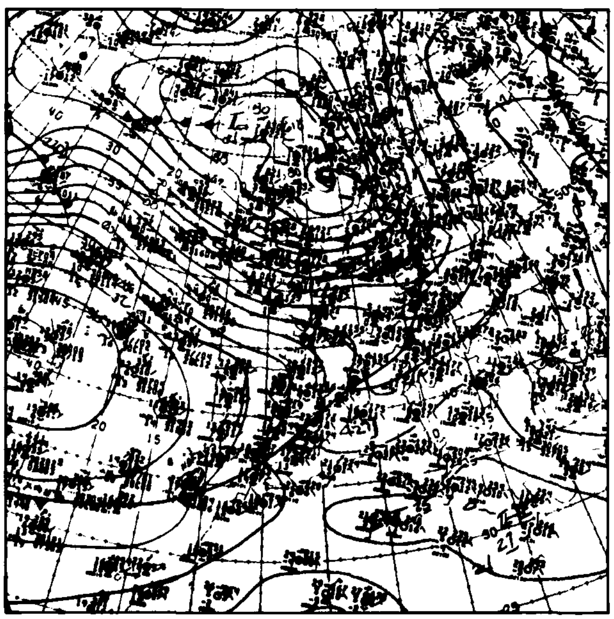

3B-51c. NMC Surface Analysis.
1200 GMT 23 March 1978.

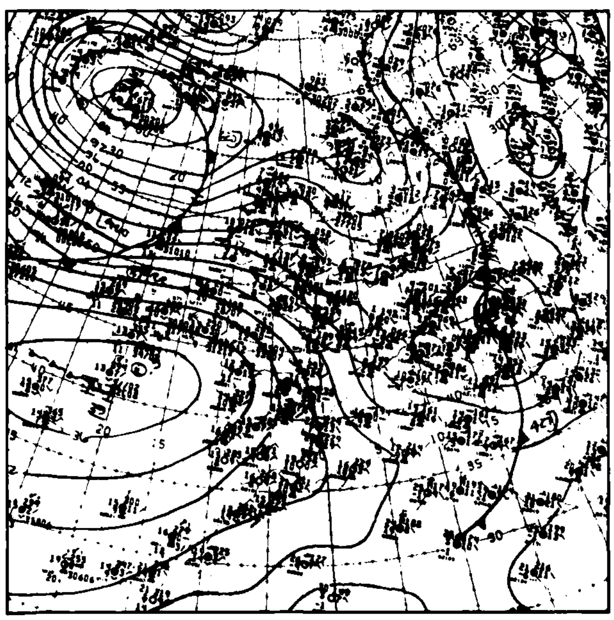

3B-51d. NMC Surface Analysis.
1200 GMT 24 March 1978.

24 March (continued)

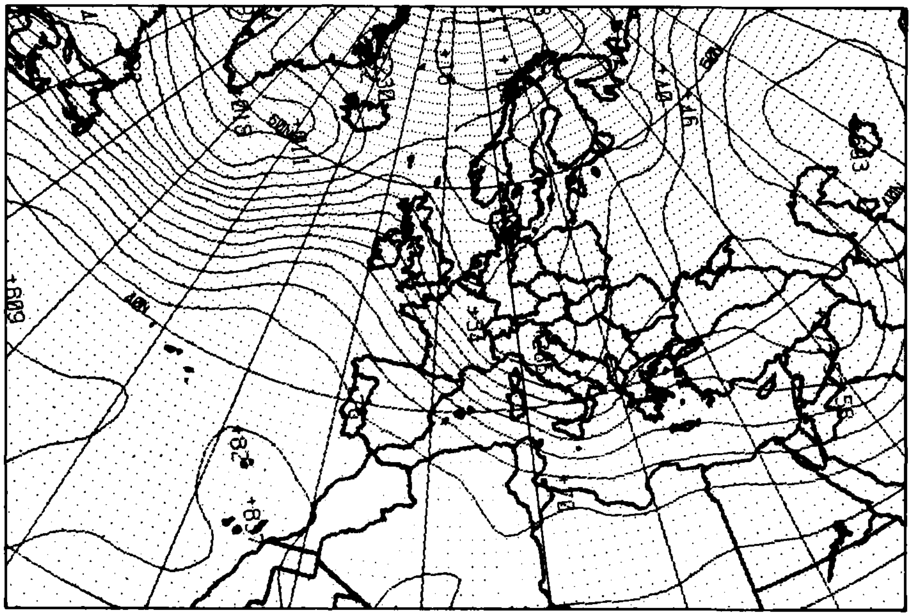

3B-52a. FNOC PE Verifying 500-mb Analysis. 1200 GMT 24 March 1978.

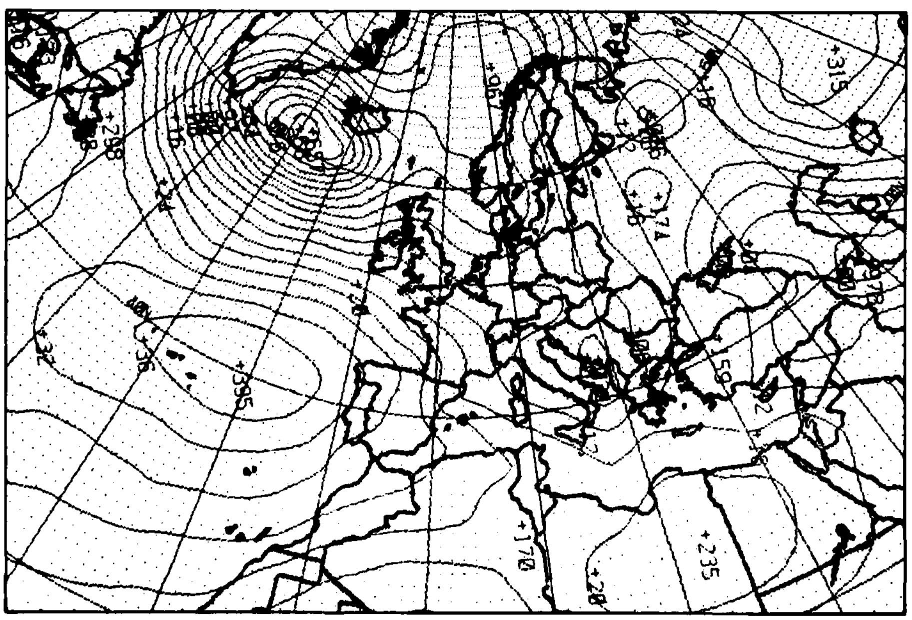

3B-52b. FNOC PE Verifying Surface Analysis. 1200 GMT 24 March 1978.

24 March (continued)

3B-53a. F-1. DMSP LS Low Enhancement. 0926 GMT 24 March 1978.

This section is under development and will be forwarded for inclusion in this volume.